UNIVERSITA' DEGLI STUDI DI PADOVA

Sede Amministrativa: Università degli Studi di Padova
Sede Consorziata: ISMN-CNR Bologna

Dipartimento di Scienze Chimiche

SCUOLA DI DOTTORATO DI RICERCA IN: Scienza ed ingegneria dei materiali
INDIRIZZO:
XX° Ciclo

Functional dielectric/semiconductor and metal/semiconductor interfaces in organic field-effect transistors

Direttore della Scuola: Ch.mo Prof. Gaetano Granozzi
Supervisore: Ch.mo Prof. Renato Bozio
Dott. Michele Muccini

Dottorando : Francesco Todescato

Frequent abbreviations and acronyms:

- Δ potential across the dipole layer present at the metal/OS interface
- ε dielectric constant of a medium
- θ_c contact angle
- μ field-effect mobility
- ρ resistivity
- ϕ work function of an organic material
- Φ_B^n energy barrier for the electrons injection
- Φ_B^p energy barrier for the holes injection
- Φ_{gs} solid wave function in its unperturbed state
- $\Phi^{r(j)}$ solid wave functions including the intramolecular perturbations
- 7-th tetrathia[7]helicene
- 7th-C3 7,8-dipropyl-tetratia-[7]-helicene
- A organic semiconductor electron affinity
- ALK-Ph(Z)-1,2-bis-(benzo-[1,2-b;4,3-b']-dithiophen-2yl)-styrene
- AFM Atomic Force Microscopy
- BCB divinyl-tetramethylsiloxane-bis(benzocyclobutene) derivative
- BG-BC bottom gate - bottom contact transistors
- BG-TC bottom gate - top contact transistors
- btp_2[Ir]acac bis(2-(2'-benzothienyl) pyridinato-N,C3')(acetylacetonate)
- C_i dielectric capacitance per unit area
- DHCO-4T α,ω-dihexylcarbonylquaterthiophene
- E_g energy gap
- ETL Electron Transport Layer
- FET Field-Effect Transistor
- GB Grain Boundaries
- HMDS hexamethyldisilazane
- HOMO Highest Occupied Molecular Orbital
- HTL Hole Transport Layer
- I organic semiconductor ionization energy
- I_{ds} current flowing through the channel
- ITO Indium Tin Oxide
- L transistor channel length
- LED Light Emitting Diode
- LUMO Lowest Unoccupied Molecular Orbital
- MB02 1,2-dibenzoditiofene-etene
- MEH-PPV Poly[2-methoxy-5-(2-ethylhexyloxy)-1,4-phenylenevinylene]
- n(x) number density of charges in the channel
- OC_1C_{10}-PPV Poly[2-methoxy-5-(3,7-dimethyloctyloxy)-1,4-phenylenevinylene]
- OFET Organic Field-Effect Transistor
- OLED Organic Light Emitting Diode
- OLET Organic Light Emitting Transistor
- OS Organic Semiconductors
- OTS octadecyltrichlorosilane
- PMMA poly-methylmetacrylate
- PV Photovoltaic Cell
- PVA polyvinilyalchol
- q_{ind} induced charge density
- RFID Radiofrequency Identification Cards
- RMS Root Mean Square
- RT Room Temperature
- SAM Self Assembled Monolayer
- t thickness of the charged layer in the transistor channel
- T3 ter(9,9-diarilfluorene)
- T_g glass transition temperature
- TG-BC top gate – bottom contact transistors
- TOF Time Of Flight
- V_{ds} voltage applied between drain and source electrodes
- V_t transistor threshold voltage

- V_g voltage applied to the gate electrode
- VL Vacuum Level
- W transistor channel width
- WF_m metal work function

Functional dielectric/semiconductor and metal/semiconductor interfaces in organic field-effect transistors

Contents

1. Introduction
    1.1. Overview on organic electronic devices
    1.2. The relevance of the interfaces
    1.3. Thesis organization
    References Chapter 1

2. Electronic structure of organic semiconductors
    2.1. π conjugated orbitals
    2.2. Energy levels in organic solids
    2.3. Charge injection in organic semiconductors
        2.3.1. Electronic structure of the Metal/Semiconductor interface
    2.4. Charge transport in organic materials
    2.5. Small molecules and polymers
        2.5.1. Small molecules
        2.5.2. Polymers
    References Chapter 2

3. OFETs device physics
    3.1. OFET device structure
        3.1.1. Materials employed for OFET fabrication
            3.1.1.1. The active material
            3.1.1.2. The electrodes
            3.1.1.3. The dielectric
    3.2. Working principles
        3.2.1. Origin of the field-effect
        3.2.2. Charge density distribution in an OFET
    3.3. Functional interfaces
        3.3.1. Metal/OS interfaces
        3.3.2. Dielectric/OS interface
            3.3.2.1. Film morphology and molecular organization
            3.3.2.2. Interfacial traps
            3.3.2.3. Polarity of the dielectric
    References Chapter 3

4. Experimental
    4.1. Film growth
        4.1.1. Vacuum sublimation
        4.1.2. Spin coating
    4.2. Contact angle measurements
    4.3. Thickness profiling
    4.4. Atomic Force Microscopy (AFM)
        4.4.1. AFM operating modalities
        4.4.2. The AFM instrument and the measures in this thesis
    4.5. Device fabrication

4.6. Electrical and optoelectronic measurements
4.6.1. Glove-box
4.6.2. Electrical measurements
References Chapter 4

5. Dielectric/semiconductor interface
5.1. Silicon dioxide dielectric
5.1.1. Wet cleaning
5.1.2. Plasma cleaning
5.1.3. HF eatching
5.2. Gas phase treatments of SiO_2 surface
5.2.1. 1,1,1-octadecyltrichlorosilane (OTS) treatment
5.2.2. 1,1,1,3,3,3-hexamethyldisilazane (HMDS) treatment
5.3. Dielectric polymer buffer layer
5.3.1. Poly(vinyl alcohol) [PVA]
5.3.2. Poly(methyl methacrylate) [PMMA]
5.3.3. Bisbenzocyclobutene derivative [BCB]
5.4. Dielectric/OS interface in PPVs based OFETs
5.4.1. Poly-phenylenevinylene derivatives
5.4.2. Electrical characteristics of PPV based OFETs
5.4.2.1. OFETs with pristine silicon dioxide
5.4.2.2. OFETs with gas phase treated silicon dioxide
5.4.2.3. OFETs with a polymer dielectric buffer layer
5.4.3. Morphological study of PPVs films
5.4.4. Conclusions on dielectric/PPV interface
5.5. Dielectric/OS interface in DHCO-4T based OFETs
5.5.1. α,ω-dihexylcarbonylquaterthiophene [DHCO-4T]
5.5.2. Electrical characteristics of DHCO-4T based OFETs
5.5.3. Early stages of DHCO-4T film growth
5.5.4. Conclusions on dielectric/DHCO-4T interface
5.6. Dielectric/OS interface in T3
5.6.1. Ter(9,9-diarylfluorene) [T3]
5.6.2. Preliminary field-effect characteristics of T3 based OFETs
5.6.3. Morphological study of T3 thin films
5.6.4. Conclusions on T3
References Chapter 5

6. Semiconductor/metal interface
6.1. Metals used as injecting electrodes
6.2. OS/metal interface in PPV based OFETs
6.3. OS/metal interface in DHCO-4T based OFETs
6.3.1. Electrical response of different metal contacts for DHCO4T based OFETs
6.3.2. Morphological study of the different metal contacts on top of DHCO4T films
6.3.3. Conclusion on metal/DHCO-4T interface
References Chapter 6

7. Future developments
7.1. Transparent electronic
7.2. Organic light emitting transistors
7.2.1. Doping the OFET active layer with chromophores
References Chapter 7

8. Conclusions

Appendix: Helicens
- Morphological study of helicens
    - 7-th
    - 7th-C3
    - ALK-Ph
    - TMT68
- Collaborations: Electrical responses
- Conclusions

  References Appendix

Chapter 1: Introduction

Organic semiconductors (OS) are considered promising materials for opto-electronics applications. The discovery of photo-electric effect in anthracene in 1906 by Italian scientist Pochettino[1] marks the beginning of studies in organic electronics. Studies on organic semiconductors started almost simultaneously with those on silicon, but low performance organic devices hindered at the beginning the development of an alternative technological platform. Furthermore, even today, there is no clear understanding of the charge transport mechanism in organic materials; the physical phenomena that govern the charge conduction is still largely unknown.

The peculiar characteristics of these materials reside in their structure, based on π-conjugated double bonds in a skeleton of carbon atoms. This particular chemical structure allows the delocalization of π-electrons over neighbouring carbon atoms and consequently enables the semiconducting nature of the materials.

The interest in OS stems from the characteristics offered by these materials: low cost and large area coverage, lightweight and flexibility. Moreover, organic materials offer the possibility of tailoring the chemical structure to change the chemical-physical properties and adapt the material functionality.

Extensive fundamental investigation on OS started in the late 1940s[2] but the interest in the possibility of using organic materials for applications in the electronics and semiconductor industry increased significantly over the last decades[3]. The great development achieved in organic device technology last the years opens new opportunities for the electronics market, currently dominated by silicon. Significant improvements were achieved in making organic light emitting diodes (OLEDs), organic photo-voltaic cells (PV) and organic field effect transistors (OFETs). Moreover, the combination of OLEDs and OFETs[4,5] is used to obtain an electroluminescent *pixel*, the key building block for active matrix display technologies. More recently, organic light emitting transistors (OLETs) [6-8] were also demonstrated, and this is an example of the possible integration of several functionalities in a single organic device.

1.1 Overview on organic electronic devices

Organic Light Emitting Diodes (OLEDs)

An organic light-emitting diode (OLED) is a solid-state device whose emissive electroluminescent layer comprises a film of organic material sandwiched between two electrodes. OLEDs can be based on thin films of organic small molecules or polymers that generate light when a voltage bias is applied between electrodes. Usually the two electrode materials are selected to favour hole (anode) and electron (cathode) injection. Generally the anode is made of ITO (Indium-Tin-Oxide, transparent material with high work function, ideal for hole injection) and the cathode of Al (low work function material, ideal for electron injection).

The birth of the OLED dates back to the 1960s when electrically driven light emission from non-crystalline organic materials was first observed[9,10]. After that, several studies were carried out by academic groups and companies (Kodak, Pioneer, Motorola, NEC, etc…) both for fundamental physics comprehension and application purposes.

The study of the OLEDs was so impressive and massive because they are, combined with transistors, the main component for flat panel displays. Nowadays electronic products containing displays are becoming more and more portable. Therefore, they need some peculiarities like lightweightness, flexibility, brightness, etc… These, with many others, are the strong points of the OLEDs. In fact they are thinner, lighter and more flexible with respect to their inorganic counterpart. Moreover, OLEDs can be as bright as LEDs and they consume much less power. Due to the organic processabilty, they are easier to produce and can be made to larger area. Finally OLEDs have large fields of view, about 170 degrees, a significantly advantage over, for example, liquid crystal displays. Obviously, these devices present also some disadvantages: they have typically shorter lifetime (in particular life time of the blue emitter is critical, about 1.000 hours), they are not very stable and can easily be contaminated by water or oxygen.

Most of organic materials (also the most highly emitting) show either p-type (hole) or n-type (electron) charge transport characteristics[11-18]. For this reason different organic materials are combined in a multi-layer architecture to improve the performances. It can thus be employed a material for hole transport, another one for electron transport and a third one for light emission (Figure 1).

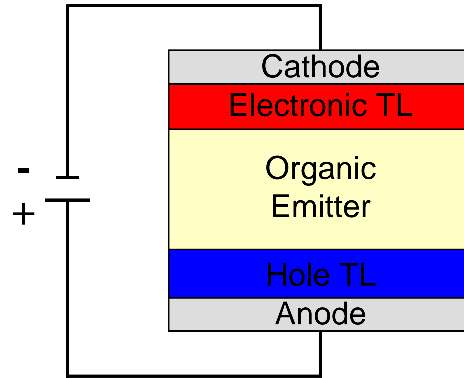

Figure 1: Scheme of a classic 3 layers OLED architecture.

To understand the basic working principles of an OLED we can use the example of a basic three-layer device (Figure 1). When a positive electrical potential is applied to the anode, the injection of holes occurs from this electrode into the hole transport layer (HTL), while the injection of electrons occurs from the cathode to the electron transport layer (ETL). The injected carriers move through the organic materials toward the oppositely charged electrode. The OLED works if the energy gap and the energetic positions of the Highest Occupied Molecular Orbital (HOMO) and Lowest Unoccupied Molecular Orbital (LUMO) (Chapter 2) levels of the materials are positioned as in the scheme of Figure 2. The hole injection from the HTL layer to the organic emitter is supported, ensuring hole blocking at the ETL one. Similarly, electron injection from the ETL to the organic emitter and the electrons blocking at the HTL is ensured. In these way we increase the probability of exciton formation and radiative recombination in the emitting layer.

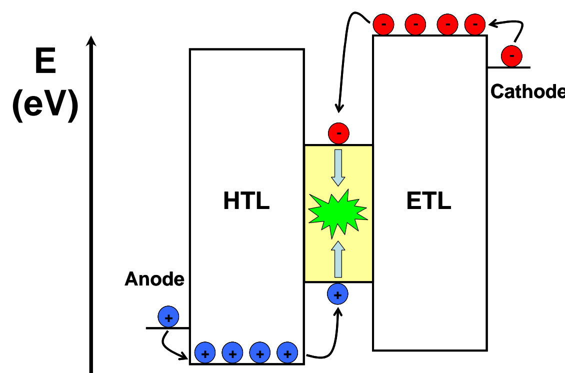

Figure 2: Scheme of energy levels for a three layers OLED. On the left the hole injection occurs in the hole transport layer (HTL). On the right the electron injection takes place in the electron transport layer (ETL).The radiative recombination occurs in the organic emitter (pale yellow).

<u>*Organic Photo-voltaic cells (PVs)*</u>

An organic photo-voltaic cell or solar cell is a device based on organic materials that converts light into electrical energy. The birth of the PVs dates back to 1959 when Kallmann and Pope observed a photo-voltaic effect in a single crystal of anthracene when sandwiched between two identical electrodes and illuminated from one side. These studies proceeded with the works of Geacintov, who discovered in 1966 the photo-voltaic effect in tetracene.

Nowadays commercial photo-voltaic devices are based on silicon because of its higher efficiency (about 20%) with respect to organics (about 5%). However, studies in organic photo-voltaic are in progress because of the unique characteristics of the organic materials (flexibility, light-weight, large area).

The first real organic PVs were made using small molecules, but soon after PVs based on polymers as active layers[19-25] were developed. The first organic solar cell were based on thermally evaporated molecular organic layer sandwiched between two metal electrodes of different work function (*single layer* PVs). Because the exciton diffusion length for most organic materials is below 20 nm, only the excitons generated near the contacts contribute to the photocurrent. For this reasons the *bilayer heterojunction* PVs (Figure 3.a) were made. In these devices a donor and an acceptor materials are stacked together with planar interface. The charge carriers separation occurs at this interface because of the large potential drop between the two materials. The bilayer is sandwiched between two electrodes with an appropriate work function to maximize the charge carrier collection.

Another possible architecture for a PV is the *bulk heterojunction* (Figure 3.b). Here there is a intimate mixture in the bulk between the two materials within a distance which is shorter than the exciton diffusion length. Therefore, there is a large increase of the interfacial area where charge separation occurs. Like in the previous cases the active layers are sandwiched between two appropriate work function electrodes.

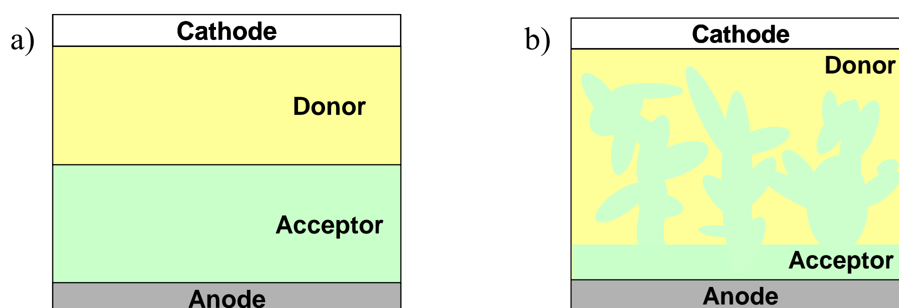

Figure 3: Schematic diagram of sandwiched PV cells: a) bilayer heterojunction cell; b) bulk heterojunction cell.

The working principle of the PVs cells is similar to the OLEDs one, but the goal is the opposite. Instead of using current for light generation, here we use light for current generation. The process of converting light into electric current is accomplished by four steps: *absorption of light*, which mainly depends on the absorption spectra, absorption coefficient and on the thickness of the OS; *exciton diffusion* to a region where the *charge separation occurs* and finally *charge transport to electrodes*. The overall photocurrent efficiency (η_j) could be factorized as the product of the fraction of absorbed photon (η_{abs}), the fraction of dissociated exciton (η_{diss}) and the fraction of charges that reach the electrodes[20] (η_{out}):

$$\eta_j = \eta_{abs} \times \eta_{diss} \times \eta_{out}$$

For a brief explanation of the device physics we consider a classic bilayer heterojunction. When the light reaches the device, it is absorbed by the donor OS with the consequent promotion of electrons from the HOMO to the LUMO of the material (Figure 4). The HOMO of the donor is lower in energy with respect to the Fermi level of the cathode (usually ITO) and therefore the holes can be collected at the electrode. Additionally, the LUMO of the donor (now rich of electrons) is higher in energy with respect to the LUMO of the acceptor favouring electron transfer to the acceptor material. The Fermi level of the anode (usually Al) is lower in energy than the LUMO of the acceptor and the electron can be collected at the Al electrode. If there is a closed external loop between anode and cathode the photocurrent starts to flow.

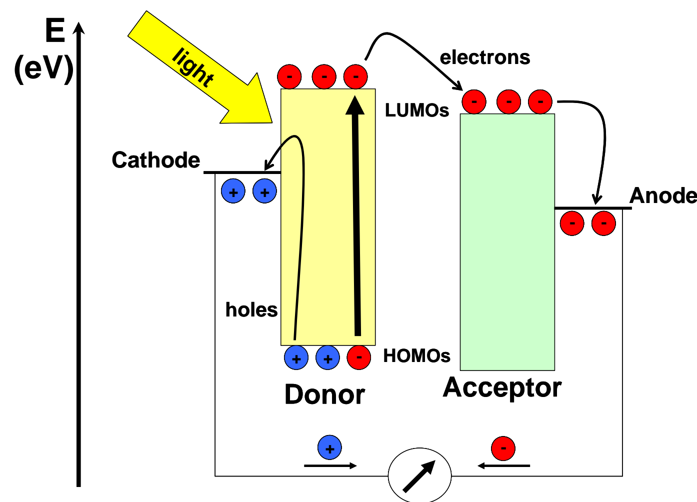

Figure 4: Schematic energy levels diagram of a bilayer PV. The external light generates holes in the HOMO and electrons in the LUMO of the donor. Holes are collected at the cathode, electrons move into the LUMO of the acceptor and are then collected at the anode.

<u>*Organic Field Effect Transistors (OFETs)*</u>

A transistor is a semiconductor device commonly used as an amplifier or an electrically controlled switch. The first field-effect transistor (FET) was inorganic and was invented in 1947 by John Bardeen, William Shockley and Walter Brittain. They received the Nobel prize in physics in 1956 for their research on semiconductor and the discovery of field-effect transistor. Since their discovery, transistors have dominated the mainstream microelectronics industry; in fact, they are the fundamental building blocks for basic analytical circuits. An Organic Field-Effect Transistor (OFET) is a transistor based on organic semiconductors.

The interest in using organic semiconductors as the active layers in FETs stemmed from the demonstration of field-effect conduction in small organic molecules[26,27] and conjugated polymers[28-30]. In 1986 the first OFET was reported by A. Tsumara [31]. From that moment a huge improvement in materials performances and development of new fabrication techniques took place[32].

OFETs are technologically attractive because all their layers can be deposited at low temperature and with low cost, in a large area and on a flexible substrate[33]. OFETs have also already been demonstrated in flexible electronic applications such as active matrix electronic paper displays[34,35] (Figure 5.a), sensors[36,37], and low-cost radiofrequency identification cards (RFIDs)[38,39] (Figure 5.b). In order to render these devices more suitable for various applications an important step will be the increasing of the charge carriers mobility. In fact the performances of OFETs are still lower with respect to those of the amorphous silicon devices. Mobility is about one order of magnitude lower in OFETs based on small molecules, and two order of magnitude lower in OFETs[40] based on polymers.

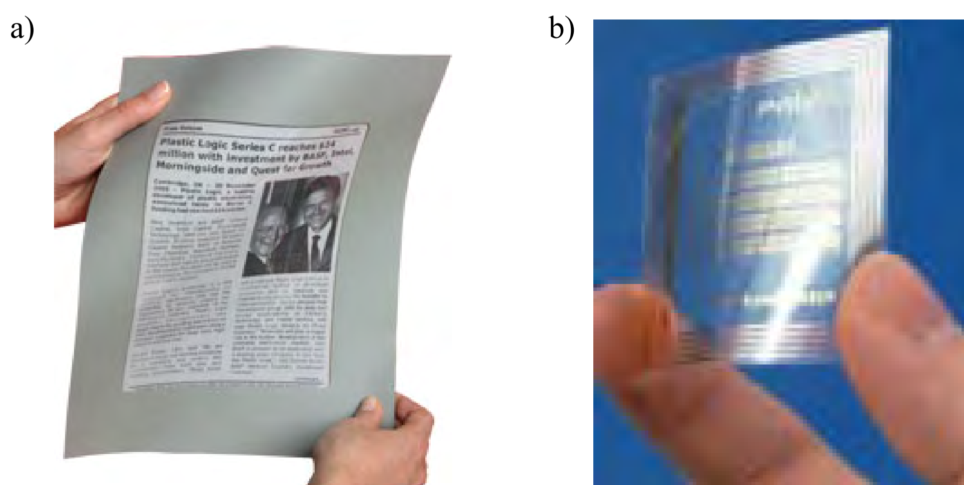

Figure 5: Example of: a) OFETs application for flexible active matrix electronic paper displays (image taken from[41]); b) low-cost radiofrequency identification cards (images taken from[42]).

In particular hole mobility on the order of 1 cm^2/Vs and 0.1 cm^2 /Vs was reached using respectively small molecules[43-45] and conjugated polymers[46-48] (Chapter 2) as OS material. However the highest mobility and most intrinsic charge transport properties in organic semiconductors are observed in single crystals, in particular, hole mobility of up to 20 cm^2/Vs is observed in rubrene[49]. Regarding electrons, mobility values of 1.7 cm^2/Vs for small molecules[50] and of about 0.1 cm^2/Vs for conjugated polymers[51,52] was recently reached.
This values are the highest reported, typical values are one or two orders of magnitude lower. In this respect the development of new materials for p and n-channel transistors continues to be a major area of research. In addition to high mobility values, the major objectives are: stability under ambient conditions and under bias stress, device to device fabrication reproducibility as well as easy processing, e.g., from solution, which would make organic semiconductors a viable alternative to amorphous silicon.

In the last years it became clear that the device performances can be improved by employing better controlled and higher purity materials, as well as through careful engineering of the device structure. There is a broadly shared understanding of the role played by interfaces in determining the device stability and reproducibility. The experimental part of this thesis mainly analyze the differences in electrical responses when different dielectric species or contact metals are used in OFETs based on the same OS.

1.2 The relevance of interfaces

From the previous description it is clear that all these devices are based on many different interfaces: metal/OS and OS/OS for OLEDs and PVs, metal/OS and OS/dielectric for OFETs. It is generally accepted that interfaces play a key role in determining the device stability and reproducibility. The control of each interface allows great improvement in the devices' performances and permits studying the fundamental physical ideas behind the devices working principles. This topic matters especially for OFETs that can be considered truly interfacial devices (Chapter 3).
Within this scenario we investigated the key OFET parameters in order to correlate the performance of the device with the functional interfaces.

1.3 Thesis organization:

The thesis is organized as follows:

In Chapter 2 an introduction on the electronic structure of the organic semiconductors is presented. The principles charge transport in organics are described. Then a brief explanation of the charge injection process is reported. Finally, a general description of the two main classes in which the OS are grouped (small molecules and polymers) is introduced.

Chapter 3 extensively describes the OFET devices, starting from the structures and introducing the working principles. The geometries of the OFETs, the classes of materials employed and, consequently, the interface involved are presented. The origin of the field-effect and the charge distribution in an OFET are examined, and the electrical parameters describing an OFET are reported. Finally, the reason why the dielectric/organic and metal/organic interfaces control is so important is discussed.

The experimental setup used are described in Chapter 4. In particular, the film growth techniques, the setups used for measuring the morphological, electrical, opto-electronic and chemical-physical properties of the devices we fabricated are introduced there.

Chapter 5 is focused on the study of the dielectric/semiconductor interface. In particular, the organic semiconductor and the dielectric species used in this work are introduced. Then we report the differences in the electrical field-effect response for different dielectric species in polymeric (Poly-phenylenevinylenes derivatives) and small molecules (oligothiopene and fluorene derivatives) based devices. In the small molecules based OFETs, we analyzed the early stages of the growth of the active layer via atomic force microscopy (AFM).

In Chapter 6, we move on to the second important OFET interface: the OS/metal contact one. We studied how different metals used for contacts influence the electrical performances of OFETs based on oligothiopene derivative. A preliminary study on a polymeric case is also reported. Our investigation includes a morphological study of the top of the metal contacts.

In Chapter 7 we hint some interesting future developments for organic electronics and in particular for OFETs advances. We introduce the possibility to obtain a totally transparent organic electronic device; and we report on the development of the Organic Light Emitting Transistors (OLETs). The possibility of doping the semiconducting or the dielectric layers in order to promote the light emission in OLETs is demonstrated.

In Chapter 8 a brief summary of the results and of their meaning reported.

The Appendix describes a new class of molecule based on the alternation of thiopene and benzene rings. In collaboration with the Northwestern University we studied the dielectric/OS interface via morphological and electrical analysis onto different substrates.

References Chapter 1:

[1] A. Pochettino, *Atti della R. Accademia di Lincei. Rendiconti della classe di scienze fisiche, matematiche e naturali*, vol. 15, 355, **1906**.

[2] M. Pope, C.E. Swenberg, *Electronic processes in Organic Crystals and Polymers*, Oxford University Press.

[3] J.B. Mullin, *Electronics Materials: From silicon to organics*, L.S. Miller.

[4] H. Sirringhaus, N. Tessler, R.H. Friend, *Science*, 280, 1741, **1998**.

[5] C.T. Kuo, S.Z. Weng, *Polymers for Adv. Tech.*, 13, 753, **2002**.

[6] A. Hepp, H. Heil, W. Weise, M. Ahles, R. Schmechel, H. von Seggern, *Phys. Rev. Lett.*, 91, 157406, **2003**.

[7] C. Rost, S. Karg, W. Riess, M. A. Loi, M. Murgia, M. Muccini , *Appl. Phys. Lett.*, 85, 1613, **2004**.

[8] R. Capelli, F. Dinelli, S. Toffanin, F. Todescato, M. Murgia, M. Muccini, A. Facchetti, T. J. Marks, *J. Phys. Chem. B.*, submitted;

[9] E. Gurnee, R. Fernandez, US Patent 3172862, **1965**.

[10] M. Pope, H. Kallman, P. Magnante, *J. Chem. Phys.*, 38, 2042, **1963**.

[11] J.H. Burroughes, D.D.C. Bradley, A.R. Brown, R.N. Marks, K. Mackay, R.H. Friend, P.L. Burns, A.B. Holmes, *Nature*, 347, 539, **1990**.

[12] A.P. Kulkarni, C.J. Tonzola, A. Babel, S.A. Jenekhe, *Chem. Mater.*, 16, 4556, **2004**.

[13] C.W. Tang, S.A. VanSlyke, *Appl. Phys. Lett.*, 51, 913, **1987**.

[14] D. Braun, A.J. Heeger, *J. Appl. Phys. Lett.*, 58, 1982, **1991**.

[15] U. Mitschke, P. Bauerle, *J. Mater. Chem.*, 10, 1471, **2000**.

[16] M.T. Bernius, M. Inabasekaran, J. O'Brien, *Adv. Mater.*, 12, 1737, **2000**.

[17] R.H. Friend, R.W. Gymer, A.B. Holmes, J.H. Burroughes, R.N. Marks, C. Taliani, D.D.C. Bradley, D.A. Dos Santos, J.L. Brédas, M. Logdlund, W.R. Salaneck, *Nature*, 397, 121, **1999**.

[18] J.R. Sheats, H. Antoniadis, M. Hueschen, W. Leonard, J. Miller, R. Moon, D. Roitman, A. Stocking, *Science*, 273, 884, **1996**.

[19] T.L. Benanti, D. Venkataraman, *Photosynthesis Research*, 87, 73, **2006**.

[20] H. Hoppe, N.S. Sariciftci, *J. Mater. Res.*, 7, 1924, **2004**.

[21] A. Goetzberger, C. Hebling, H.W. Schock, *Mater. Sci. Eng.*, 40, 1, **2003**.

[22] G.A. Chamberlain, *Solar Cells*, 8, 47, **1983**.

[23] D. Wohrle, D. Meissner, *Adv. Mater.*, 3, 129, **1991**.

[24] J.M. Nunzi, *C.R. Physique*, 3, 523, **2002**.

[25] P. Peumans, A. Yakimov, S.R. Forrest, *J. Appl. Phys.*, 93, 3693, **2003**.

[26] G.H. Heilmeier, L.A. Zanoni, *J. Phys. Chem. Solids*, 25, 603, **1964**.

[27] G. Horowitz, X.Z. Peng, D. Fichou, F. Garner, *Solid State Commun.*, 72, 381, **1989**.

[28] E. Ebisawa, T. Kurokawa, S. Nara, *J. Appl. Phys.*, 54, 3255, 1983.

[29] H. Koezuka, A. Tsumara, T. Ando, *Synth. Met.*, 18, 699, **1987**.

[30] J.H. Burroughes, C.A. Jones, R.H. Friend, *Nature*, 355, 137, **1988**.

[31] A. Tsumara, H. Koezuka, T. Ando, *Appl. Phys. Lett.*, 49, 1210, **1986**.

[32] C. Reese, M. Roberts, M.M. Ling, Z. Bao, *Mater. Today*, 20, **2004**.

[33] S.R. Forrest, *Nature*, 428, 911, **2004**.

[34] C. D. Sheraw, L. Zhou, J. R. Huang, D. J. Gundlach, T. N. Jackson M. G. Kane, I. G. Hill, M. S. Hammond, J. Campi, B. K. Greening J. Francl and J. West, *Appl. Phys. Lett.*, 80, 1088, **2002**.

[35] G.H. Gelinck, H.E.A. Huitema, E. Van Veenendaal, E. Cantatore, L. Schrijnemakers, J.B.P.H. Van der Putten, T.C.T. Genus, M. Beenhakkers, J.B. Giesbers, B.H. Huisman, E.J. Meijer, E. Mena Benito, F.T. Touwslager, A.W. Marsman, B.J.E. Van Rens, D.M. De Leeuw, *Nature*, 3, 106, **2004**.

[36] Z.T. Zhu, J. T. Mason, R. Dieckmann, G. G. Malliaras, *Appl. Phys. Lett.*, 81, 4643, **2002**.

[37] B. K. Crone, A. Dodabalapur, R. Sarpeshkar, A. Gelperin, H. E. Katz, Z. Bao, *J. Appl: Phys.*, 91, 10140, **2002**.

[38] W. Clemens, I. Fix, J. Ficker, A. Knobloch, A. Ulmann, *J. Mater. Res.*, 19, 1963, **2004**.

[39] D. Voss, *Nature*, 407, 442, **2000**.

[40] H. Sirringhaus, *Adv. Mater.*, 17, 2411, **2005**.

[41] http://www.editorsweblog.org/news/2006/01/flexible_e-reader.php

[42] http://www.ims.tnw.utwente.nl/research/devices/research_deveen.doc/

[43] M.M. Payne, S.R. Parkin, J.E. Anthony, C.C. Kuo, T.N. Jackson, *J. Am. Chem. Soc.*, 127, 4986, **2005**.

[44] K.C. Dickey, J.E. Anthony, Y.L. Loo, *Adv. Mater.*, 18, 1721, **2006**.

[45] J.E. Anthony, J.E., *Chem. Rev*, 106, 5028, **2006**.

[46] H. Sirringhaus, P.J. Brown, R.H. Friend, M.M. Nielsen, K. Bechgaard, B.M.W. Langeveld-Voss, A.J.H. Spiering, R.A.J. Janssen, E.W. Meijer, P. Herwig, D.M. de Leeuw, *Nature*, 401, 685, **1999**.

[47] J.F. Chang, B.Q. Sun, D.W. Breiby, M.M. Nielsen, T.I. Solling, M. Giles, I. McCulloch, H. Sirringhaus, *Chem. Mat.*, 16, 4772, **2004**.

[48] R.J. Kline, M.D. McGehee, E.N. Kadnikova, J.S. Liu, J.M.J. Frechet, M.F. Toney, *Macromolecules*, 38, 3312, **2005**.

[49] E. Menard, V. Podzorov, S.H. Hur, A. Gaur, M.E. Gershenson, J.A. Rogers, *Adv. Mater.*, 16, 2097, **2004**.

[50] R.J. Chesterfield, J. McKeen, C.R. Newman, P..C. Ewbank, C.D.J. Frisbie, *Phys. Chem. B*, submitted.

[51] A. Babel, S.A. Jenekhe, *Adv. Mater.*, 14, 371, **2002**.

[52] A. Babel, S.A:. Jenekhe, *J. Am. Chem. Soc.*, 125, 13656, **2003**.

Chapter 2:

Electronic structure of organic materials

This section reports a brief explanation of active materials electronic characteristics. Starting from the carbon atom, across a description of the π-conjugation, the electronic energy level structure of organics is introduced. Besides, the charge injection and transport in these materials is considered. At last, an overview of the main classes of organic semiconductors is reported.

2.1 π conjugated orbitals

An organic material is a system based on carbon atoms. Organic semiconductors are organic materials that exhibit semi-conducting properties.

Most attractive opto-electronic properties of these materials arise from the carbon atom features. In its ground state, the carbon atom has this classic electronic structure: $1s^2 2s^2 2p_x^1 2p_y^1$. This means that carbon has two electrons in orbital 1s, two in orbital 2s (Figure 6.a) and 2 in orbitals 2p (figure 6.b). Therefore, the s orbitals are totally filled, and with this configuration carbon should form only two bonds. Instead, it is well known that carbon is tetravalent and forms four bonds. This can be explained using the valance bond theory[1].

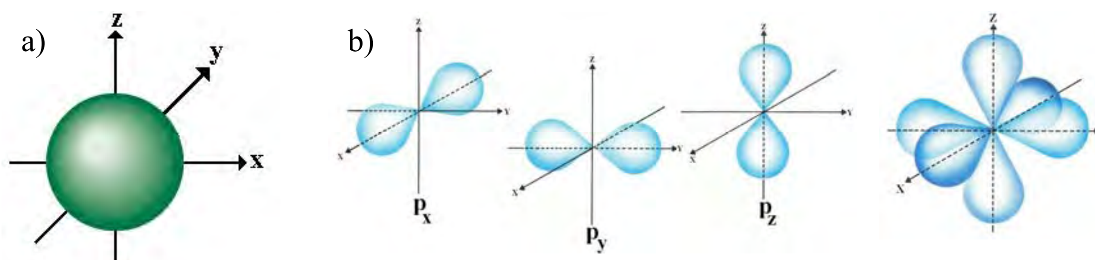

Figure 6: a) Spherical shape of s orbital; b) Representation of the 3 p orbitals (p_x, p_y and p_z) and of their spatial combination

This theory asserts that a chemical bond is formed by the overlapping of the atomic orbitals which contain the electrons participating in the bond, in order to lower the total energy of the system. The atomic orbitals are the wave functions solving the Schrodinger equation for an atom; therefore, the overlapping of atomic orbitals corresponds to the combination of the wave functions of the two electrons involved in the bond.

The wave function describing a molecular system, if ϕ_i are solutions of the Schrodinger equation, can be expressed as:

$$\psi = \sum_i a_i \phi_i \quad \text{with} \quad \sum_i a_i^2 = 1$$

is a generic normalized solution of the wave function, and is called *hybrid orbital*. The orbital superimposition described is a *linear combination of atomic orbitals* (LCAO) and gives as result a *molecular orbital* (or molecular wave function).

In the case of carbon, we can combine the 2s orbital with one, two or three of the 2p orbitals. If the mix occurs between the 2s orbital and all the 2p orbitals, we obtain four degenerate sp^3 hybrid orbitals lying in a tetrahedral geometry around the central carbon atom (109,47° between bond axes, Figure 7).

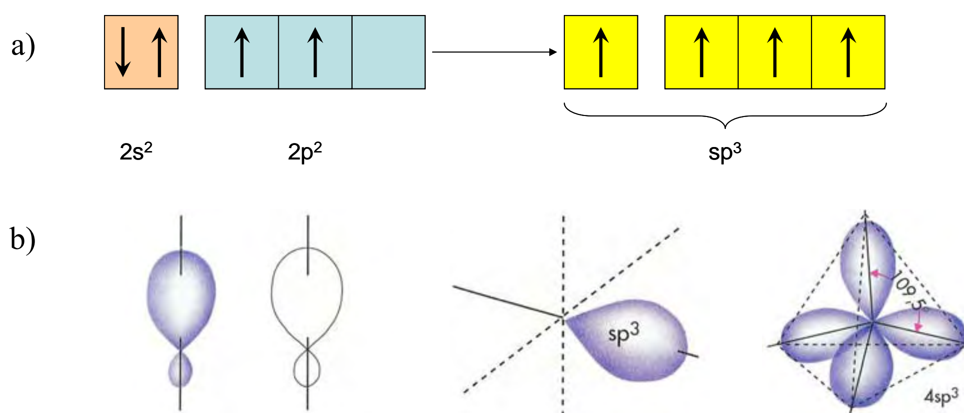

Figure 7: a) Electronic scheme of the sp^3 hybridization; b) two profiles of the shape of the sp^3 orbitals and the tetrahedral symmetry of a sp^3 carbon (image adapted from[2]).

Mixing can also occur between 2s orbital and one 2p orbital to form 2 equivalent sp orbitals. These are on the same plane (α) passing through the nucleus, and lie at 180° from one each other. The 2 pure p remaining orbitals lie in a plane which is perpendicular to the former (β) (Figure 8).

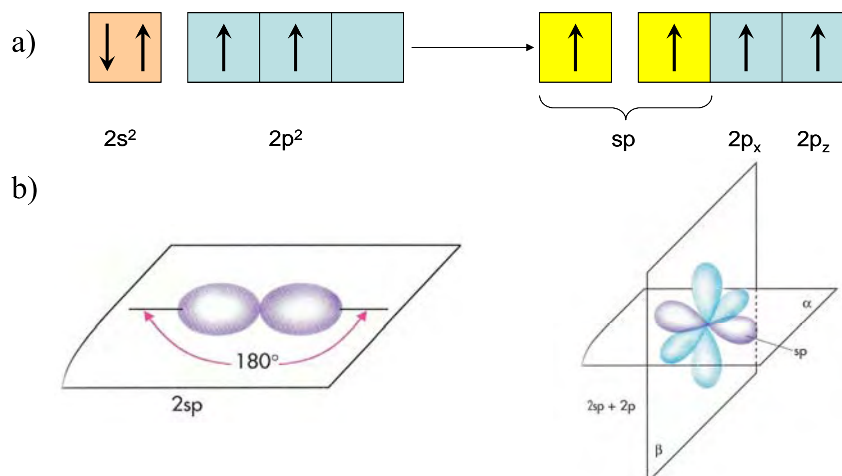

Figure 8: a) Electronic scheme of the sp hybridization; b) spatial distribution of the sp hybrid orbitals and of the spatial combination of the 2 sp hybrid orbitals and the 2 pure p orbitals (image adapted from[2]).

If the mixing occurs between the 2s and two 2p orbitals, we have three new sp^2 hybrid orbitals on the same plane (α) at 120°, leaving an unaltered p orbital on a plane lying perpendicularly to the hybridization one (β) (Figure 9).

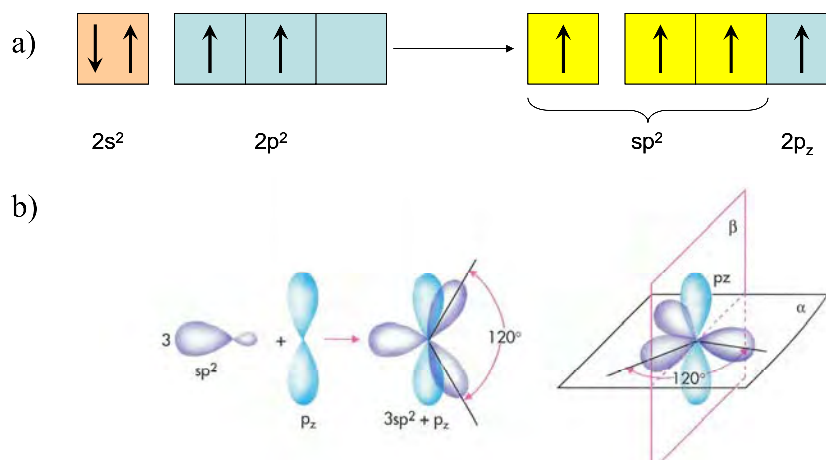

Figure 9: a) Electronic scheme of the sp^2 hybridization; b) the sum of 3 sp^2 hybrid orbitals and a pure p orbital with the resultant spatial combination (image adapted from[2]).

In each one of the above mentioned cases the mixing of these orbitals increases the bond strength between equivalent carbon atoms, thus giving back the energy required to promote the hybridization.

The sp^2 hybridization, as explained below, originates the semiconducting nature of the organic materials, and is the key to understand the possibility of charge transport in organic materials. When two sp^2 hybridized carbon atoms mutually approach, then an sp^2 orbital of the first atom could overlap an sp^2 orbital of the second, thus forming a σ molecular orbital

(or σ bond). Furthermore, the two pure p orbitals of the two carbon atoms could partially overlap, in order to form a second molecular orbital, the π one (or π bond). Overall, we have a double bond leaving the two other sp^2 atomic orbitals of each carbon atom free to form other bonds (Figure 10).

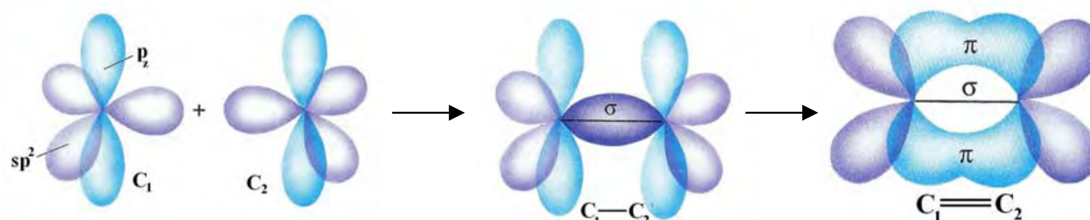

Figure 10: formation of σ and π bonds between two carbon atoms hybridized sp^2 . Electron density spatial distribution is shown (image adapted from[2]).

An alternating arrangement of single and double bonds is called *conjugated system*. This system is responsible for the organic materials semiconducting nature. In fact, in the σ bonds electrons are localized in the region between the nuclei, whereas in the π bonds they are delocalized. This means that electrons are not confined between the nuclei, rather they form an electron density cloud above and below the plane of the σ bond (Figure 10). This cloud creates an electron system ideally delocalized over the entire molecule or polymer. In real cases, this delocalization can be confined in only a part of the molecule[3]. As a matter of fact, conjugation exists, and, as we will see below (Section 2.2), it largely determines the electron energy structure of the organic materials.

2.2 Energy levels in organic solids

Organic solids are formed by an ensemble of many molecules. Properties of solids can be related to those of free molecules. As just explained (Section 2.1), the electron energy structure for molecules can be described by molecular wave functions. Each molecule owns a ground-state electronic wave function (ψ) and many excited-state wave functions (ψ^s) distinguished from the superscripts. Each molecule in a solid lies in a defined position, recognizable by the site and the unit cell. Thus, the molecule that occupies the *lth* states of the *mth* unit cell and is in its ground-state has a wave function ψ_{lm}; otherwise if is in an excited states has a wave function: $\psi^s{}_{lm}$.

The energy of such a solid can be described by a simple Hamiltonian (h), the operator that corresponds to the total energy of the system. With the approximation that electronic energy levels of the crystal are determined by the equilibrium positions of the molecules in the lattice and are slightly disturbed by lattice vibrations, it is possible to definine for the equilibrium configuration of the lattice h as[4]:

$$h = \sum_{k=1}^{N} \left(H_k + \sum_{l>k} V_{lk} \right)$$

with H_k the Hamiltonian for the kth molecule, V_{kl} the interaction operator for molecules l and k, and N the number of molecules in the solid. The intermolecular potential energies (represented by the V_{kl} terms) are small compared with intramolecular energy terms (H_k) and can be treated as perturbations. Thus, if the *tight-binding approximation* is used (this approximation treats a solid as an extended molecule, then the molecular wave functions are spread throughout the solid[5]), the free-molecule Hamiltonians define the unperturbed problem, and the basis functions are the wave functions of free molecules, namely the sets ψ_{lm} and $\psi^s{}_{lm}$ for all the molecules in the crystal. If all the molecules are in their ground-state the solid is in its unperturbed state and its wave function is a simple product of molecular wave functions:

$$\Phi_{GS} = \psi_{11}\psi_{12}.....\psi_{21}.....\psi_{q\ N/q}$$

with q the number of molecules in each unit cell and consequently N/q the total number of unit cells.

A different situation occurs for the excited states of the solid. The unperturbed wave function for the lowest states corresponds to the excitation of one molecule only. Excitation of the pth molecule of the ith translational set is represented by a localized excitation wave function:

$$\phi_{ip}^{r} = \psi_{11}\psi_{12}.....\psi_{ip}^{r}.....\psi_{q\ \ N/q}$$

There are N such functions, each for the excitation of one of the molecules in the solid. Each is of the same energy, giving N-fold degeneracy. The solid wave functions for the problem including the intramolecular perturbations are described by the expansion:

$$\Phi^{r(j)} = \sum_{ip} c_{ip}^{r(j)} \phi_{ip}^{r}$$

There will be N such solid states for a chosen molecular excited state *r*, each specified by a value of the index *j*. The coefficients $c_{ip}^{r(j)}$ can be determined by minimizing the energy of the system.

The simplest case that can be treated is the dimer formation. In this situation two identical molecules (1 and 2) bond and the Hamiltonian of this system is: $h = H_1 + H_2 + V_{12}$, with H_1 and H_2 the Hamiltonian for the molecules 1 and 2 and V_{12} the interaction operator. The dimeric wave function for the ground-state case is $\Phi_{GS} = \psi_1\psi_2$. From the Schrodinger equation the relative degenerate energies are:

$$E_{GS} = E_1 + E_2 + \left\langle \psi_1\psi_2 \left| V_{12} \right| \psi_1\psi_2 \right\rangle$$

with $E_1 = E_2$ the energies of the isolated molecules.
As before, different situation occurs for the excited states. The excited state wave function is:

$$\Phi_{EX} = C_1\psi_1^{*}\psi_2 + C_2\psi_1\psi_2^{*} \qquad \text{with} \quad |C_1| = |C_2|$$

where ψ_1* and ψ_2* are the wave functions for the excited molecules 1 and 2.
If it is consider only one molecules excited, the energies of the system are:

$$E(\pm) = E_1^{*} + E_2 + W' \pm \beta$$

with:

$$W' = \left\langle \psi_1^{*}\psi_2 \left| V_{12} \right| \psi_1^{*}\psi_2 \right\rangle$$

$$\beta = \left\langle \psi_1^{*}\psi_2 \left| V_{12} \right| \psi_1\psi_2^{*} \right\rangle$$

W' is the Coulomb interaction between the excited molecule 1 and the molecule 2 and β is the excitation exchange integral that considers the possible excitation exchange between the identical molecules.
This description can be summarized in an energy level diagram (Figure 11) where the energy levels of the free molecules are lowered by the Coulomb interaction and the degeneracy is removed by the exchange integral.

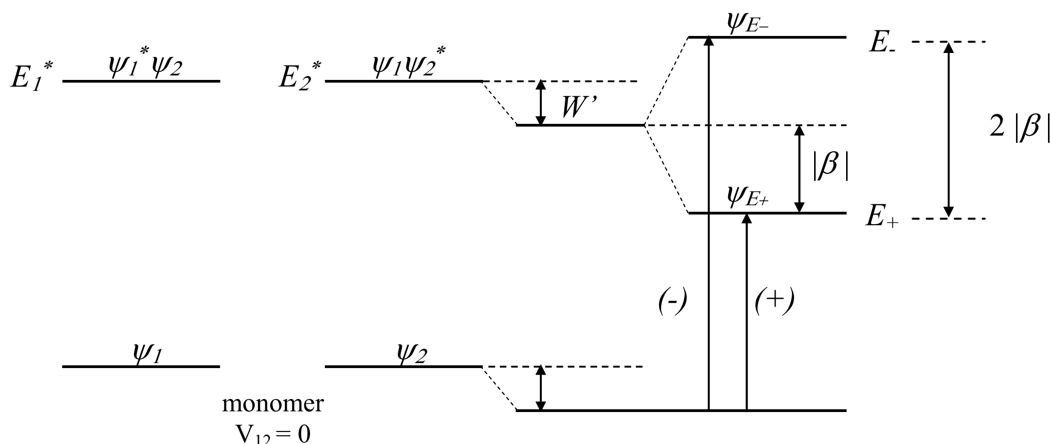

Figure 11: Energy level diagram for a dimer with identical molecules.

The dimer case can intuitively be extended to a many molecule system: a solid. In a such situation a huge number of levels with different energy are present forming narrow energetic intervals (narrow bands). Some levels, with low energy, are filled by electrons, and others, with higher energy, are empty. In a molecule (as in a solid), the highest energy filled molecular orbital is called HOMO (*Highest Occupied Molecular Orbital*) and the lowest energy empty molecular orbital is called LUMO (*Lowest Unoccupied Molecular Orbital*). The energy difference between these two orbitals is called *energy gap* (E_g).

In the case of sp^2 hybridized carbon, C atoms bond together, forming an alternation of single and double bonds: a conjugated system. When the length of the conjugation sequence in a molecule increases, the average level of delocalisation of π bonds increases too, and energy gap consequently decreases (Figure 12). This allows easier promotion of electrons from the HOMO to the LUMO leaving free charge carriers for the conduction. The gap remains finite in the long chain limit because of the Peierls instability or defects presence.

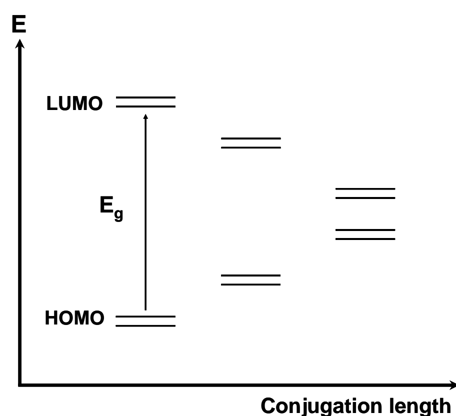

Figure 12: Differences in energy between HOMO and LUMO as a function of conjugation length.

2.3 Charge injection in organic semiconductors

One of the main issues in device physics is the description of the effects of the metallic contacts, and therefore the nature of the charge injection. Historically, studies on charge injection started from the work of Richardson and Dushman, who explored the injection from a metal to an insulator[6,7] using the thermoionic emission theory[7]. Later, their work was modified by Bethe and Schottky[8] for charge injection at the interface between a (crystalline inorganic) semiconductor and a metal. The calculation is done on the assumption that electrons in the semiconductor are freely propagating in the conduction band, with a thermal distribution of kinetic energies. Extending these theories to organic semiconductors is difficult, because conduction occurs via hopping and not via propagation in extended states as in the inorganic case; nevertheless, this problem was treated by Emtege and O'Dwyer[9].

The OS/metal contact interface is usually treated as a Mott-Schottky barrier, where the barrier height is given by the difference between the metal work function (WF_m) and the semiconductor Highest Occupied Molecular Orbital (HOMO) for hole injection; or between WF_m and Lowest Unoccupied Molecular Orbital (LUMO) for the electron injection. The barrier is formed after the contact between the metal and the semiconductor, and physically consists of a region of uncompensated charge. This "space charge" causes a voltage drop at the interface. From the energetic point of view, there is a bending of the energetic levels of the semiconducting material at the interface, as metal creates a gap with respect to the metal work function. When the WF_m and the electronic level of the semiconductor are energetically closer, a good ohmic contact is achieved. In the case of non-ohmic contacts, a high potential barrier is formed, thus leading to poorly efficient charge injection. This is the reason why low work function metals (e.g. Ca) are commonly used for n-type channel OFET (WF_m close to the LUMO of the organic semiconductor, for an easier electron injection), while high work function metals (e.g. Au) are used for p-type conductor (WF_m close to the HOMO of the organic semiconductor, for an easier hole injection). In spite of the large effort put in the investigation of the contact effect, a severe lack of understanding remains about a number of issues, such as the high contact resistance values and the device irreproducibility. This happens because, beyond the energy levels matching, other parameters play important roles: the grain boundaries present at the metal/semiconductor interface, the penetration of metal clusters inside the organic soft material during the metal deposition, the possible local fluctuation of the metal work function due e.g. to local oxidation, the traps presence at the interface, etc…

Although the simple Mott-Schottky model provides a guideline for choosing appropriate injecting electrodes (Section 2.3.1), it is not sufficient to describe properly the charge injection into organic semiconductors. Therefore, many models were proposed to accomplish this theory: thermally assisted tunnelling from the metal to localized states[10], tunnelling into polaron levels[11], thermally assisted injection into an energetically disordered dielectric[12], or diffusion-limited thermoionic emission[13].

2.3.1 Electronic structure of the Metal/Semiconductor interface

This section contains a brief overview of the conceptual aspects of charge injection. In order to understand the idea of charge injection, we have to introduce some basic concepts of solid state physics. Starting from the beginning, it is important to recall that the vacuum level (VL) is defined as the energy level above which an electron can escape from the solid. Analyzing the easiest interface, metal/vacuum, it has to be noticed that a surface dipole layer is formed due to the tailing of the electron cloud at the metal surface (Figure 13). This makes the vacuum side of the interface negative, obviously leaving the metal one positive[14].

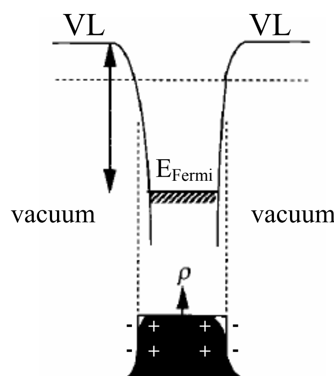

Figure 13: Potential surface for an electron at the metal/vacuum interface (top); tailing of the electronic cloud at the metal surface (bottom)[14].

The idea is similar also in metal/OS interfaces and when the two solids come into intimate contact, the organic material is in the potential rise from the tail of the metal electron cloud. Thus, its energy level raises up to a common VL in a very narrow interfacial gap. In this configuration a simplistic energy levels diagram can be used, in which the energy barrier for the electron injection (Φ_B^n, Figure 14.b), and the energy barrier for the hole injection (Φ_B^p, Figure 14.b) can be easily calculated (Equation 2 and 3).

Such energy level diagram describes in a simple way the interface between a metal and a thin organic film, in which the total number of mobile carriers in the organic material is low.

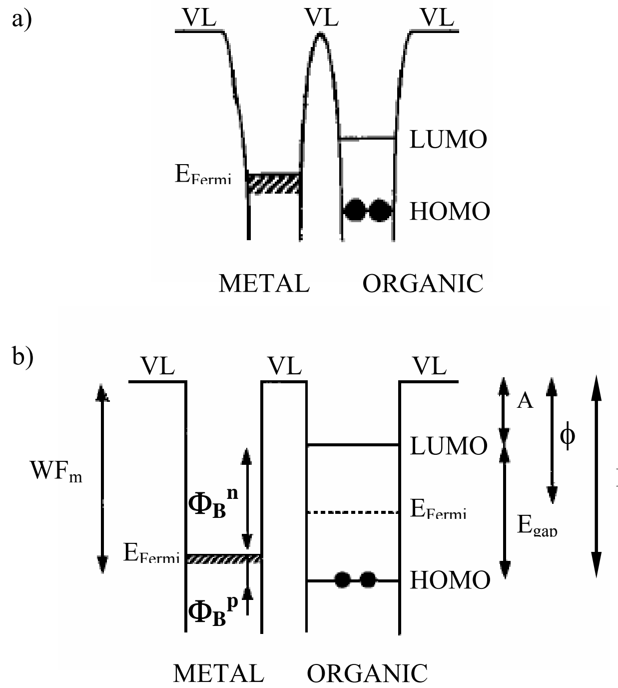

Figure 14: a) Ideal electronic structure of a metal/organic semiconductor interface; b) Schematic representation of the same interface including some interesting physical parameters as metal work function (WF_m), organic semiconductor electron affinity (A), ionization energy (I) and band gap (E_{gap}) energy[14]. Φ_B^p and Φ_B^n are the energy injection barrier for holes and electrons and ϕ the work function of the organic material.

In an interface with a "thick" organic film (typical case for the majority of the OFETs) band bending should be also considered. In this case there are usually several charge carriers in the OS. The metal/OS interface is not in equilibrium (Figure 14.b, the WF_m is larger with respect to the work function of the organic material, ϕ); therefore, some electrons could move through the interface from the organic to the metal. A negative charge appears on the metal side and a positive one on the organic side. This charge redistribution obstructs further electron movements from OS to metal, which stop when the two Fermi levels are aligned. The potential distribution at the interface is governed by the Poisson equation, that expresses the relation between the charge density (ρ) and the potential distribution, V:

$$\nabla^2 V = -\frac{\rho}{\varepsilon} \tag{1}$$

where $\nabla^2 = \frac{\partial^2}{\partial x^2} + \frac{\partial^2}{\partial y^2} + \frac{\partial^2}{\partial z^2}$ is the Laplace operator and ε the dielectric constant of the medium.

As a result, a diffusion layer (W) with band bending is formed to align the Fermi energies of the two solids, hence building up the organic layer potential (V_{bi}, Figure 15).

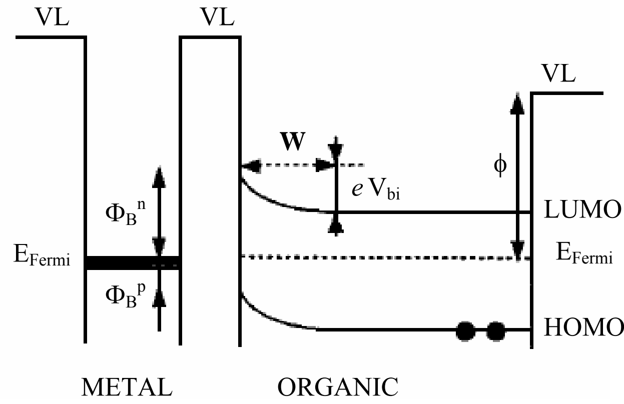

Figure 15: Energy level bands bending in a metal/thick organic layer interface. A diffusion layer of thickness W compares within the bands bending.

Equations for the hole and electron injection are easily express from the physical properties of the system as:

$$\Phi_B^p = I - WF_m \quad (2)$$

and

$$\Phi_B^n = WF_m - A = E_{gap} - \Phi_B^p \quad (3)$$

that are the Schottky-Mott classic equations for simple contacts. I and A are respectively the organic semiconductor ionization energy and electron affinity.

The model described above is valid for an ideal system without dipoles presence. In reality, a dipole layer is present, because the tail of the metal electron cloud is not well confined inside the metal, as already discussed. Furthermore, in real systems this is strengthened by further dipole sources, due to many factors. For this reasons, a more realistic treatment has to be carried out (Section 3.4.1).

2.4 Charge transport in organic materials

In organic semiconductor materials charge carriers are rather localized on individual molecules, with the consequence of considerable local changes in nuclear position, vibrational frequencies and electronic wavefunction by polarization interaction: we have *polarons*. A polaron can be described as an electron dressed with its nuclear deformation[15,16].
The bulk transport occurs by hopping of charges between localized states, thus a new concept has to be introduced: the *polaron hopping*. The charge transport in the organic materials is allowed by movements made by polarons along the conjugation, and by the jump of the charge carriers from one molecule to a neighbour, or from a polymer chain to a near chain (Figure 16). This is the concept of hopping conduction.

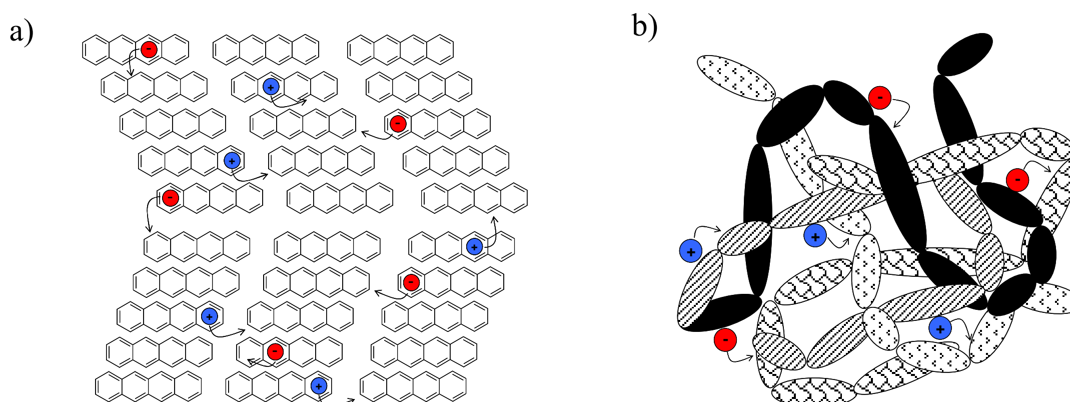

Figure 16: Scheme of electrons and holes hopping conduction. Holes are represented by blue circles and electrons by red circles. (a) Small molecules case (e.g. tetracene, that is an ambipolar materials): intramolecular and intermolecular hopping in a crystalline structure. (b) Polymers case: intra-chain (along chains) and inter-chain (between different chains) hopping in an ideal ambipolar polymer.

Each polaron can be described by its generalized configurational coordinate (Q) and from an energetic point of view by its Hamiltonian (*H*), that is a function of Q. In the case of a localized state without interactions between nearest-neighbour, the total energy of the excess carrier (or of the polaron) residing in a given molecular site is[17]:

$$E(Q) = E_0 - AQ + BQ^2 \tag{4}$$

where A>0 is the local electron-phonon coupling constant (energy/distance), BQ^2 represents the elastic energy produced by the lattice distortion, and E_0 is the carrier energy in absence of phonons. The linear phonon-electron interaction lowers the carrier energy of $E_b = A^2/4B$ (*zero-order polaron binding energy*) by altering the local configuration of the lattice, so that

minimum energy is achieved. This corresponds to a change in the equilibrium position from $Q=0$ to $Q_0 = A/2B$ (Figure 17). The electron and its associated local distortion as a whole are called *localized polaron*.

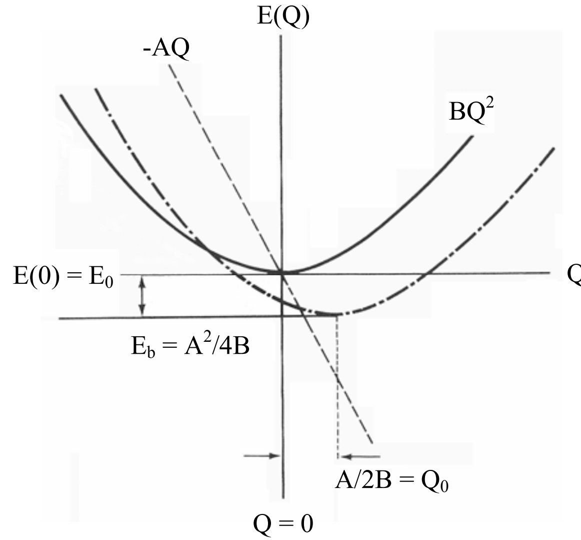

Figure 17: The total energy of a polaron, E(Q), in a solid as a function of the configurational coordinate, Q[17].

Transfer between different molecular sites occurs when the configuration of lattice atoms offers the same energy on both site. The linear phonon coupling does not alter the phonon frequencies[18], so B is unchanged and the condition of equivalent electron energy for two different sites is $AQ_1 = AQ_2$, and so $Q_1 = Q_2$. This configuration is allowed as a result of thermal fluctuations, with a probability proportional to $\exp\left(-W_a/kT\right)$ where W_a is the activation energy. The energy needed to distort both molecules in order to obtain a $Q_1 = Q_2$ configuration is:

$$W_a = B(Q_0 - Q)^2 + BQ^2 \qquad (5)$$

The minimum activation energy occurs when $Q = Q_0/2 = A/4B$. In this description, when the effects of the intermolecular coupling are neglected, the activation energy is $W_a = \frac{1}{2} BQ_0^2 = \frac{1}{2} A^2/4B = \frac{1}{2} E_b$. If we consider disordered systems, there will be spatial variation in E_0. If δW denotes the difference in the electron site energy between two molecular sites, the W_a (always without intramolecular effects) is[19]:

$$W_a = \frac{E_b}{2} + \frac{\delta W}{2} + \frac{(\delta W)^2}{8 E_b} \qquad (6)$$

So far the discussion was limited to the case of a localized small polaron. If there is an interaction energy (J) between neighboring molecules, the energy degeneracy at X (as shown in the previous case) is lifted, giving rise to new states (X_1 and X_2, Figure 18). The activation energy for transfer is lowered from X to X_1 and the new potential energy barrier for the charge motion is $W_a^{'}$.

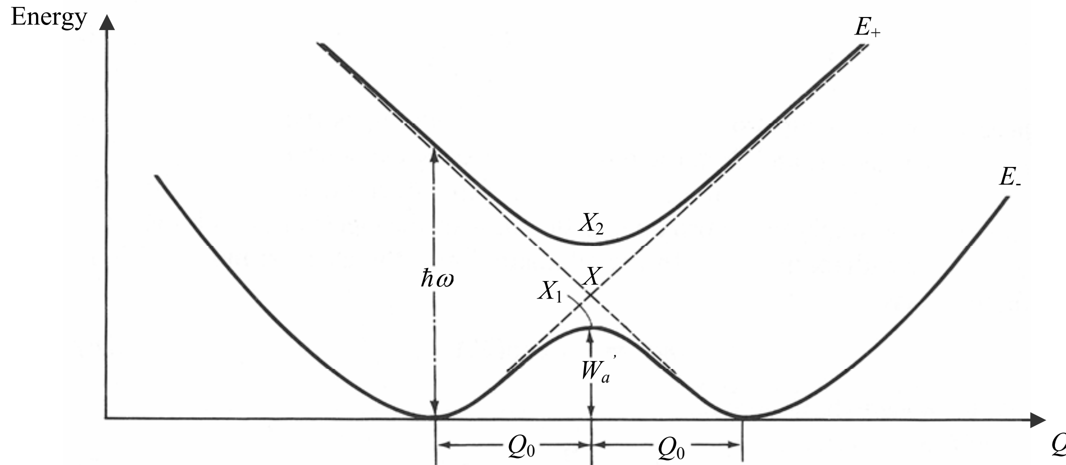

Figure 18: The activation energy ($W_a^{'}$) of a small polaron in a two-site system as a function of Q. Its adiabatic energies (E_+ and E_-, here $E_b = BQ_0^2$)[17].

If the magnitude of J is so large that the transition between E_- and E_+ is improbable, the carrier moves *adiabatically*[19]. Otherwise, if J is small enough to allow the transition, the transfer is called *nonadiabatic*[20].

The temperature dependence of mobility will be different in each one of the two cases. At low temperatures *J* is the dominant factor, and the motion is band-like, with the polarons moving with different effective mass[20,21] in either case.

As T increases, the polaron bandwidth narrows. Eventually, at a temperature T_c lifetime broadening caused by other scattering processes, e.g., defects and electron-phonon interactions, is comparable to or larger than the polaron carrier bandwidth. In this limit, inelastic scattering dominates with the corresponding absorption and emission of phonons. Now, we have to consider the motion of the carrier as a sequence of uncorrelated hops. The hopping mobility can be written[22]:

$$\mu = \frac{ea}{kT} P \tag{7}$$

where *a* is the spacing between hopping sites and P the hopping probability per unit time[23,24].

For adiabatic transfer $W_a^{'} << \frac{1}{2}E_b$ because $W_a^{'} \approx \frac{1}{2}E_b - J$ with $J > 0$ and larger than or comparable with the polaron binding energy. The hopping probability P is now thermally activated and is $P = \omega_0 \exp\left(-\frac{W_a^{'}}{kT}\right)$. So, substituting in eq. (7):

$$\mu = \frac{ea}{kT}\omega_0 \exp\left(-\frac{W_a^{'}}{kT}\right) \tag{8}$$

In the nonadiabatic limit $W_a^{'} \approx \frac{1}{2}E_b$ and for the narrow-phonon-band limit of $\omega_q = \omega_0$ (ω_q being the frequency of the polaron band and ω_0 the phonon frequency) the expression of mobility is:

$$\mu = \frac{ea^2}{kT}\frac{1}{\eta}\left(\frac{\pi}{2E_b kT}\right)^{1/2} J^2 \exp\left(-\frac{E_b}{2kT}\right) \tag{9}$$

Eq. (8) and (9) assume that the lattice relaxing between jumps is rapid enough for successive hops to be uncorrelated. If the lattice does not relax, then the memory of the site of the last occupation persists, and the carrier is likely to return, hence dropping mobility; if the lattice relaxes, then there is no memory of past occupation[17].

Several models rationalizing the hopping transport were developed. In most cases temperature dependence was taken into account, and mobility equations have the form[25,28]: $\mu = \mu_0 \exp\left[-\left(\frac{T_0}{T}\right)^{1/\alpha}\right]$ where α is an integer ranging from 1 to 4 (indicating the dimensionality of the system), T_0 is inversely proportional to the density of states at the Fermi level and μ_0 is a mobility pre-factor.

A useful model to describe the charge transport in organic materials is the *polaron model*, developed by Holstein, Fesser and Marcu[26,27,29]. The idea was that the charges move by thermal activated hops between adjacent sites. The transition rate from a *i* site to a *j* site for polarons is given by[29]:

$$\upsilon_{i\to j} \propto \frac{1}{\sqrt{E_r T}} \exp\left[-\frac{\left(E_j - E_i + E_r\right)^2}{4E_r kT}\right] \tag{10}$$

where E_i and E_j are the energies of the *i* and *j* sites and E_r is the intramolecular reorganization energy. The mobility of the charges in this model is field (F) and temperature (T) dependent:

$$\mu = \mu_0 \exp\left[-\frac{E_r}{4kT} - \frac{(aF)^2}{4E_r kT}\right]\frac{\sinh(aF/2kT)}{aF/2kT} \quad (11)$$

where μ_0 is a pre-factor slightly temperature dependent.

Another model used for amorphous organic materials employed as active layers in transistors is the *multiple trapping and release model (MTR model)*[30]. In this model a narrow delocalized band is associated with a high concentration of localized levels acting as traps. During their transit through the delocalized levels, the charge carriers interact with the localized levels through trapping and thermal release. To elaborate an expression for mobility, two assumption are made: when the carriers injected, or already present in the organic semiconductor, arrive on a trap, they are immediately trapped with probability close to one and the release is controlled by a thermally activated process. The drift mobility (D) is given by:

$$\mu_D = \mu_0 \alpha \exp\left(-\frac{E_t}{k_B T}\right) \quad (12)$$

where μ_o is the mobility in the delocalized band, α is the ratio between the effective density of states at the transport band edge and the density of traps. In the case of single trapping level, E_t corresponds to the distance between the trap level and the delocalized band edge. This model is commonly used in amorphous silicon transistors, but it was extended to organic systems as well.

In the MTR model transport is governed by the activation to a transport level. Another model in which hopping is the driving force of the transport is the *variable range hopping model (VRH).* This model is preferentially used for polymers and it is based on the Miller-Abrahms model. It assumes that electron-lattice coupling is weak and when the model is applied to polymers it considers the conjugated segments as analogous to nearly isolated impurity states. With this assumption, the hopping rate from an occupied site i to a neighbouring unoccupied site j is:

$$\upsilon_{ij} = \upsilon_0 \exp\left[-2\gamma a\left(\frac{R_{ij}}{a}\right)\right]\begin{cases}\exp\left(-\frac{E_{ij}}{k_B T}\right) & E_{ij} > 0 \\ 1 & E_{ij} < 0\end{cases} \quad (13)$$

where R_{ij} is the distance between the two sites, E_{ij} the two sites separation in energy, γ is related to the inverse wavefunction decay constant of an energy state and a is the average lattice constant. This idea was extended by Mott[31] to include hops over greater distances. So, the carriers might hop over long distances with low activation energy and over small distances

with high activation energy. This is the foundation of the VRH models, which result in an expression where mobility depends from temperature:

$$\mu \propto \exp\left[-\left(\frac{T_0}{T}\right)^{1/n+1}\right] \tag{14}$$

where n is the dimensionality of the system and T_0 is inversely proportional to the density of states at the Fermi level.

In the last years many groups worked on the theory of transport in OS. In particular, Arkhipov's studies[32] showed that mobility is a function of temperature and charge carriers concentration. These dependences are calculated by averaging the hopping rate in an energetically and positionally disordered hopping system, and can be factorized as a product of two functions. The first function describes the temperature dependence and is slightly influenced by the concentration; the second one determines the concentration dependence of mobility and is temperature independent. Moreover, Arkhipov takes into account the influence of the deep trap presence on charge transport[33].

In addition to this, Viessenberg[34] carried out a theoretic study of field-effect mobility (Chapter 3) in a field-effect transistor, using a percolation model of hopping between delocalized states, hence obtaining an analytic expression for the mobility. The expression was tested with experimentally obtained results with a polymer, polythienylene vinylene, and with a small molecule, pentacene[35].

Recently, an analytic model describing general hopping transport in OS with traps was formulated on the basis of a percolation theory by Li[36]. The results show that the presence of different traps does not change the nature of the hopping transport but heavily affects the transport mechanism at low temperatures.

Finally, the presence of doping heavily influences mobility values as shown by Arkhipov[37,38].

Only a few theories for transport in organic semiconductors were mentioned here. Although there is a general agreement that transport occurs via hopping between localized states, the exact nature of these hops is still controversial. Moreover, polymer behaviour is different with respect to the small molecule one. Furthermore, mobility values change as a function of the kind of transport we are considering, e.g.: bulk or field-effect.

2.5 Small molecules and polymers

The π-conjugated organic semiconductors can be grouped into two main classes: small molecules and polymers. This distinction can be ascribed principally to their different molecular weight (MW) and chemical structure, as we will see in the next sub-sections.
The small molecules belong to the low MW class, whereas the polymers belong to the high MW class.

2.5.1 Small molecules

An organic small molecule is a molecule based on carbon which presents low MW, low spatial extent and consequently short conjugation length. Typically, interactions between different small molecules are dominated by Van Der Waals forces.
A plethora of organic species belong to this class: polycondensate aromatic hydrocarbons as pentacene (Figure 19.a) and perylene (Figure 19.b), organo-metallic complexes such as metal-phtalocyanines and oxy-quinoline (Figure 19.c), fullerens and dendrimers. However, the largest part of small molecules is represented by oligomers (from the Greek: ολιγος, or *oligos,* "a few", and μέρος, or *meros*, "part"). An oligomer consists of a finite number of monomer units (Section 2.5.2). Some examples of oligomers are: oligo-phenylenes or oligo-thiopenes (Figure 19.d).
Generally, molecular materials are processed by vacuum sublimation and solution-based processing techniques can rarely be employed. Films grown on dielectric substrates are mainly poly-crystalline, and their growth (and consequently the morphology of the film) can be partially controlled acting on the vacuum sublimation parameters and selecting the nature of the dielectric. Using small molecules, the analysis of the early growth stages of the active layer via atomic force microscopy (AFM) is also possible.
Concerning the transport properties, there is a large number of hole transport (*p-type*, e.g. α sexy-thiophene, named T6) and electron transport (*n-type*, e.g. perylene derivative, named PTCDI-$C_{13}H_{27}$) semiconductor small molecules. In the last years, ambipolar small molecules (e.g. DHCO4T, Section 5.5, Figure 19.e) have also been synthesized; these molecules are able to transport both electrons and holes.
To date, small molecules present the best carrier field-effect mobility values in OFETs based on rubrene (Figure 19.f) single crystals[39].

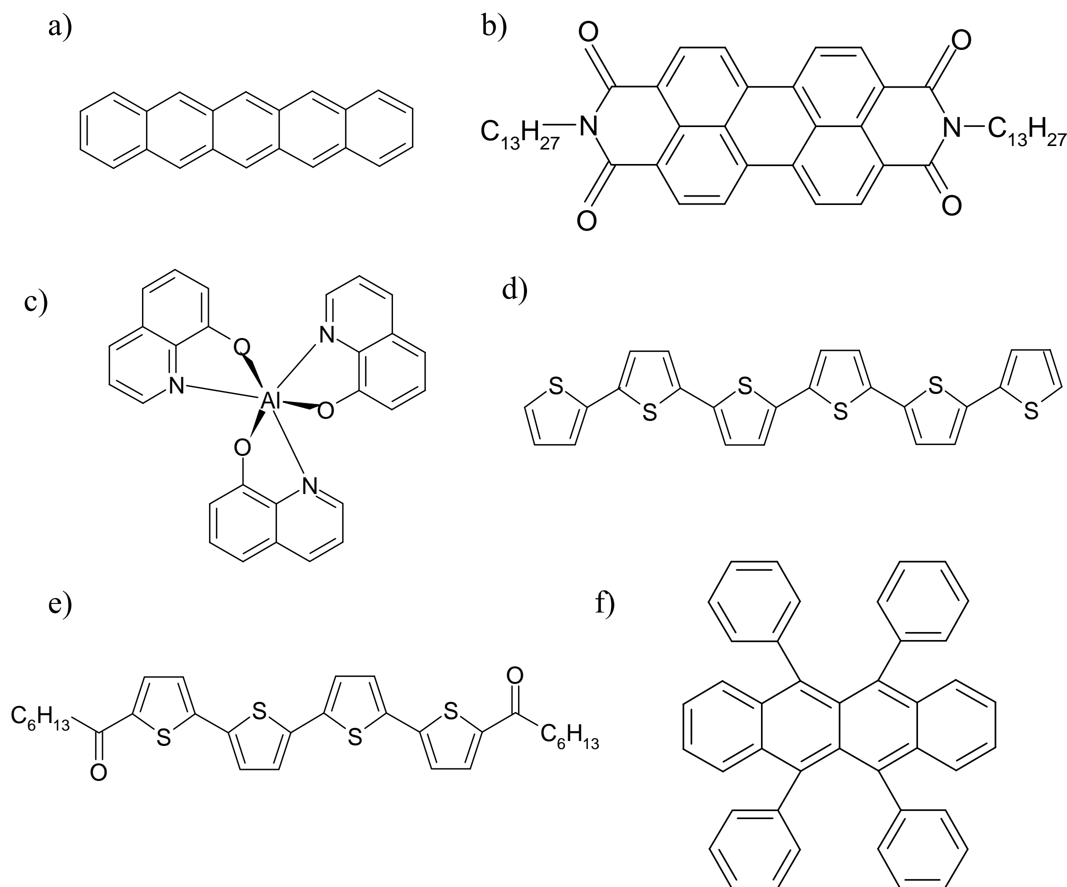

Figure 19: Chemical structure of some widely studied small molecule organic semiconductors. a) Pentacene; b) N,N - ditrydecylperylene - 3,4,9,10 - tetracarboxylic diimmide (PTCDI-$C_{13}H_{27}$); c) Allumin oxyquinolina (Alq_3); d) α sexy-thiophene (T6); e) α,ω-dihexylcarbonylquaterthiophene (DHCO4T); f) Rubrene.

2.5.2 Polymers

A polymer (from Greek: πολυ, *polu*, "many"; and μέρος, *meros*, "part") consists of the repetition of structural units, typically large mass molecules called *monomers* (from Greek *mono* "one" and *meros* "part") forming a long molecular chain along which π-electrons are delocalized. A chemical chain can take up a range of different conformations by rotating, twisting or distorting its backbone bonds. In addition, it may contain chain interruptions, chemical defects, pollutants, which contribute to break the conjugation. So the π-electrons delocalization becomes shorter and various. In amorphous polymers (the great majority), the case is further complicated as each conjugation section of the chain is randomly oriented with respect to the others. In this situation there is a range of conjugation lengths, with the obvious consequence that energy levels are spread out over a wider interval.

Polymers can be further catalogued: if they are formed by identical units, they are called homopolymers; if they contain more than one monomer, they are called copolymers[40].

The most studied OS polymers belong principally to three families: poly(phenylene-vinylene), e.g. MEH-PPV (Figure 20.a), or OC_1C_{10}-PPV; poly-thiopene, e.g. P3HT (Figure 20.c); and poly-fluorenes, e.g. F8T2 (Figure 20.d), or PFO.

Processability of polymers is usually restricted to wet techniques; this can be an advantage, because of the inherently low cost and large area coverage of such techniques, but also a disadvantage, as the structural and morphological control of usually amorphous thin films is limited. As a consequence, charge mobility in polymeric thin films is typically lower with respect to that of small molecule films.

Theoretically, there is no particular reason for the majority of polymers not to be ambipolar[41]; however they are found to be mainly p-type, and only a few are n-type (e.g. CN-PPV Figure 20.b). In the last years, it was demonstrated that the principal reason for many polymers not to be ambipolar is the interaction with the substrate over which they are grown[41,42].

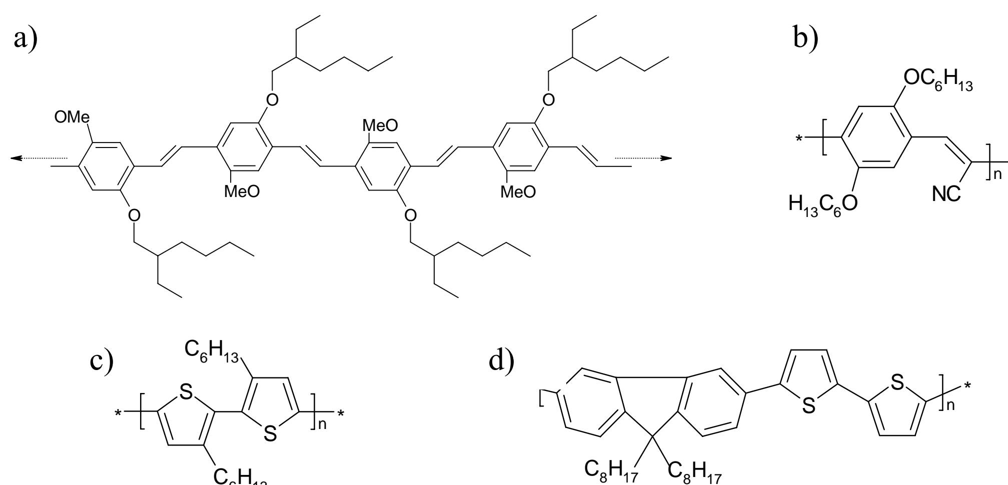

Figure 19: Chemical structure of some widely studied polymer organic semiconductors. a) Long chain of Poly[2-methoxy-5-(2-ethylhexyloxy)-1,4-phenylene-vinylene] (MEH-PPV); b) Poly[2,5,2',5'-tetrahexyloxy-7,8'-dicyano-di-*p*-phenylenevinylene] (CN-PPV); c) Poly[3-hexylthiophene] (P3HT); d) Poly[9,9'-dioctyl-fluorene-*co*-bithiophene] (F8T2).

References Chapter 2:

[1] A. Sacco, *Fondamenti di chimica*, Casa editrice Ambrosiana, 2ª Edizione, **1996.**

[2] A. Post Baracchi, A. Tagliabue, *Chimica per le scuole medie superiori*, Ed. Lattes, **1995.**

[3] I. H. Campbell and D. L. Smith, *Physics of Organic Electronic Devices*, in Solid State Physics **55,** Academic Press, 2001.

[4] D. P. Craig, S. H. Walmsley, *Excitons in Molecular Crystals*, Benjamin, New York, **1968**.

[5] P.W. Atkins, R.S. Friedman, *Molecular Quantum Mechanics*, Third Edition, Oxford University Press, **1997**.

[6] J.C. Scott, G.G. Malliaras, Chem. Phys. Lett., 299, 155, **1999**.

[7] N.W. Ashcroft, N.D. Mermin, *Solid State Physics*, Holt, Rinehart and Winston, New York, **1976**.

[8] S.M. Sze, *Physics of Semiconductor Devices*, Wiley, New York, **1981**.

[9] P.R. Emtage, J.J. O'Dwyer, *Phys. Rev. Lett.*, 16, 356, **1966**.

[10] M.A. Abkowitz, H.A. Mizes, *Appl. Phys. Lett.*, 66, 1288, **1995**.

[11] E.M. Conwell, M.W. Wu, *Appl. Phys. Lett.*, 70, 1867, **1997**.

[12] V.I. Arkhipov, E.V. Emelianova, Y.H. Tak, H. Bassler, *J. Appl. Phys.*, 84, 848, **1998**.

[13] J.C. Scott, G.G. Malliaras, Chem. Phys. Lett., 299, 155, **1999**.

[14] H. Ishii, K. Sugiyama, E. Ito, K. Seki, *Adv. Mater.*, 11, 605, **1999**.

[15] C. Kittel, *Introduction to Solid State Physics*, John Wiley & Sons Inc., New York, Chichester, Brisbane, Toronto, Singapore, Seventh Edition, **1996.**

[16] R. Farchioni, G. Grosso, *Organic Electronic Materials Conjugated Polymers and Low Molecular Weight Organic Solids*, Ed. Springer.

[17] M. Pope, C.E. Swenberg, *Electronic processes in organic crystals*, Oxford University Press, New York, **1982**.

[18] A.A. Maraudin, E.W. Montrol, G.H. Weiss, *Theory of Lattice Dynamics in the Harmonic Approximation*, 2nd edition, Solid state Physics Suppl. 3., Academic Press, New York.

[19] I.G. Austin, N.F. Mott, *Adv. Phys.*, 18, 41, **1969**.

[20] T. Holstein, *Ann. Phys.*, 8, 343, **1959**.

[21] T. Holstein, *Ann. Phys.*, 8, 325, **1959**.

[22] J. Yamashita, T. Kurosawa, *J. Phys. Chem. Sol.*, 5, 34, **1958**.

[23] I.G. Lang, Y.A. Firsov, *Sov. Phys. Sol. State*, 5, 2049, **1964**.

[24] I.G. Lang, Y.A. Firsov, *Sov. Phys. JETP*, 54, 826, **1968**.

[25] C.K. Chiang, C.R. Fincher Jr., Y.W. Park, A.J. Heeger, H. Shirakawa, E.J. Louis, S.C. Gau, A.G. MacDiarmid, *Phys. Rev. Lett.*, 51, 913, **1987**.

[26] J.H. Burroughes, D.D.C. Bradley, A.R. Brown, R.N. Marks, K. Mackay, R.H. Friend, P.L. Burns, A.B. Holmes, *Nature*, 347, 539, **1990**.

[27] H. Koezuka, A. Tsumara, T. Ando, *Synth. Met.*, 18, 699, **1987**.

[28] H. Hoegl, *J. Phys. Chem.*, 69, 755, **1965**.

[29] A.R. Brown, A. Pomp, C.M. Hart, D.M. de Leeuw, *Science*, 270, 972, **1995**.

[30] D.D.C. Bradley, A.R. Brown, P.L. Burn, R.H. Friend, A.B. Holmes, A. Kraft, *Solid State Science*, 107, Springer, Hiedelberg, 304, **1992**.

[31] N. F. Mott, E. A. Davies, *Electronic Processes in non-crystalline materials,* 2nd Edition, Oxford University Press, **1979**.

[32] V.I. Arkhipov, E.V. Emelianova, G.J. Adriaenssens, H. Bassler, *J. of Non-Cryst. Solids*, 299-302,1047, **2002**.

[33] V.I. Arkhipov, J. Reynaert, Y.D. Jin, P. Heremans, E.V. Emelianova, G.J. Adriaenssens, H. Bassler, *Synth. Met.*, 138, 209, **2003**.

[34] M.C.J.M. Vissenberg, M. Matters, *Phys. Rev. B*, 57, 12964, **1998**.

[35] A.R. Brown, D.M. De Leeuw, M. Matters, C.P. Jarrett, *Synth. Met.*, 88, 37, **1997**.

[36] L. Li, G. Meller, H. Kosina, *Solid-State Electr.*,51, 445, **2007**.

[37] V.I. Arkhipov, P. Heremans, E.V. Emelianova, H. Bassler, *Phys. Rev. B.*, 71, 045214, **2005**.

[38] V.I. Arkhipov, E.V. Emelianova, P. Heremans, H. Bassler, *Phys. Rev. B*, 72, 235202, **2005**.

[39] V. Podzorov, E. Menare, A. Borissov, V. Kiryukhin, J.A. Rogers, M.E. Gershenson, *Phys. Rev. Lett.*, 93, 086602, **2004**.

[40] J.R. Fried, *Polymer Science and Technology*, Prentice Hall Professional Technical Reference, **2003**.

[41] N. Karl, *Synth. Met.*, 133-134, 649, **2003**.

[42] J.C. Scott, G.G. Malliaras, Chem. Phys. Lett., 1999, 299, 155.

Chapter 3:

OFET device physics

This section reports an overview about OFETs devices, starting from the structures and introducing the working principles. Via a simple approch the equations that describe the OFETs behaviour are obtained. Besides, an analysis of the interfaces present in a OFET is performed: the issues of charge injection in real devices as well as the influence of the dielectric are studied.

3.1 OFET device structure

As briefly mentioned in Chapter 1, a field-effect transistor (FET) is a semiconductor device commonly used as an amplifier or as an electrically controlled switch. It is composed by a semiconducting material working as a *channel* in which current flows. At one extremity of the channel there is an electrode called *source* and at the opposite side there is a second electrode called *drain*. As we will see (Section 3.2), the physical dimension of the channel are fixed but the part actually used for the conduction can be varied by applying a voltage to a third electrode called *gate*. The FET conductivity depends on the portion of the channel open to the current. Little changes in the gate voltage can involve great changes in the current flowing from the source to the drain, thus amplifying the signal. If the channel is composed by an organic material, we have an *organic field-effect transistor* (OFET). The channel is in contact with a dielectric layer working as a capacitor, and allows current modulation through the gate voltage (Section 3.2).

The main constituting elements of an OFET are: three contacts (source, drain and gate), an active semiconducting material and a dielectric layer. These key elements can be differently combined to obtain different device structures. The most common among them are reported below: *bottom gate - bottom contact* (Figure 20.a), *bottom gate - top contact* (Figure 20.b) and *top gate - bottom contact* (Figure 20.c). In the bottom gate - bottom contact (BG-BC) the drain and the source electrodes are positioned directly on the dielectric film. The gate contact is under the dielectric; it usually works also as a substrate, and the active material is grown on

top of the dielectric. In this configuration, the contact resistance is usually higher with respect to the bottom gate - top contact (BG-TC) case and three interfaces are in contact in the same region: OS/contacts, contacts/dielectric and OS/dielectric. This can increase the difficult in the control of the organic growth in these “triple points”. Furthermore, treating the dielectric surface to improve the OFET performances for the BG-BC is difficult, if not impossible, because the electrodes presence prevents a perfect treatment at the edge with the dielectric. Otherwise, this kind of devices are easier to process (typically for the classic SiO_2 dielectric the drain and the source contacts are obtained by photolithography), as they involve less steps with respect to the BG-TC, and the possible damage of the active layer by growing the electrodes is ruled out.

In the BG-TC configuration, the drain and the source electrodes are grown on top of the OS. Below it, there is the dielectric and the gate contact working also as substrate. In this geometry (as in the top gate – bottom contact one), the injection zone (contacts/OS) is well separated from the conducting zone (OS/dielectric). Furthermore, treating the dielectric surface in intimate contact with the active layer, thus changing its chemical environment, is easy. Clearly, the disadvantage for this kind of devices is a tricky processing involving more steps with respect to the BG-BC.

In the top gate – bottom contact (TG-BC) device, the active layer is grown directly onto a substrate where the drain and the source contacts are already present. The dielectric is deposited on top of the OS, and the gate electrode is placed on top of it. This is a sort of mirror geometry with respect to the BG-BC.

In this thesis we used the BG-TC configuration.

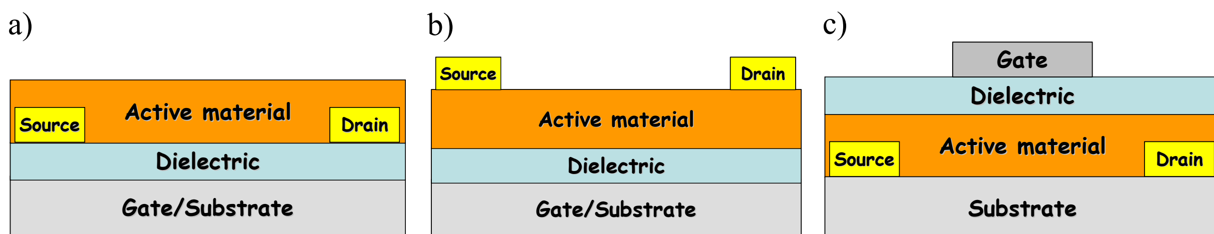

Figure 20: Typical OFET structures: a) *bottom gate - bottom contact*, drain and source are directly grown on the dielectric and the gate also functions as a substrate; b) *bottom gate - top contact*, drain and source are grown on the active material, and once again the gate works also as a substrate; c) *top gate - bottom contact*, the gate is on top of the structure: it is grown on the dielectric, in a sort of reverse geometry with respect to a).

3.1.1 Materials employed for OFET fabrication

The main components of an OFET are: an active material, contacts and a dielectric.

3.1.1.1 The active material

As already mentioned (Section 2.5) the majority of OS are p-type, but in the last years a number of n-type materials have been produced[1,2]. Typical OS feature relatively wide band gap: in the range of 2-3 eV. The synthesis of new n-type or ambipolar OS involve the presence of high electron affinity groups in the material, comprising specific electron withdrawing groups[1] (as -F, -CO, etc…).

It was recently clarified that not only does the chemical structure of the organic material determine its behaviour, but also processing conditions, the choice of electrodes and the dielectric species are relevant for the OFET operations. The material transport properties strongly depend to the interfaces present in the device in which it is used. Therefore, instead of p-type or n-type OFET, one should better refer to p-channel or n-channel transistors.

3.1.1.2 The electrodes

Transistors have three electrodes: drain, source and gate. Drain and source are also called *injecting electrodes,* while the gate is called *control electrode.*

The roles of these two electrode typologies are quite different. The gate is used to control the portion of the conduction channel open to current (Section 3.2), by applying an appropriate voltage. This electrode can be a metal or a conducting polymer, but in most cases highly doped silicon is used, as it works also as substrate. Devices made in this work are based on heavily doped silicon because of its wide commercial availability and its good performances.

The two other electrodes are responsible for the charge injection and collection, through the transistor channel. In n-channel transistors, this means injection of electrons into the LUMO level of the semiconductor, whereas in p-channel transistors it means injection of holes into the HOMO level of the active material. Differently from the classic inorganic amorphous silicon case, these contacts are very important for a good OFET operation[3-5]. If we work with non-ohmic contacts, a potential barrier is formed, and it leads to poor charge injection. This introduces an extra resistance to the transistor: the *contact resistance*. This is relevant when field-effect transistors perform in the linear regime (Section 3.2) because a large part of the source-drain voltage drops at the contacts and not across the channel.

Dipoles could be intentionally introduced at the interface through, for example, self assembled monolayers[6,7] to enhance the charge injection and the metal adhesion to the

organic material. The source and the drain electrodes are usually high work function metals (e.g gold, platinum, etc…) for p-channel OFETs and low work function metals (e.g. Calcium) for n-channel ones. However, conducting polymers (e.g. PEDOT:PSS, PANI, etc…) may be used as well.

3.1.1.3 The dielectric

Organic field effect transistors are truly interfacial devices; the region where the charge transport takes place at the OS/dielectric interface is few nanometers thick, hence the properties of the insulator are very important. Both the semiconductor and the insulator affect the performance of the device.

The interplay between dielectric and active material is complex and a clear interpretation is not yet available. The equation showing the crucial parameter for a dielectric material, the capacitance per unit area, C_i, can be expressed as:

$$C_i = \varepsilon_0 \left(\frac{k}{d} \right)$$

where k is the dielectric constant and d is the insulator thickness.

As mentioned, the dielectric influences carrier transport and mobility in different ways. First, the dielectric can affect the morphology of the active layer or the orientation of small molecules or of polymer segments. Transport properties are strongly linked to the molecule orientation, because hopping conduction is related to the length of the π-delocalization (Section 3.3.2). Second, the OS/dielectric interface roughness modulates the mobility of charge carriers. Commonly, the higher the roughness, the lower the device performances[8-10]. Finally, a crucial role for the conduction is played by the value of the dielectric constant. Since the current flowing in the semiconductor channel is proportional to C_i and to the voltage applied between drain and source (Section 3.2), it seems clear that a viable approach to increase the current while operating at low biases is to increase the capacitance of the dielectric. High k materials allow high C_i values with a thick film which prevents *leakage currents* (currents flowing from the OS to the gate contact). This idea was implemented using inorganic dielectric species. Starting from the classic silicon dioxide (low dielectric constant, usually about 3,9), different oxides were studied, like Al_2O_3 (ε around 7), Ta_2O_5 (ε around 24), etc… Different inorganic species were also used[11]: nitrides, titanates, etc…. Unfortunately, these materials present many trap sites at the surface and therefore, not surprisingly, their use as insulators in OFETs still leads to low transport properties. For example, the SiO_2 surface is rich in Si–OH defects that strongly influence the performances of

the device (Section 3.3.2.2). Moreover, when inorganic dielectrics are used OFETs lose two important characteristics: flexibility and low-cost processing. Inorganic dielectrics are usually grown by sputtering or chemical vapour deposition (CVD), and these techniques are more expensive than spin-coating or printing from solutions.

Anyhow, considering the diffuse commercial availability of silicon dioxide, and the possible integration of the organic (or hybrid) materials in inorganic transistors, many efforts were put in improving performances of SiO_2 based OFETs. In particular, good results were obtained treating the SiO_2 surface in order to remove or cover charge carrier traps. Surface treatments based on self assembled monolayer (SAM) of hexamethyldisilazene (HMDS) or octadecyltrichlorosilane (OTS) were first employed at Philips in the early 1990s[12]. Then several studies investigated the effects of SAM[13-16] or other silanes[16,17].

Over the last years, solution-processable materials, in particular polymers, have been widely used as dielectric in OFETs, partly because films with good characteristics can be obtained by spin-coating or printing, but also because they are flexible and allow good performance devices. Polymers having different chemical structures and physical properties are available. The films obtained have very smooth surfaces and a wide range of possible dielectric constants. Theoretically, higher k values should be preferred, but a recent[18] report shows that amorphous OS ensure better mobility and lower threshold voltages (Section 3.2) if low dielectric constant insulators are used, these involve a low polar interface between them and the OS (Section 3.3.2.3).

Obviously, using low-k insulators the required operating voltage may be higher.

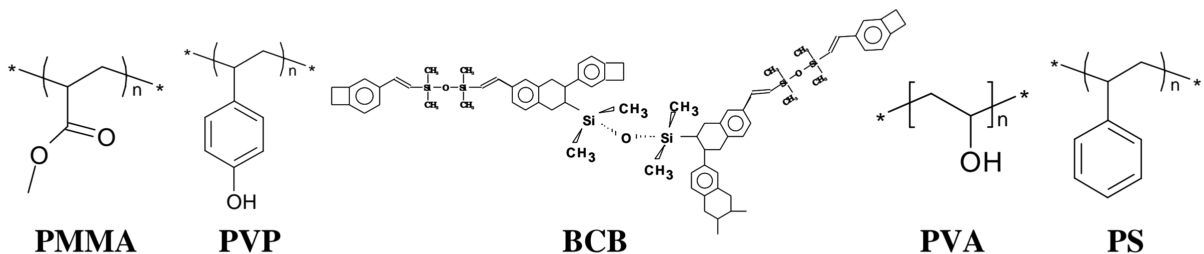

Figure 21: Chemical structure of the most widely used dielectric polymers in OFETs: PMMA (polymethylmethacrylate); PVP (polyvinylphenol); BCB (benzocyclobutene); PVA (polyvinylalcohol); PS (polystyrene).

Typical widely used[11] dielectrics polymer are reported in Figure 21.

Summarizing, the choice of the dielectric and the careful control of its characteristics in an OFET is crucial to optimize the most important device characteristics, such as: mobility, threshold voltage, current hysterisis (Section 3.2) and device to device reproducibility.

3.2 Working principles

To explain how a classic OFET works, a simple BG-TC geometry (Figure 22) is referred to. As briefly mentioned (Section 3.1.1), the physical dimension of the channel is fixed and it is described by the channel length (L) and the channel width (W). The real portion of the channel used for the conduction is determined by the voltages applied to the device. We refer to the voltage applied between drain and source as V_{ds}, while the voltage applied to the gate is labelled as V_g. By convention, the source is generally considered grounded and the voltage is applied to the drain contact. The current flowing through the channel is called I_{ds} and it is a strong function of V_g.

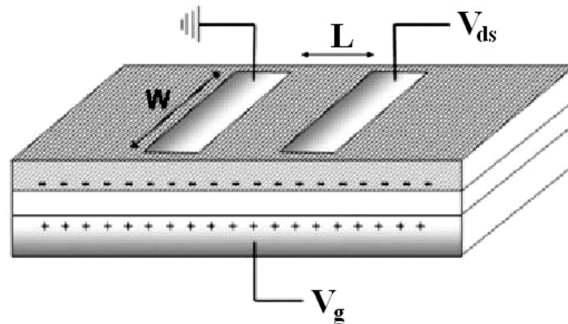

Figure 22: Classic BG-TC geometry with physical channel dimensions labelled:
W = channel width, L = channel length.

3.2.1 Origin of the field-effect

The dielectric is sandwiched between the gate and the OS, and they work like two plates of a plane capacitor. Thus, when a V_g is applied, charges of different sign are accumulated at gate/dielectric and dielectric/OS interfaces (like in a classic capacitor, in Figure 22 there is an example of positive gate voltage applied). Much of this charge in the active material is mobile and moves in response to the applied V_{ds}. When no V_g is applied there are ideally no free charge carriers, and the device is *off*. Otherwise, with applied V_g the device is *on*.

This gate-induced charge carrier creation is called *field-effect*, and it is the key-idea of the working principle of FETs[19].

To better understand the origin of this effect, we have to analyze a simplified energy level diagram (Figure 23). In the off state, the Fermi level of the drain and of the source contacts generally lies between the HOMO and the LUMO of the organic semiconductor (Figure 23.a). There are few charge carriers available for conduction (owing to the thermal energy

promotion from HOMO to LUMO). If a V_g is applied, then a large electric field (***E*** = **-grad** V) at the OS/dielectric interface is present. If $V_g > 0$ then ***E*** lowers HOMO and LUMO levels of the semiconductor while the Fermi level of the contacts remain fixed (Figure 23.b). If $V_g < 0$, the energy levels of the active material rise up (Figure 23.c). In the first case the V_g value can be so large that the LUMO and the Fermi level of the contacts have more or less the same energy; so electrons can flow from the source into the LUMO. Free electrons are present at OS/insulator interface. If $V_{ds} > 0$ is applied, electric current flows between source and drain (Figure 23.d). Similarly, in the second case, applying a $V_g < 0$ holes can be injected from the source into the HOMO, thus obtaining mobile charges which move in response to a $V_{ds} < 0$ (Figure 23.e).

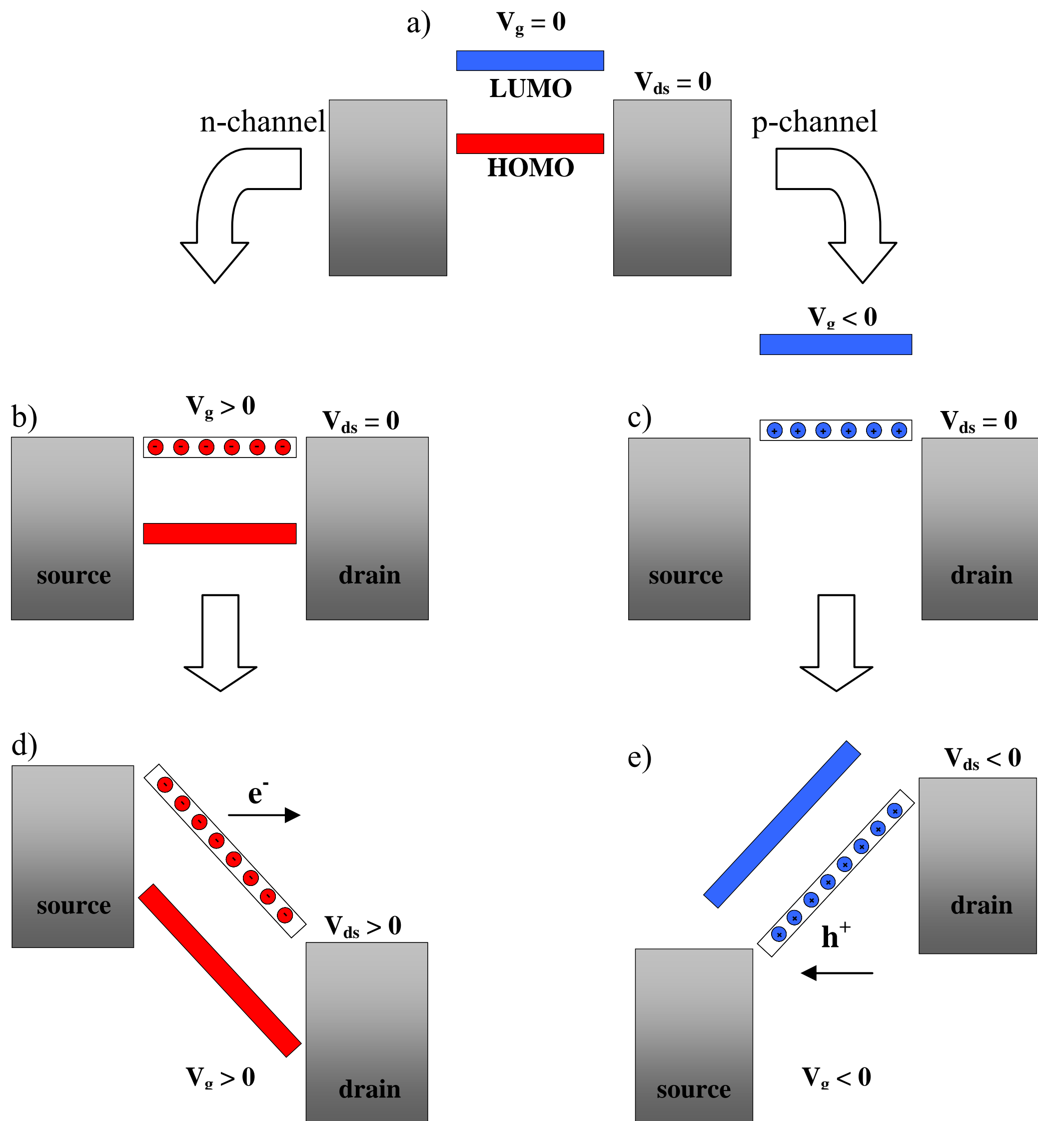

Figure 23: Schematic energy level diagram for an OFET when V_g and V_{ds} are applied. When only V_g is applied free charges carriers electrons (b) or holes (c) are generated in the LUMO or HOMO of the OS. When V_{ds} is also applied the Ids current flows due to electrons (d) or holes (e).

In this simple description, any OS can apparently show field-effect conduction and transport both holes and electrons, depending on the sign of V_g. This is not true: in fact, both the field-effect and the ambipolar behaviour strongly depend on the interfaces present in the devices and on the charge carrier traps and/or dopants presence. The previous description do not consider such factors which render the materials practically unipolar or unable to show field-effect conduction.

3.2.2 Charge density distribution in an OFET

An n-channel OFET can be used as an example to understand the basic operation regimes due to the distribution of “free” charges in the active material. If we assume ohmic contacts and no trap presence (*ideal case*), when a $V_g > 0$ is applied, as seen in the previous section, we have free electrons at OS/dielectric interface. Without any voltage difference between drain and source, this negative charge density is uniform along all the active material, we will then have a uniform *conduction channel*. If a positive V_{ds} is applied, the induced charge density (Coulomb/cm^2) in a certain position x of the semiconductor is described by:

$$q_{ind} = n(x)et = C_i[V_g - V(x)] \qquad (1)$$

where t is the thickness of the charged layer in the channel, n(x) is the density of charges in the channel (cm^{-3}), *e* is the electron charge and C_i is the insulator capacitance per unit area[20,21].

Clearly, charge density at x is proportional to the voltage difference between the active material and the gate exactly at point x.

However, real devices are far from being ideal and not all induced charges are mobile; a large number of deep charge traps are present in the film (deep enough to effectively immobilize electrons trapped in them). Deep traps have to be filled before the additionally induced charge can move. Thus, a minimum gate voltage has to be applied to obtain free electron density in the channel, the *threshold voltage*, V_t. Obviously, in n-channel OFETs V_t is higher than zero (for a p-channel OFETs the idea is the same, but charge carriers have opposite sign, so V_t is lower than zero). If we include the threshold voltage in equation (1):

$$q_{ind} = n(x)et = C_i[V_g - V_t - V(x)] \qquad (2)$$

As V_t is not ideally a function of x, with $V_{ds} = 0$ and $V_g > V_t$ we have a homogeneous charge density in the channel. When a small source-drain voltage is applied ($V_{ds} << V_g - V_t$) a *linear gradient* of charge density is formed. The voltage drop between OS and gate is larger at the source, where V(x) = 0 (grounded), than at the drain, where V(x) = V_{ds}. This is the *linear*

regime in which the current flowing through the channel is directly proportional to V_{ds} (Figure 24.a).

When the source-drain voltage is further increased, we reach a point where a potential difference between the gate and the part of the channel near the drain no longer exists, the channel is *pinched off*. This means that a charge carrier depletion region is formed next to the drain, because the difference between the local potential V(x) and V_g is lower than the threshold voltage.

A space-charged-limited saturation current can flow across this narrow depletion zone. Carriers are swept from the pinch point to the drain by a comparatively high electric field in the depletion region (Figure 24.b).

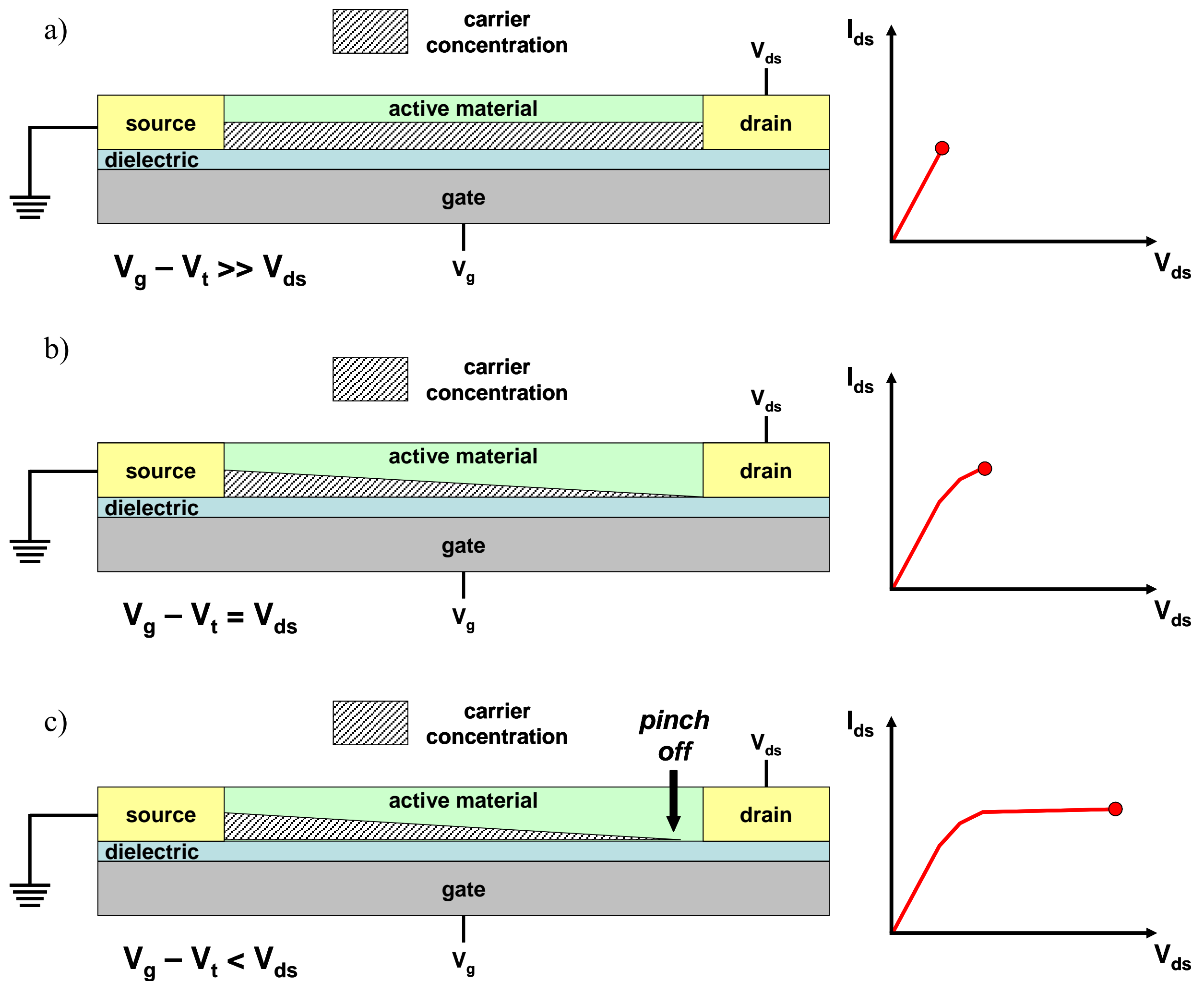

Figure 24: Schematic structure of an OFET. a) Carrier concentration profile in the linear regime; b) Carrier concentration profile when the pinch off occurs near the drain electrode ($V_g - V_t = V_d$); c) Carrier concentration profile in the saturation regime.

A further increase in V_{ds} pushes the pinch-off point further away from the drain (Figure 24.c). However the length of the channel (L) shortens only slightly, as it is infinitely larger than the width of the depletion region, and the integrated resistance of the channel from the source to the pinch point remains more or less the same. For these reasons once pinch off condition is met, current saturates at I_{ds}^{sat}. From a mathematical point of view, pinch off is reached when $V_{ds} = V_g - V_t$.

The current-voltage characteristics in the different operating regimes of an OFET can be described analytically, in a simplistic way, considering the channel as a resistor and starting from the Ohm laws:

$$I = \frac{V}{R} = V \frac{S}{\rho L} \tag{3}$$

where R is the resistance of the system, ρ the resistivity, L and S the resistor length and section.

Since conductivity (σ) is the inverse of resistivity and the resistor section is width times thickness of the channel, we have:

$$I = V\sigma \frac{W t}{L} \tag{4}$$

using the general definition of conductivity, $\sigma = \mu\, e\, \bar{n}_{ind}$, where e is the fundamental unit of charge, μ the carrier mobility and $\bar{n}_{ind}$ the average carrier concentration in the channel, we can write a similar equation for the drain-source current flowing in the OFET channel:

$$I_{ds} = \frac{W}{L}\left(\bar{n}_{ind}\, e t\right)\mu V_{ds} \tag{5}$$

Substituting equation (2), and taking into account that, in the linear regime, for a small value of V_{ds} the *average* value of V(x) is $V_{ds}/2$ (which is the drain-source voltage in the center of the channel) we obtain:

$$\begin{aligned} I_{ds} &= \frac{W}{L} C_i\, \mu \left[\left(V_g - V_t\right) - \frac{V_{ds}}{2}\right] V_{ds} \\ &= \frac{W}{L} C_i\, \mu \left[\left(V_g - V_t\right)V_{ds} - \frac{V_{ds}^2}{2}\right] \end{aligned} \tag{6}$$

that is the *linear equation* describing the dependence of I_{ds} from the drain-source and gate voltages. The classic I-V curves based on it and on the *saturation equation* (see below) are called *output curves* (Figure 25.a).

The same equation can be obtained with a more rigorous derivation. Starting from equation (2), the induced mobile charge is:

$$q_{ind} = n(x)et = C_i[V_g - V_t - V(x)] \tag{2}$$

the source-drain current induced by carriers is[20,21]:

$$I_{ds} = W \mu q_{ind} E_x \tag{7}$$

where E_x is the electric field at *x*. Substituting equation (2) in (7) and bearing in mind that E_x = dV/dx:

$$I_{ds}\, dx = W \mu C_i [V_g - V_t - V(x)] dV \tag{8}$$

The final equation for the drain-source current can be obtained by integrating eq. (8): from *x* = 0 to *x* = L (channel length) and from V(*x*) = 0 to V(*x*) = V_{ds}:

$$I_{ds} = \quad = \frac{W}{L} C_i \mu \left[(V_g - V_t) V_{ds} - \frac{1}{2} V_{ds}^2 \right] \tag{6}$$

When $V_{ds} << V_g$ (the linear regime), the equation is simplified to:

$$I_{ds} = \frac{W}{L} C_i \mu (V_g - V_t) V_{ds} \tag{9}$$

The field effect mobility in the linear regime (μ_{lin}) can be extracted from the gradient of I_{ds} versus V_g at constant V_{ds}:

$$\mu_{lin} = \frac{\partial I_{ds}}{\partial V_g} \frac{L}{W C_i V_{ds}} \tag{10}$$

The curves obtained keeping fix V_{ds} and sweeping V_g, are called *transfer curves* (Figure 25.b). Defining two derivatives (with V_g-$V_t >> V_{ds}$) is useful to calculate μ_{lin}:

$$\begin{aligned} g_m &= \left. \frac{\partial I_{ds}}{\partial V_g} \right|_{V_{ds}} = \frac{W}{L} C_i \mu_{lin} V_{ds} \\ g_d &= \left. \frac{\partial I_{ds}}{\partial V_{ds}} \right|_{V_g} \approx \frac{W}{L} C_i \mu_{lin} (V_g - V_t) \end{aligned} \tag{11}$$

Mobility can be calculated from the variation of g_m with V_{ds} or g_d with V_g:

$$\frac{dg_m}{dV_{ds}} = \frac{dg_d}{dV_g} = \frac{W}{L} C_i \mu_{lin} \tag{12}$$

as $\partial I_{ds} / \partial V_g$ is the angular coefficient (*m*) of the transfer curve, mobility is calculated from the linear interpolation of a transfer curve at high V_g (linear regime) where it is quasi-linear. Once mobility is obtained, the threshold voltage can be easily calculated from Eq. (9) (or from Eq (13), see below).

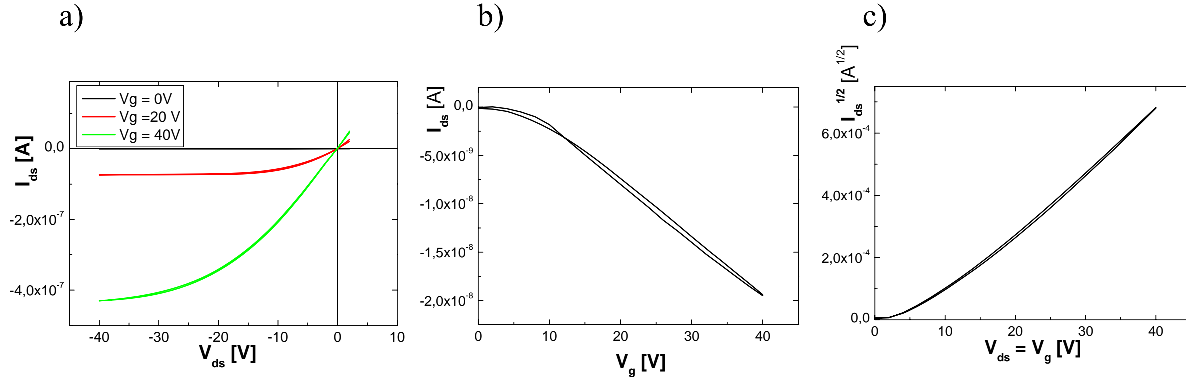

Figure 25: a) Output curve with different gate voltages applied to a p-type channel OFET; b) Transfer curve with V_{ds} kept fixed at -2 V, in a p-type channel OFET; c) Locus curve of a p-type channel OFET.

As already mentioned, the channel becomes pinched and the saturation region starts when $V_{ds} = V_g - V_t$. Current cannot substantially increase and reach a plateau in this region. The saturation drain-source current equation is obtained by substituting the saturation condition in equation (6):

$$I_{ds}^{sat} = \frac{W}{2L}\mu_{sat}\, C_i \left(V_g - V_t\right)^2 \tag{13}$$

The device mobility is also calculated in the saturation region from the slope of the linear part of an $\left(I_{ds}^{sat}\right)^{1/2}\ Vs\ V_g$ plot, called *locus curve*. A locus curve is a plot obtained by collecting I_{ds} current during the sweeping of the drain and gate voltages, which are kept at the same value, (Figure 25.c). In this condition, pinch-off is always reached near the drain contact. If $\left(I_{ds}^{sat}\right)^{1/2}$ versus V_g or V_{ds} is plotted, the linear interpolation of the data gives mobility and threshold voltage values. The square root of equation (13) is:

$$\sqrt{I_{ds}^{sat}} = \sqrt{\frac{W}{2L}\mu_{sat}\, C_i}\ \left(V_g - V_t\right) \tag{14}$$

it can be written as a straight line equation: $y = mx - mq$ where:

$$m = \sqrt{\frac{W}{2L}\mu_{sat}\, C_i} \tag{15}$$

and

$$q = -\frac{V_t}{m} \tag{16}$$

m is the angular coefficient of the straight line part of the locus curve (high $V_g = V_{ds}$) and *q* is the intercept with the *x* axis. Both values are obtained with a linear fit.

Mobility in the saturation region (μ_{sat}) and V_t can be easily calculated:

$$\mu_{sat} = \frac{2\ L\ m^2}{W\ C_i} \tag{17}$$

and
$$V_t = -\frac{q}{m} \tag{18}$$

Mobility values calculated in the linear and in the saturation regimes are often different, the saturation one being usually higher. This happens because the conduction channel resistance in saturation is higher than in the linear case, hence contact resistance is less critical than in the linear region. However, the two mobility values must be equal in devices with good injection contacts.

Another important parameter to analyze the OFET performances is the *ON/OFF ratio*. It is the ratio of the drain-source current flowing when the gate bias equals the drain one at the maximum voltage, to the one measured at the same drain potential but with the gate bias equal to zero[22]. This value should be as large as possible to obtain a clear switching behavior of the transistor. If the contact resistance can be neglected, the ON current mainly depends on the OS mobility and on the capacitance of the insulator used as dielectric. The OFF current is determined by the OS bulk conduction.

In good operating OFETs based on small molecules, ON/OFF ratio values should be around 10^4-10^5. If conjugated polymers are used, values are usually slightly lower, around 10^3-10^4. It obviously depends on the material and device characteristics.

Evaluating the current hysterisis is also important for an accurate electrical characterization. For a device behavior compatible with standard applications, this parameter should be minimized. In order to check hysterisis, the applied voltages are to be swept from 0 to a certain value, back and forward, collecting all the data. Hysterisis sometimes appears in the classic device curves (Figure 25.b). This means that, given the same bias conditions, the drain-source current is different if values are acquired during the forward step (increasing bias) or during the comeback. The drain-source current during the return is generally lower. This is due to the current transit inducing trap formation at the OS/dielectric interface. This is a problem, because trap generation is detrimental for the device lifetime and performance. Therefore, beyond optimizing mobility, voltage threshold and ON/OFF ratio values, minimizing the hysterisis is fundamental.

The last important check for a good performing device is to verifying the presence of a good saturation in the output curves, otherwise pinch off conditions are not fulfilled and the OFET looses part of its switching property.

3.3 Functional interfaces

In the past, the nature of charge carrier microscopic motion in organic devices was related exclusively to the quality and purity of the OS. In recent years, it has become clear that the electrical response is not determined by the chemical structure and the purity of the OS alone. The identification of the crucial role of the interfaces present in the device structure to increase performances was a key discovery that promoted the study of the interface characteristics.

In our thesis, we focused on BG-TC OFETs, in which the most important interfaces are: dielectric/OS and OS/metal.

The main part of our work aims at understanding the influence of the dielectric/OS interface on the electrical characteristics of both polymer and small molecule-based OFETs; moreover, we studied the influence of different OS/metal contact interfaces on the device characteristics.

3.3.1 Metal/OS interface

The description of an ideal metal/OS interface is reported in Section 2.3.1. As mentioned there, the presence of interfacial dipole has to be considered when describing a real system. The formation of a dipole in the metal/OS interface can be ascribed to many factors[23,24]: *interface charge transfer, formation of covalent bonds, pillow effect* and the *interfacial state formation.*

In the *interface charge transfer,* WF_m before the formation of the interface is different from the OS LUMO or HOMO. So if, e.g., the WF_m is smaller than the organic electron affinity (A), an electron transfer to the LUMO of the interface molecules is expected. The result is a dipole barrier ($\Delta > 0$) equal to an upward step of VL from the metal to the organic film. The energy raise of the electronic structure in the organic stops the electron flow and the partially occupied LUMO level relaxes into the gap forming interface gap states. Obviously, an opposite behaviour is expected if WF_m is bigger than the organic ionization energy (I). The value of Δ is determined by the magnitude of the dipole and $\Delta > 0$ if the positive pole of the dipole is in the metal direction, and vice versa. This dipole formation is expected in combinations of strong acceptor-low work function metal and strong donor-high work function metal. (Figure 26.a)

The second possibility corresponds to a reactive interface, in which chemical reactions occur. An example is the Magnesium (Mg)/tris(8-hydrox-quinoline)aluminium (Alq_3) case.

Experimental observations show a dipole barrier of about 0.5 eV due to the formation of a complex involving Mg and two Alq_3 molecules joined by Mg- C and Mg-O *covalent bonds* (Figure 26.b).

In the metal/OS interface, the first monolayer of the organic material does not create an abrupt interface like in the inorganic cases, rather an irregular shaped one. Recent studies suggest that a significant fraction of the interface dipole barrier corresponds to a lowering of the WF_m by the adsorbed molecules[25,26]. The first monolayer of the organic material on the metal interface can be imagined as adsorbed molecules on a metal surface. With large adsorbates, such as conjugated molecules, the repulsion between the molecule electrons and the metal surface electrons compresses the electron tail (Section 2.3.1), *pillow effect*, and lowers WF_m. In fact, WF_m is the sum of a bulk and a surface contribution and the latter sensitively depends on the tail of the electrons spilling out from the metal surface. This lowering practically increases the hole injection barrier.

The last factor is the possible existence of *interfacial states*. This means that there is a mechanism at the interface which works as a buffer for the charge exchange between the metal and the organic layer (Figure 26.c). This is common and well-known for inorganic semiconductors[27-29] but the origin of this mechanism in the OS/metal interface may be different and is not yet fully understood.

All these factors are valid for non polar molecules, but if we use *organic polar molecules* the orientation of the dipole moment can also lead to a large interfacial dipole (Figure 26.d).

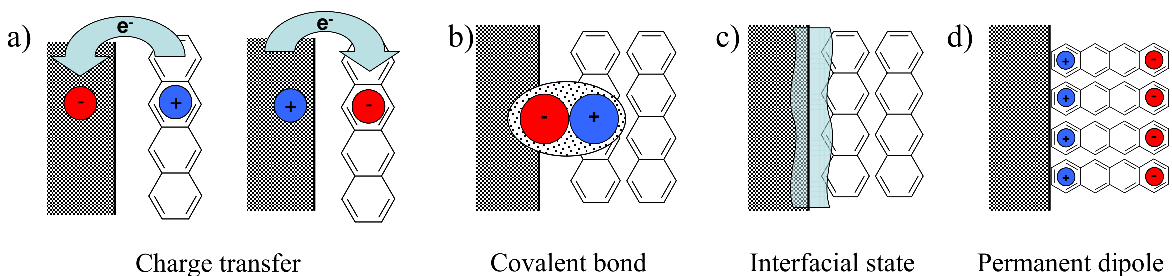

Figure 26: Interfacial dipole formation by a) charge transfer between strong donor-high work function metal (left) and strong acceptor-low work function metal (right); b) covalent bond formation; c) existence of interfacial states; d) molecule with a permanent dipole.

After describing the origins of the dipole present at the metal/OS interface, the next step is explaining the consequences of the dipole presence[23]. Thin organic films have an ideally low total number of mobile carriers in the organic. In such interfacial dipole formation, an abrupt shift of the potential across the dipole layer occurs, and this involves a shift of VL at the interface with respect to the non dipolar case (Section 2.3.1, Figure 27.a).

The behaviour is similar in thicker organic films, a case in which band bending has also to be considered (Figure 27.b).

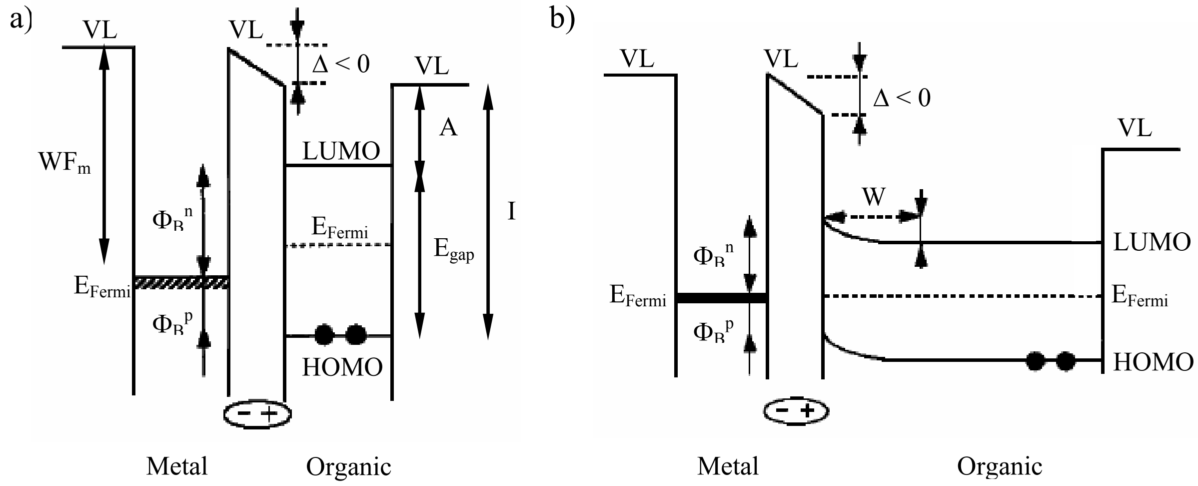

Figure 27: Interfacial energy level diagram with dipole presence (Δ < 0, positive pole of the dipole is in the organic direction) for a thin film (a) and a thick film (b).

Equations for hole and electron injection are similar to the ones described in Section 2.5.2, but with the dipole presence:

$$\Phi_B^p = I - WF_m - \Delta \tag{19}$$

and

$$\Phi_B^n = WF_m - A + \Delta = E_{gap} - \Phi_B^p \tag{20}$$

in these equations Δ is considered negative.

In spite of the large effort put in the investigation of contact effect[30-33], a lack of understanding about many problems, as the high contact resistance values and device irreproducibility still remains. OFETs are commonly described by the inorganic MOSFET model, and all the deviations are attributed to contact effects, sometimes generically termed *contact resistance*, although effects include more than the simple ohmic resistance.
We mention the recent work of *Hulea et al.*[34], who demonstrated better reproducibility with lower contact resistance in rubrene single crystal OFET when using nickel, instead of gold, as electrodes. Gold is usually employed because of its higher chemical stability to oxidation. In fact, nickel contacts present oxidation, but nickel oxide is nevertheless conductive and its work function value is similar to the gold one (about 5.0 eV). The reason why nickel performs

better than gold, which is a better conductor and has a comparable φ value, is less clear and needs further investigation.

The role of the OS/contact interface is crucial especially in small molecule-based OFETs, as contact resistance in polymer-based OFETs has been recently shown to scale linearly with carrier mobility[35].

Moreover, *Street and Salleo*[31] have demonstrated that the BG-TC geometry in OFETs is generally less susceptible to high contact resistance with respect to BG-BC one, because the effective area of the contact is larger. The main drawback of the BG-TC geometry is the possible damage of organic material during the metal deposition, as already mentioned.

In this thesis we work both with polymer (Section 5.4) and small molecule (Section 5.5) based OFETs in BG-TC geometry. As already mentioned, the exact role of the metal/OS interface in ambipolar small molecules remains uncertain. Therefore, transistors with different metals used as contacts were grown, and contact quality was then verified by atomic force microscopy measurements (Section 6.2.2), in order to evaluate the possibility of organic thin film damaging by metal cluster penetration.

3.3.2 Dielectric/OS interface

Field-effect conduction is well-known to occur in a narrow region of the active material, at the interface with the dielectric layes[36,37]. The crucial process of charge accumulation and transport (Section 3.2.2) takes place very close to the interface, between the gate dielectric and the semiconductor. Therefore, the interface and the dielectric properties have huge influence on the device characteristics.

Gate dielectrics to be used in FETs should show high dielectric break-down strength, be environmentally stable, easily processable and compatible with the preceding and subsequent processing steps. Beyond these obvious features, the choice of the dielectric species in OFETs involves many other effects which can highly influence the carrier transport and mobility with respect to inorganic materials. First, the dielectric can affect the *morphology* and/or the *molecular organization* of the OS thin film. Second, the interface with the organic material can be rich of *traps,* that are detrimental for charge transport. Finally, different dielectric species present different *dielectric constant* (ε) values that influence the OFET response.

3.3.2.1 Film morphology and molecular organization

The supra-molecular organization of organic semiconductors on the dielectric layer of thin film field-effect transistors is a crucial factor for achieving good device performance. Recently, several demonstrations in that sense have been carried out, both for polymer and for small molecules.

In particular, *Sirringhaus et al*.[14] showed how the field-effect mobility for a classic semiconducting polymer, the P3HT, is strongly dependent on the molecular organization. P3HT shows a self-organization in a lamellar structure with two-dimensional conjugated sheets formed by interchain stacking. Depending on processing conditions, the lamellae can adopt two different orientations, parallel and normal with respect to the SiO_2 substrate used as gate dielectric (Figure 28).

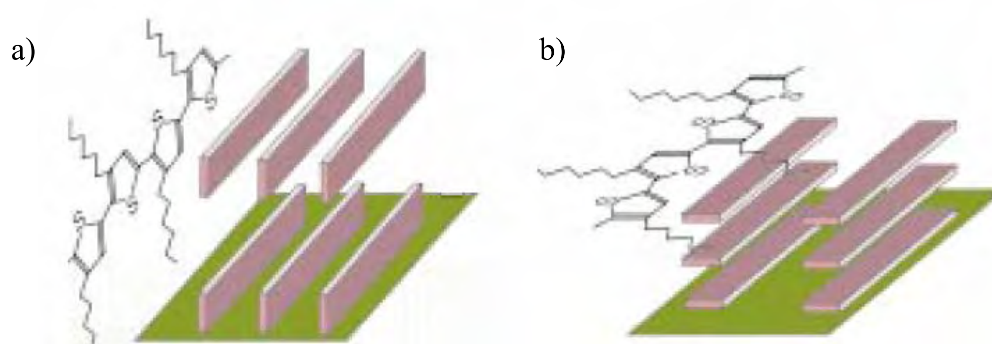

Figure 28: a) Lamellae organization perpendicular to the substrate; b) Lamellae organization parallel to the substrate. Image taken from[15]

The field-effect mobility of a device with a perpendicular lamellar structure (Figure 28.a) is 100 times higher than one where lamellae are parallel to the substrate (Figure 28.b). In a simple way, this behavior is due to high $\pi-\pi$ orbital overlapping in the perpendicular case, which favors charge carrier hopping from a polymer chain to another one.

This example clarifies how important the supra-molecular organization of the organic semiconductor on top of the dielectric species is.

Another interesting point to underline is that if the dielectric/OS interface or growth conditions are changed, different organizations can be driven in an organic material, thus obtaining the best structure for high mobility. *Cicoira et al*.[38] have recently demonstrated how two different SiO_2 dielectric treatments, and different deposition flux, provided different morphology and electrical response for an OFET based on tetracene small molecules.

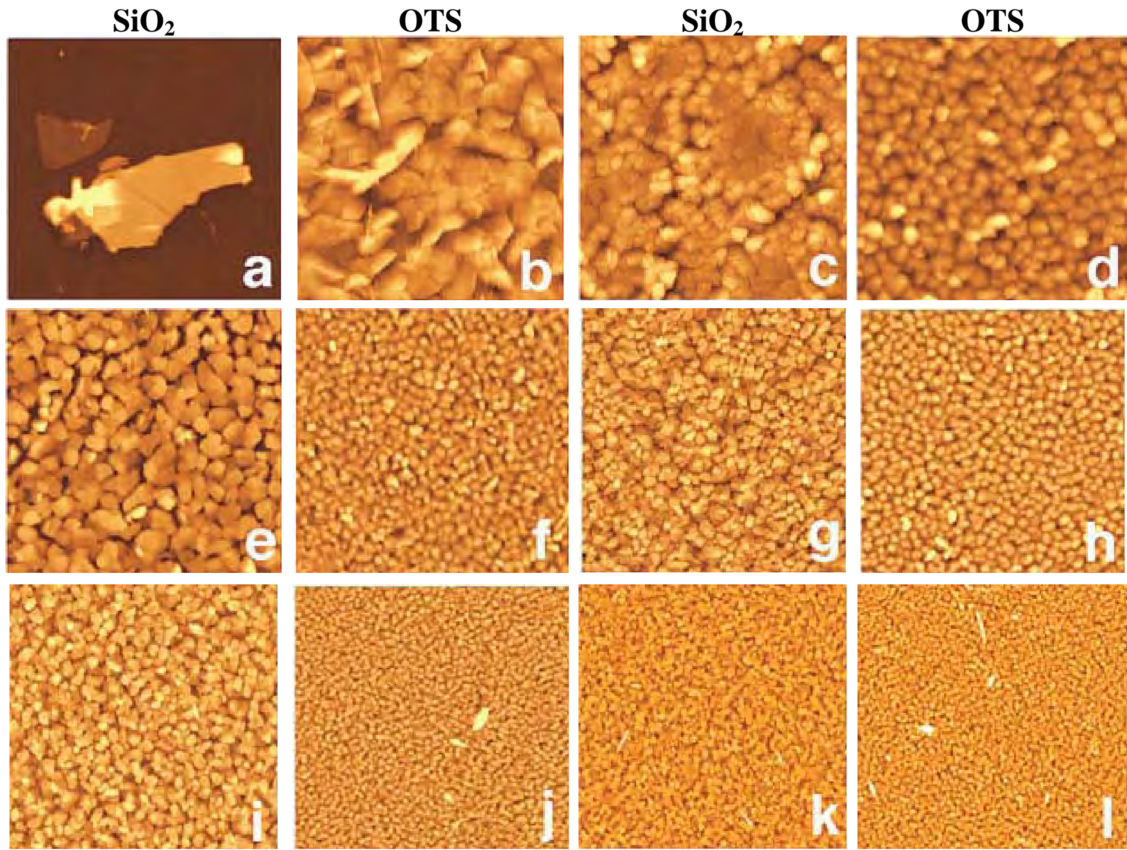

Figure 29: 10 x 10 atomic force microscopy images (Section 4.4) of 50 nm thick (nominal thickness) tetracene films grown on SiO_2 and SiO_2 chemically treated with OTS. The nominal deposition flux are: a,b) 0.02 Å/s; c,d) 0.1 Å/s; e,f) 0.5 Å/s; g,h) 2.0 Å/s; i,j) 5.0 Å/s; k,l) 10.0 Å/s.

In summary they observed that: on a given substrate, the grain size decreases with increasing deposition flux; at given deposition flux, the grain size is smaller on SiO_2 with OTS; the OTS favors the formation of grains with a more regular shape and size distribution.

The OTS treatment does not change the growth mode but strongly influences the island density and size; moreover it does not significantly improve the device performance (as recently observed for pentacene by *Shtein et al.*[39]). Instead, different deposition fluxes strongly influence the electrical characteristics. The average mobility increases with increasing deposition flux between 0.1 and 3 Å/s. A further increase of the deposition flux does not significantly affect the mobility (Figure 30).

Higher deposition flux involves smaller grain size and this increases the density of the grain boundaries (GB). GB are traps for the charge transport[40] and the mobility in such polycrystalline films is controlled by the rate of carrier jumps across the GB as[41]: $\mu = \mu_0 \exp\left(-\frac{\phi_b}{kT}\right)$ where ϕ_b is the height of the grain boundary potential barrier and described how GBs are deep traps. In this case the correlation between mobility and

deposition flux suggests that a more uniform substrate coverage (high flux) dominates over the density of GB in determining the field-effect mobility.

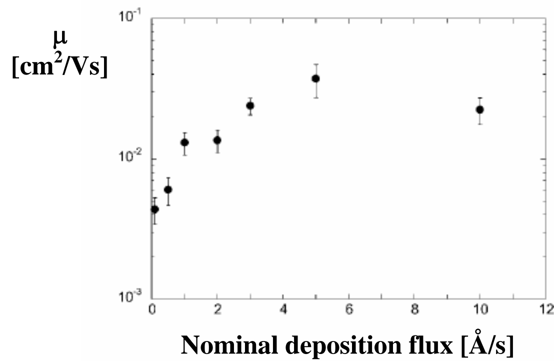

Figure 30: Field effect mobility of tetracene versus nominal deposition flux.

Indeed, analyzing the effect of the deposition flux on the early stages of growth they shown that higher deposition flux strongly improves film connectivity and substrate coverage (Figure 31).

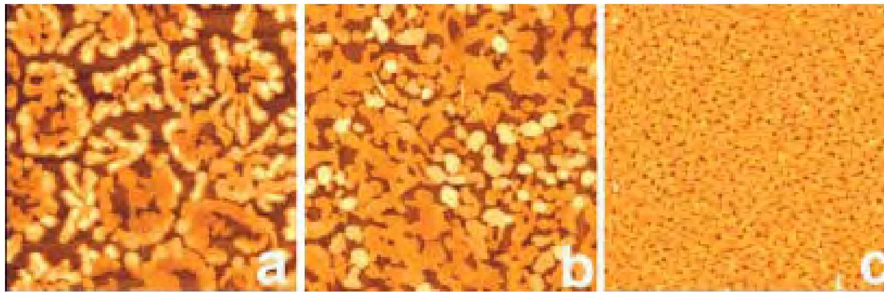

Figure 31: 5 x 5 atomic force microscopy images (Section 4.4) of 10 nm thick tetracene films grown on SiO_2 at nominal deposition fluxes of: a) 0.1Å/s; b) 0.5 Å/s; c) 5.0 Å/s.

Many papers[8,9,42-44] show how the morphology of the OS first layers is fundamental for transport properties and how it can be strongly influenced by the dielectric species. The basic idea for improving conduction properties through morphology or molecular organization control is to maximize the $\pi-\pi$ orbital overlapping, in order to make the carrier hopping[14] easier. In principle, this is possible by packing the organic molecules in a defined and ordered way. Furthermore, a homogeneous coverage of the substrate is required to achieve good mobility values, and so growth control is crucial again.

Unfortunately, the molecular organization cannot be controlled by the dielectric/OS interface in all organic system. If the intra-molecular interaction is much higher than the molecule-dielectric one, the organic material structure is expected to be independent on the substrate, and driven only by minimization of the system total energy.

3.3.2.2 *Interfacial traps*

Charge carrier traps at dielectric/OS interface may severely affect charge transport. From the energetic point of view, there could be shallow traps with little influence on electron and hole carriers, as the thermal activated de-trapping mechanism is allowed, or deep traps which pin charges, thus involving detrimental OFET performances.

The fundamental role played by these traps has been only recently discovered. At the moment, some experiment-based guidelines suggest that the trap presence lowers transport. However, there is an almost total lack of knowledge regarding the nature of traps and of the trapping mechanism.

The typical example for charge traps are the hydroxyl groups (Si-OH), normally present on the silicon dioxide surface. All organic semiconductors showing ambipolar transport according to time of flight measurements (TOF measure the bulk conduction properties of the organic semiconductors) are in fact unipolar in OFETs where SiO_2 is used as dielectric. In this case, only hole transport is usually allowed. The lack of electron transport can be attributed to the dielectric/OS interface and in particular to the interfacial traps presence. Electron trapping can be ascribed to the hydroxyl groups (Si-OH) normally present on the silicon dioxide surface. *Chua et al*.[45] demonstrated that the use of an appropriate hydroxyl-free gate dielectric (BCB, divinyl-tetramethylsiloxane-bis(benzocyclobutene) derivative) can yield n-channel field-effect conduction in conjugated polymers, which used to be experimentally only p-type. But the problem still remains, and the reason for the different behavior of BCB, compared to other hydroxyl-free dielectrics (e.g. PMMA, poly-methylmetacrylate) is not yet clear. The reason why –OH groups act as a trap for electrons is clear, but not the reason why they partially act as a trap for hole transport[42], too. To summarize, the trap mechanism that hinders the hopping of the charge carriers has not been well understood yet.

Obviously, there are also different kinds of superficial traps beyond –OH groups[11]. Therefore, a careful control of physical and chemical characteristics of the dielectric/OS interface is crucial to improve OFET performances .

The use of surface treatments or different polymeric insulator films reducing trap density has been investigated by different research groups[43]. This is true in the oligomers[44,46-48] case, and also when polymers or blends[10,49,50] are used as active materials. In SiO_2, most of these treatments involve a self assembled monolayer bonding directly the –OH groups and covering the rest of the trap rich dielectric surface (Section 5.2). Another possibility is replacing or covering the silicon dioxide film with different polymeric insulator films, which are theoretically trap-free (Section 5.3). The last possibility is the use of different inorganic

dielectric as high k-oxides species (e.g. Si_3N_4 or Al_2O_3). The driving force for the use of these high-*k* insulator is the possible low voltage operation (Section 3.1.1.3). The growth of these dielectric is generally more complicate and expensive than the SiO_2 treatments aforementioned (typically sputtering or chemical vapour deposition are request); moreover, often inorganic dielectric species lead to low mobility and high degree of variability from device to device, as a symptom of the trapped charges[11].

All these efforts are basically driven by experimental observation, and a solid theory explaining the trap action and nature is still missing.

3.3.2.3 Polarity of the dielectric

Not only can the insulator affect the morphology of the semiconducting layers or the trap density of the interface, but it can also change the density of states by local polarization effects.

We have already mentioned (Section 2.4) that transport takes place by hopping between localized states. These may be formed by individual molecules or by a number of interacting molecules. Localization in turn may be enhanced by local polarization effects that can distort these states. Random dipoles present at the interface with the OS can modulate the energies of localized states, leading to increased energetic disorder. *Veres at al.*[18] observed a marked improvement in field-effect mobility when the dielectric constant of the insulator was lowered from 18 to 2. They studied the temperature dependence of mobility, showing that transport in OFET grown on different dielectrics mainly differs by a temperature activation factor, which is the degree of energetic disorder expressed by the width of the density of states (DOS) in the Gaussian DOS representing the semiconductor. The energetic disorder is increased when more polar insulator is used. In absence of disorder, states would be totally isoenergetic. The dipoles present locally are randomly oriented and the intermolecular interactions among their energy fluctuations caused the broadening of the DOS. The more polar the interface, the more severe the DOS broadening, thus more tail states are present. Carriers in equilibrium with temperature and field (so with a certain energy) will, on average, face a higher potential barrier (higher of ΔE) for hopping into denser sites lying close, resulting therefore more localized (Figure 32). This is clearly detrimental for transport properties.

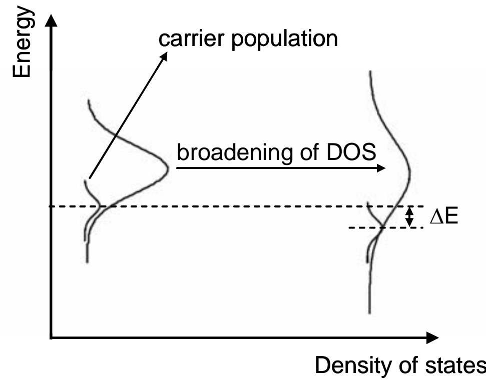

Figure 32: Scheme of the enhancement of carrier localization due to polar insulator interface.

On the same topic *Hulea et al.*[51] showed how, as polarity of dielectric species increases, transport at low temperature can not be described only by classic Holstain polaron movements (an Holstain polaron is a quasi-particles formed by a charge carrier bound to a short range deformation of the molecular crystal), but the formation of Frölich polarons has also to be considered (a Frölich polaron is a quasi-particles consisting of a charge carrier bound to a ionic polarization cloud in the surrounding medium). Through studies on the temperature dependence of mobility, they identified an intrinsic dependence of mobility on the dielectric properties, and they referred the lowering of the transport, as polarizability increased, to the interaction of charge carriers with their polar environment (Figure 33). In common inorganic semiconductors, the effective strength of this interaction is weak, due to low polarizabilities and large bandwidth; but in organic semiconductors bands are narrow and a high polarizability dielectric strengthens interactions.

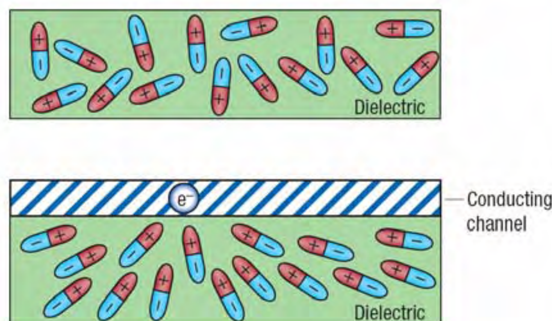

Figure 33: Illustration of the disorder dipoles present in a dielectric material (top). The charge carriers in the OFET conduction channel interact with dipoles in the dielectric affecting the charge motion (bottom). Images taken from[52].

References Chapter 3:

[1] J.A. Letizia, A. Facchetti, C.L. Stern, M.A. Ratner, T.J. Marks, *JACS*, 127, 13476, **2005**.

[2] R. Capelli, F. Dinelli, S. Toffanin, F. Todescato, M. Murgia, M. Muccini, A. Facchetti, T. J. Marks, *J. Phys. Chem. B.*, submitted;

[3] K. Nakayama, M. Umehara, M. Yokoyama, *Jpn. J. Appl. Phys.*, 45, 974, **2006**.

[4] R. Schroeder, L.A. Majewski, M. Grell, *Appl. Phys. Lett.*, 84, 1004, **2004**.

[5] K. Tsukagoshi, K. Shigeto, I. Yagi, Y. Aoyagi, *Appl. Phys. Lett.*, 89, 113507, **2006**.

[6] B. de Boer, A. Hadipour, M.M. Manadoc, T. Van Woudenbergh, P.W.M. Blom, *Adv. Mater.*, 17, 621, **2005**.

[7] B.H. Hamadani, D.A. Corley, J.W. Ciszek, J.M. Tour, D. Natelson, *Nano Lett.*, 6, 1303, **2006**.

[8] T. B. Singh, S. Gunes, N. Marjanovic, N. S. Sacriftci, R. Menon, *J. Appl. Phys.*, 97, 114508, **2005**.

[9] S. Shaked, S. Tal, Y. Roichman, A. Razin, S. Xiao, Y. Eichen, N. Tessler, *Adv. Mater.*, 15, 913, **2003**.

[10] H. Sirringhaus, *Adv. Mater.*, 17, 2411, **2005**.

[11] A. Facchetti, M.H. Yoon, T.J. Marks, *Adv. Mater.*, 17, 1705, **2005**.

[12] J. Veres, S. Ogier, G. Lloyd, D. de Leeuw, *Chem. Mater.*, 16, 4543, **2004**.

[13] H. Sirringhaus, N. Tessler, R.H. Friend, *Science*, 280, 1741, **1998**.

[14] H. Sirringhaus, P.J. Brown, R.H. Friend, M.M. Nielsen, K. Bechgaard, B.M.W. Langeveld-Voss, A.J.H. Spiering, R.A. Janssen, E.W. Meijer, P.T. Herwig, D.M. de Leeuw, *Nature*, 401, 685, **1999**.

[15] Y.Y. Lin, D.J. Gundlach, S. Nelson, T.N. Jackson, *IEEE Electron Device Lett.*, 18, 606, **1997**.

[16] M. Shtein, J. Mapel, J.B. Berziger, S.R. Forrest, *Appl. Phys. Lett.*, 81, 268, **2002**.

[17] A. Salleo, M.L. Chabinyc, M.S. Yang, R.A. Street, *Appl. Phys. Lett.*, 81, 4383, **2002**.

[18] J. Veres, S.D. Ogier, S.W. Leeming, D.C. Cupertino, S. Mohialdin Khaffaf, *Adv. Funct. Mater.*, 13, 199, **2003**.

[19] C.R. Newman, C.D. Frisbie, D.A. da Silva Filho, J.L. Bredas, P.C. Ewbank, K.R. Mann, *Chem. Mater.*, 16, 4436, **2004**.

[20] J. Zamuseil, H. Sirringhaus, *Chem. Rev.*, 107, 1296, **2007**.

[21] D.A. Neamen, Ed. *Semiconductor Physics and Devices : Basic Principles*, 2nd ed., Irwin: Chicago, **1996**.

[22] A.R. Brown, D.M. de Leeuw, E.E. Havinga, A. Pomp, *Synth. Met.*, 68, 65, **1994**.

[23] H. Ishii, K. Sugiyama, E. Ito, K. Seki, *Adv. Mater.*, 11, 605, **1999**.

[24] A. Kahn, N. Koch, W. Gao, *J. of Polymer Phys.*, 41, 2529, **2003**.

[25] X. Crispin, V. Geskin, A. Crispin, J. Cornil, R. Lazzaroni, W.R. Salaneck, J.L Bredas, *J. Am. Chem. Soc.*, 124, 8131, **2002**.

[26] P.S. Bagus, V. Staemmler, C. Woll, *Phys. Rev. Lett.*, 89, 096104, **2002**.

[27] L.J. Brillson, *Surf. Sci. Rep.*, 2, 123, **1982**.

[28] W. Monch, *Surf. Sci.*, 299/300, 928, **1994**.

[29] L.J. Brillson, *Surf. Sci.*, 299/300, 909, **1994**.

[30] L. Burgi, T.J. Richards, R.H. Friend, H. Sirringhaus, *J. Appl. Phys.*, 94, 6129, **2003**.

[31] R.A. Street, A. Salleo, *Appl. Phys. Lett.*, 81, 2887, **2002**.

[32] P.V. Necliudov, M.S. Shur, D.J. Gundlach, T.N. Jackson, *Solid-State Electron.*, 47, 259, **2003**.

[33] E.J. Meijer, G.H. Gelinck, E. Van Veenedaal, B.H. Huisman, D.M. de Leeuw, T. Klapwijk, *Appl. Phys. Lett.*, 82, 4576, **2003**.

[34] I.N. Hulea, S. Russo, A. Molinari, A.F. Morpurgo, *Appl. Phys. Lett.*, 88, 113512, **2006**.

[35] B.H. Hamadani, D. Natelson, *Appl. Phys. Lett.*, 84, 443, **2004.**

[36] G. Horowitz, X. Peng, D. Fichou, F. Garnier, *J. Appl. Phys*, 67, 528, **1990**.

[37] F. Dinelli, M. Murgia, P. Levy, M. Cavallini, D. de Leeuw, F. Biscarini, *Phys. Rev. Lett.*, 92, 6802, **2004**.

[38] F. Cicoira, C. Santato, F. Dinelli, M. Murgia, M.A. Loi, F. Biscarini, R. Zamboni, P. Heremans, M. Muccini, *Adv. Funct. Mater.*, 15, 375, **2005**.

[39] M. Shtein, J. Mapel, J.B. Berziger, S.R. Forrest, *Appl. Phys. Lett.*, 81, 268, **2002**.

[40] G. Horowitz, R. Hajlaoui, H. Bouchirha, R. Bourguiga, M. Hajlaoui, *Adv. Mater.*, 10, 923, **1998**.

[41] Orton, Powel, *Rep. Prog. Phys.*, 43, 1267, **1980**.

[42] F. Todescato , R. Capelli, F. Dinelli, M. Murgia, N. Camaioni, M. Yang, R. Bozio, M. Muccini, *Advanced Functional Materials*, submitted.

[43] T. Yasuda, K. Fujita, H. Nakashima, T. Tsutsui, *Jpn. J. Appl. Phys.*, 42, 6614, **2003**.

[44] M. Halik, H. Klauk, U. Zschieschang, G. Schmid, C. Dhem, M. Schutz, S. Malsch, F Effenberg, M. Brunnbauer, F. Stellaci, *Nature*, 431, 963, **2004**.

[45] L.L. Chua, J. Zamuseil, J.F. Chang, E.C.W. Ou, P.K.H. Ho, H. Sirringhaus, R.H. Friend, *Nature*, 434, 194, **2005**.

[46] S. H. Jin, J. S. Yu , A. L. Lee, J. W. Kim, B. G. Park, J. D. Lee, *J. Koeran Phys. Soc.*, 44, 181, **2004**.

[47] T. C. Gorjanc, I. Levesque, M. D'Iorio, *J. Vac. Sci. Technol.*, **,** 22, 760, **2004**.

[48] J. Puigdolers, C. Voz, A. Orpella, R. Quidant, I. Matrin, M. Vetter, R. Alcubilla, *Organic Electronics*, 5, 67, **2004**.

[49] A. Babel, S.A. Jenekhe, *J. Am. Chem. Soc.*, 125, 13656, **2003**.

[50] S. Goffri, C. Muller, N. Stingelin-Stutzmann, D. W. Breiby, C. P. Radano, J. W. Andreasen, R. Thompson, R. A. J. Janssen, M. M. Nielsen, P. Smith, H. Sirringhaus, *Nature Materials,* 5, 950, **2006**.

[51] I.N. Hulea, S. Fratini, H. Xie, C.L. Mulder, N.N. Iossad, G. Rastelli, S. Ciuchi, A.F. Morpurgo, *Nat. Mater.*, 5, 982, **2006**.

[52] V. Coropceanu, J.L Brédas, *Nat, Mater.*, 5, 929, **2006**.

Chapter 4: Experimental

This section describes the experimental setups used in this thesis. Thin film growth techniques, such as vacuum sublimation and spin-coating, are briefly described, with reference to the instrumentation employed. The setups used to perform contact angle and morphological measurements are presented. Finally, the glove-box, the parametric analyzer and the probe station used for electrical characterization of OFETs are described.

4.1 Film growth

The growth of thin films is a fundamental step in the fabrication process of all kind of organic devices. All the main OFET components (the active layer, the dielectric layer, the source and drain contacts) can be thin films.
There are a number of techniques for growing thin films, but two techniques are mainly used in the contest of organic electronics: *vacuum sublimation* and *spin coating*. In this section we illustrate these processing techniques, which were used for our OFET febrication.

4.1.1 Vacuum sublimation

Vacuum sublimation has experienced an enormous diffusion in the last decades as a technique to prepare thin films for small molecule organic semiconductor[1]. The main advantages of this technique consist of providing sub-monolayer thickness control during the growth, while the ultraclean environment provided by vacuum ensures a low level of contamination due to moisture or chemical impurities. Moreover, the presence of many control parameters give the possibility to drive a preferential growth modality. The vacuum sublimation is a powerful technique for thin film growth.
The main drawbacks of this technique are: high instrumental costs (turbomolecular pump, high vacuum chambers, etc…), impossibility to process polymers and high molecular weight materials, low industrial applicability and operational complexity.

The core of every vacuum sublimation setup consists of a vacuum chamber with a crucible and a substrate held perpendicularly to the crucible orifice. Once the crucible is filled with material, it is heated until its sublimation temperature is reached. The material exits the crucible orifice as a molecular beam and impinges onto the substrate. Then, according to the substrate temperature, molecules can be adsorbed, desorbed or diffuse to a nucleation center. Substrate temperature is a key parameter to modulate the growth of films with different morphology. A quartz microbalance placed near the substrate is used to monitor the amount of material sublimed yielding, after a calibration procedure which takes into account the material density, the nominal thickness and the evaporation rate are calculated. Evaporation rate and substrate temperature play a major role in the control of film morphology. The former depends on the crucible temperature while the latter can be controlled with a resistance attached to the substrate holder.

Our films were grown in two different chambers. The first one is a steel chamber equipped with four Knudsen cells for evaporation and is connected to a glove-box (Figure 34). This configuration permits a sequential growth of the active material and of the top metal contacts with immediate electrical characterization of the devices without any air exposure.

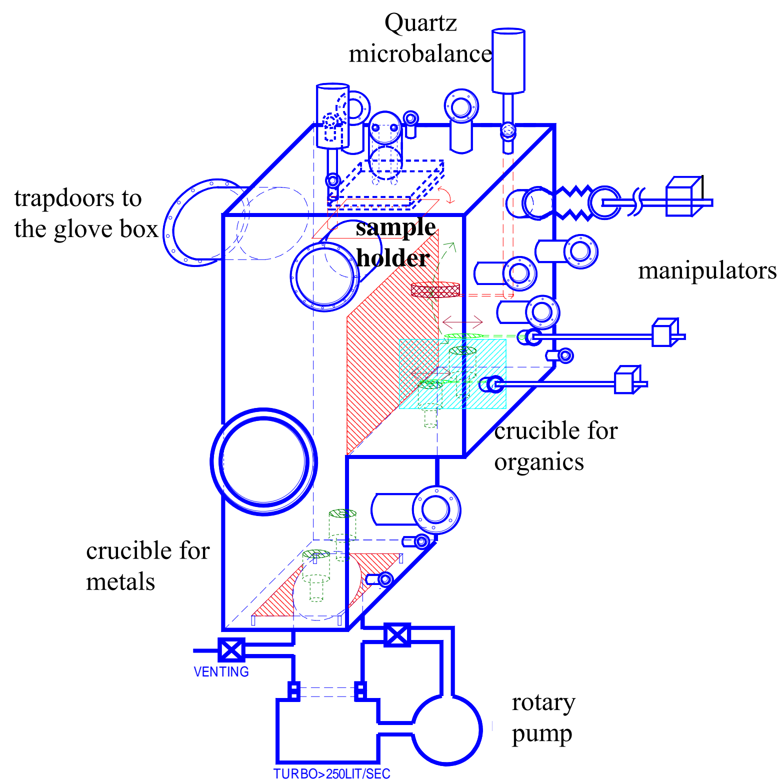

Figure 34: Scheme of the steel chamber linked to the box

Alternatively, if materials are air stable, a second chamber can be used. This is a glass bell chamber equipped with six different cells, for growing different materials (Figure 35).

In every case, cells are maintained few degrees under sublimation temperature before and after the film growth, in order to constantly outgas the source material from impurities. This procedure is accomplished while the substrate is kept mechanically shuttered.

Both chambers are equipped with a rotary and a turbomolecular pump which ensure a preliminary vacuum of about 10^{-7} mbar.

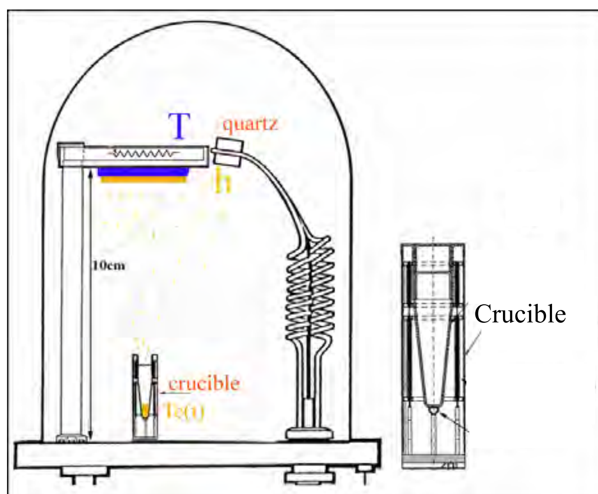

Figure 35: Vacuum sublimation glass bell chamber with quartz microbalance, crucible and cell scheme.

4.1.2 Spin coating

Spin coating is a procedure used to apply uniform thin films to flat substrates. In practice, an excess amount of a solution is placed on the substrate, which is then rotated at high speed. Centripetal acceleration will cause the fluid to spread to, or eventually off, the edge of the substrate leaving a thin film (Figure 36). This technique is very useful for polymers whose solubility is high in many solvents.

Physics behind the spin coating technique involve a balance between controlled centrifugal forces and viscous forces which are determined by solution viscosity. The main process parameters are: solution viscosity, angular speed (ω), angular acceleration, spin time and solution volume.

Solution viscosity is determined by the concentration of the organic material in the volatile solvent and gives the solvent drying rate. Generally, very dilute solutions afford thin films while viscous solutions give rise to thick films[2].

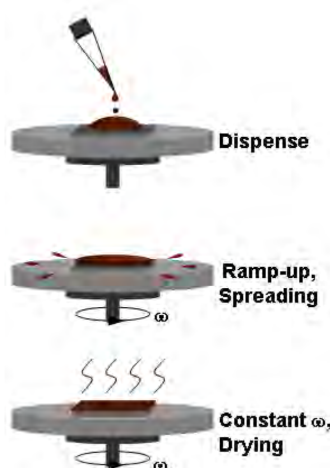

Figure 36: The principal spin coating steps: solution dispense, acceleration ramp and drying during the spin. Image taken from[3].

The spin speed of the substrate (rpm) affects the degree of centrifugal force applied to the solution. Film thickness is largely a balance between the force applied to shear the solution towards the edge of the substrate and the drying rate. As the solution dries, viscosity increases until the radial force of the spin process can no longer appreciably move the solution over the surface. Film thickness does not decrease significantly when spin time increases. Generally, the higher the speed, the thinner the film.

The acceleration of the substrate towards the final spin speed can also affect the coated film properties. Since the solution begins to dry during the first part of the spin cycle, it is important to accurately control acceleration. In some processes, 50% of the solvent in the solution evaporates in the first few seconds of the spin. The spin time must to be sufficient to permit a complete drying of the solution.

We employed a home made spin coater with a speed range between 500 and 7000 rpm. Acceleration was fixed and the sample was locked on the rotating plate by a vacuum system. The solution was dispensed manually with a micropipette, and always at the center of the substrate.

4.2 Contact angle measurements

The contact angle (θ_c) is a quantitative measure of the wettability of a solid by a liquid. It is defined geometrically as the angle formed by a liquid at the three phase boundary where liquid, gas and solid intersect (Figure 37). Low values of contact angle indicate that the liquid spreads (Figure 38.a), or wets well, while high values indicate poor wetting (Figure 38.b). If the contact angle is less than 90°, then the liquid is said to wet the solid. If it is greater than

90°, it is said to be non-wetting. An ideal hydrophilic liquid on an ideal hydrophilic surface would exhibit a contact angle of 0°, and accordingly an angle of 180° would be expected for an ideal hydrophobic substrate.

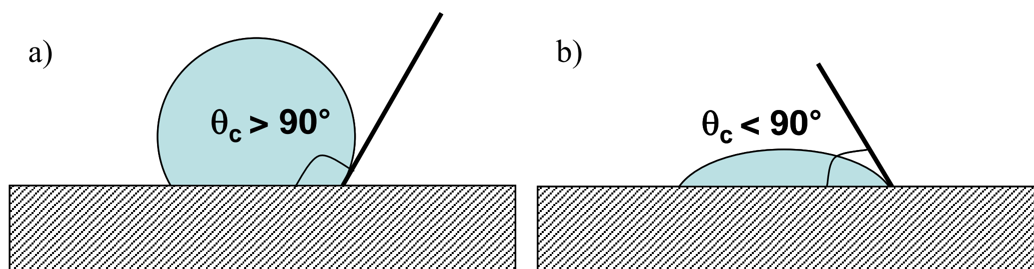

Figure 37: Schematic examples of: (a) low wettability, $\theta_c > 90°$; (b) high wettability, $\theta_c < 90°$

The most common approach used to measure contact angles is *Goniometry*. This method is based on the analysis of the shape of a drop of test liquid placed on a solid. The basic components of a goniometry system include a light source, a sample stage, lens and a camera. A liquid drop is put on the substrate lying on the stage with a syringe or a micro-pipette. A zoom of the contact zone is made through the lenses and the camera. Contact angle can be directly assessed, measuring by software the angle formed between the solid and the tangent to the drop surface.
The wettability of the samples used in this thesis was measured with a commercial contact angle instrument: Digidrop GBX, Contact angle meter model DS.

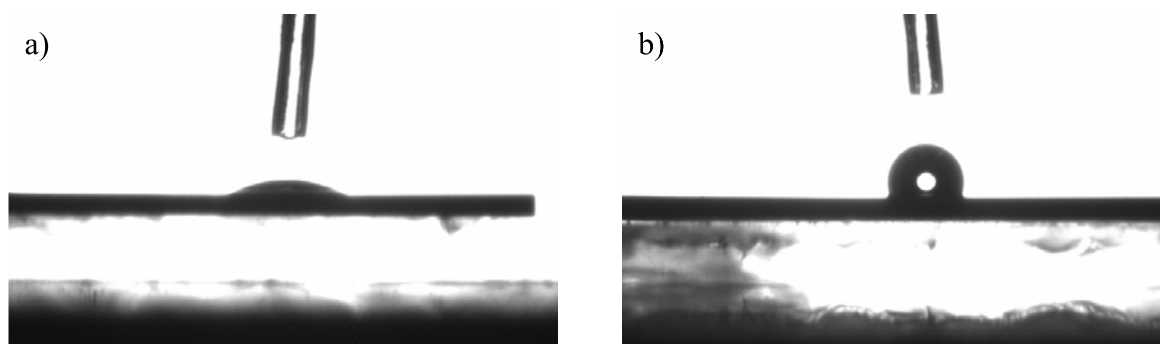

Figure 38: a) Low contact angle value, the liquid wets well the substrate; b) High contact angle value, poor wetting.

4.3 Thickness profiling

An *Alpha-step 200* surface profiler was used to perform thickness measurements on polymer films. A straight line was scratched into the polymer film using a sharp scalpel and the surface was scanned perpendicularly to the scratch. The range of scanning is selected so

that the scratch is midway between the start and the end of the scan. A cross-section of the profile was displayed, and the depth of the polymer thickness (that is the thickness of the scratch) can be computed. In order to evaluate the homogeneity of our spin coating and to have a reliable value of the thickness, each film was measured in several points of the samples and on different scratches. For each sample, the final thickness value is the average of all measures.

4.4 Atomic Force Microscopy (AFM)

Atomic force microscopy (AFM) belongs to the family of the Scanning Probe Microscopy (SPM) techniques. SPM are based on 3-D scanning of a sample surface, through a probe which locally interacts with the surface. The probe is placed near the surface (d < 100 nm). An electronic system measures the surface-probe interaction at every (x,y) point in the sample. The probe is moved on top of the sample by a piezoelectric actuator, in order to cover a path called *raster*. The interaction strength (whatever it is, depending on the SPM techniques) depends on the sample-probe distance. By mapping the strength in the (x,y) points, we could obtain an *image* of the sample surface.

AFM was invented by G. Binning, C. Gerber and C. Quate[4]. It overcomes the limits of other SPM (like Scanning Tunneling Microscopy, STM) because it permits the analysis of all type of samples (insulator, semiconductor, etc…). Furthermore, it allows processing in air, vacuum or liquid environment. The main components of an AFM are (Figure 39):

- a probe which can interact with the surface (Figure 40). The probe plays a key-role in the SPM techniques because it differentiates various techniques, in order to render the analysis sensible to different forces (magnetic, electric, etc…);
- a piezoelectric transducer (also called *scanner*, Figure 39) which permits probe or sample movements. Movements are possible in all the three spatial directions and with an accuracy in the order of 10^{-12} m (pm). Vertical movements are guided by a feedback system which keeps the surface-probe interaction fixed. These movements are recorded and used to determine the height of the surface;
- an electronic system used to measure and to amplify the probe-surface interaction;
- a mechanical system, to damp the external vibrations;
- the above mentioned feedback system, to keep the signal with the physical information at a set value (*setpoint*);
- a control system for the acquisition and visualization of the data.

In the AMF technique, the probe is a very sharp pyramidal or conical tip fabricated on the edge of a lever called *cantilever*. When the tip and the surface interact, a force modifies the cantilever's mechanical balance. These change is detected by a laser beam focused on the back of the cantilever (Figure 39). The laser beam, after a convenient optical path, reaches a sensor (*beam and bounce*). During the surface scanning, the sensor (usually a photo-diode) reveals the different laser beam positions that, after a suitable amplification, are used to reproduce the surface topography.

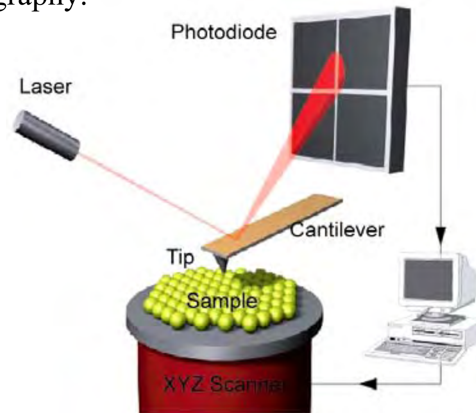

Figure 39: Scheme of the working system of the beam and bounce. The scanner move the sample so changing the tip/surface interaction and the optical path of the laser beam.

The probes

The probe is the fundamental part of the instrument. Ideally, it is conceived to be sensitive to a single chemical-physical interaction with the surface. But in practice this in not possible, so fabrication is important to minimize parasite interactions.

There are rectangular or triangular shape levers with conic or pyramidal tip. Classic conic tips have these features: length = 100-130 μm, wide = 35 μm, thickness = 2 μm, tip radius of curvature = 10 nm, elastic constant ≤ 10 N/m.

The fundamental characteristic is the radius of curvature of the tip, because it sets the minimal spatial resolution of the AFM.

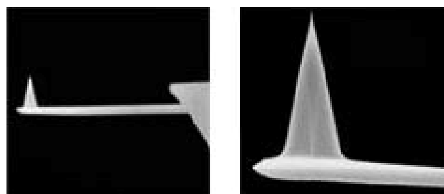

Figure 40: SEM images of a SiN cantilever with a conic Si tip.

4.4.1 AFM operating modalities

AFM instruments typically operate in two ways: *contact mode* (short range forces) and *non contact mode* (long range forces) (Figure 41).

In the contact modality, the tip touches the surface and a repulsive force bends the cantilever. The bending of the cantilever depends on the surface topography and is measured by the beam and bounce system. There are two operation modalities for contact mode: *constant force*, the feedback system drives the piezoelectric to keep the cantilever bending fixed; *constant height,* the tip height is kept constant and the different force strengths between tip and surface are collected.

In *non contact mode* the cantilever oscillate at its own resonance frequency, on a piezoelectric substrate. The interaction with the surface modifies the resonance frequency of the cantilever and physical information about the surface are obtained from these variations. This mode operation is less detrimental for the sample but has a worse lateral resolution.

A third operation mode has been developed, between the contact and non contact modes: the *semi-contact* or *tapping-mode* (Figure 41).

Like in non contact mode, the cantilever oscillates at its resonance frequency. The tip moves in a field of attraction and repulsion forces. The tip touches the surface in a intermittent way. Away from the surface the lever makes free oscillations, while when there is an interaction with the surface the oscillations amplitude is reduced to a set value (set-point). In this case the piezoelectric actuator moves the cantilever in order to keep the oscillations amplitude fixed, reflecting the differences in the surface morphology. The surface morphology can be reproduced through the actuator movements. The advantages of this procedure are low sample damaging and good lateral resolution. The semi-contact mode is usually employed for soft and biological materials.

Figure 41: Scheme of the AFM working modalities. In contact mode the topography is obtained by the cantilever bending; in non contact mode and semi-contact (or tapping) mode the signal comes from the variation of frequency, magnitude and phase of the cantilever oscillation.

4.4.2 The AFM instrument and the measures in this thesis

The AFM employed for this work is an *NT-MDT Solver Scanning Probe Microscope*. The operation condition are always the same: in air and in tapping mode. The operational scheme of the instrument is the classic scanning by sample in which the sample moves and the cantilever oscillates in a fixed position. The external vibration isolation is ensured by three springs that decouples the instrument from the environment.

We used this instrument for the dielectric surface roughness analysis, to study the early stages of organic film growth, to study different typologies of organic material growth on different substrates and to study the drain and source electrode morphology.

4.5 Device fabrication

All devices employed in this thesis are TG-TC OFETs, and they are fabricated following the same procedure. First of all, the substrate, formed by heavily doped silicon and covered with a thin silicon dioxide film, is cleaned (Section 5.1). Then, if necessary, SiO_2 is treated to modify the species in contact with the OS (Section 5.2).

The third step is different for polymer and small molecule based OFET. In the former case, the polymer solution is spun on the substrate (treated or not) to obtain a 100 nm thick film. After the OS deposition, the sample is annealed in vacuum or in controlled atmosphere to remove the residual solvent. In the small molecule cases, the substrate was masked to sublime the OS in device areas only. Each mask presents three apertures designed to achieve OFETs with different channel length.

The sample which encompass the OS are moved from the spin-coater (or form the sublimation chamber) directly into the glove-box, without any air exposure. Here, it is masked to grow the metal drain and source electrodes. The contact mask presents three couples of drain and source contacts with different separation in order to have three devices with different channel length (L = 150, 300 and 600 μm) on the same substrate. Masked samples are directly re-introduced from the glove-box into the vacuum chamber in which the metallic contacts are grown.

In the last step, the finished device is moved again in the glove-box and the electrical measurements are performed.

For the polymer based OFET, a further step is needed before the electrical measurements. In this case, differently to the small molecule one, the OS is present among the three devices

grown on the same substrate. Therefore, each device is not isolated and current can flow from one device to the neighbour one, thus lowering the performance. To avoid this, a manual scratch is performed with a scalpel around each device.

4.6 Electrical and optoelectronic measurements

Three types of measurement are mainly performed to test OFETs: the I-V or *output* curves, which is obtained keeping V_g fixed and sweeping the V_{ds}; the *transfer* curves, which are obtained keeping V_{ds} fixed and sweeping V_g; the *locus* curves, which are plots obtained by collecting I_{ds} current during the V_{ds} and V_g sweeping, which are kept at the same value.

4.6.1 Glove-box

A glove box is a sealed container designed to allow one to manipulate objects while being in a different atmosphere with respect to the object one, that is usually a very high purity inert atmosphere (such as argon or nitrogen). This is useful for working with oxygen sensitive substances. Inert atmosphere glove boxes are typically kept at a higher pressure than the surrounding environment, so any microscopic leaks are mostly leaking inert gas out of the box instead of letting air in. Built into the sides of the glove box are gloves, arranged in such a way that one can place his hands into them and be able to perform tasks inside the box without breaking the seal or allowing potential injury to the worker. Part or all of the boxes are usually transparent to allow one to see what is being manipulated. This instrument is important because most organic materials are oxygen and moisture sensitive; measurements performed inside the glove-box are intrinsic, as the environment does not influence them.

Our instrument is an EC-MECABOX from MECALAB labortechnologie AG. This glove box is composed of two containers coupled together by the main access entry chamber (Figure 42). Each container also presents a small entry chamber to introduce small objects. The left module contains the spin coater and is used for “wet chemical” processing. The right module contains the probe station for the electrical measurements (Section 4.5.2) and is linked to a growth chamber. This permits electrical characterization immediately after the device growth, without any air and oxygen exposure. Our glove box ensures oxygen and water presence below 1 ppm.

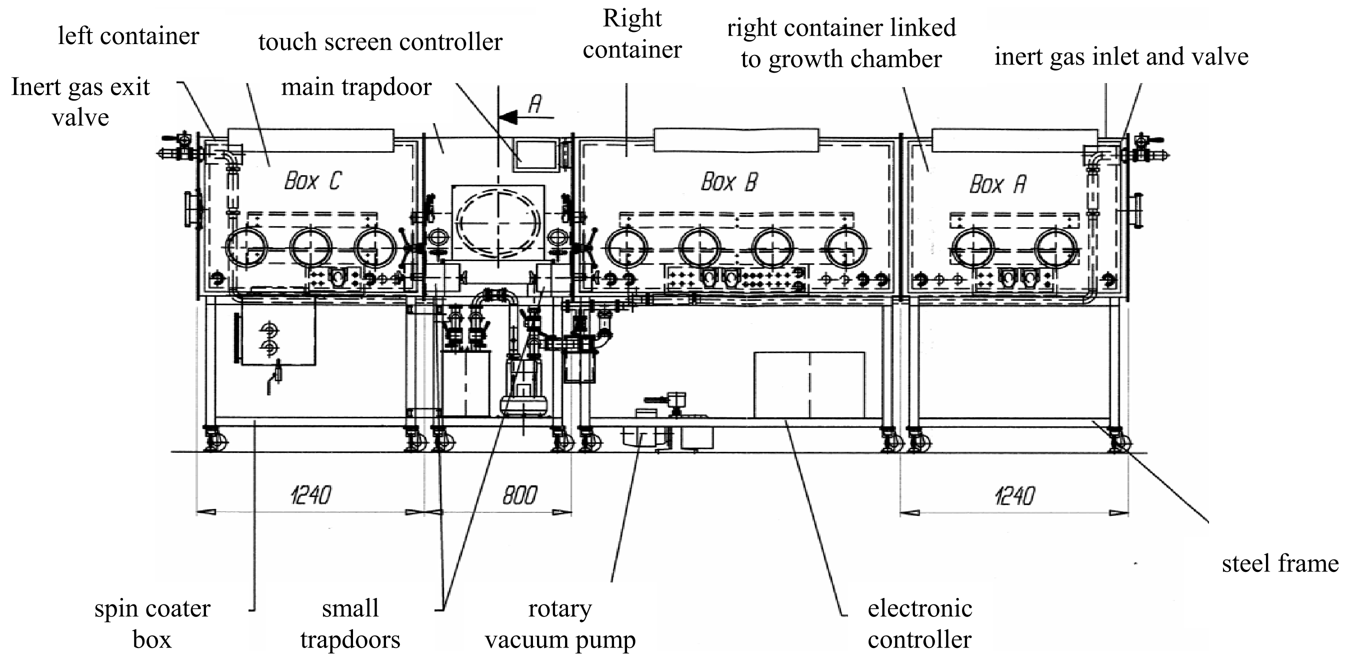

Figure 42: Scheme of the EC-MECABOX composition.

4.6.2 Electrical measurements

The core of the setup used to carry out the electrical measurements are the parametric analyzer and the probe station. The former supplies the set voltage to the device contacts in order to obtain the current flowing. Furthermore, it allows to collect the intensity of the current flowing through the OFET channel. All operations are software-controlled. We used Agilent B1500A parametric analyzer.

The parametric analyzer is linked to a home made probe station for electrical measurements and to a photodiode for electroluminescence measurements. These are placed inside the glove-box in order to measure devices without any oxygen or moisture exposure, which induces the lowering of electrical characteristics.

The probe station is composed of a fixed conductive support used to hold samples and to apply a voltage to the gate contact. Two conductive tips installed on a mobile cantilever and controlled by three micrometer for x,y z movements. These tips are used to apply the drain-source voltage and to detect the drain-source current. A webcam was used to help place tips on top of the drain and source contacts.

References Chapter 4:

[1] S. R. Forrest, *Chem. Rev.*, 97, 1793, **1997**.

[2] http://www.cise.columbia.edu/clean/process/spintheory.pdf

[3] http://ssg.epfl.ch/images/SpinCoating.png

[4] G. Binning, C.F. Quate, C. Gerber, *Phys. Rev. Lett.*, 56, 930, **1986**.

Chapter 5: Dielectric/Semiconductor Interface

This section first reports the main characteristics of the materials used as dielectrics in OFETs. We discuss about silicon dioxide and the various processes to clean it, about gas phase treatments of the silicon dioxide surface and about insulator polymers used as buffer layer on it. Then we study the dielectric/OS interface in OFETs. The cases of a dielectric in intimate contact with two PPV derivatives (Section 5.4) and with two molecular systems, α,ω-dihexylcarbonylquaterthiophene (DHCO-4T, Section 5.5) and ter(9,9-diarilfluorene) (T3, Section 5.6), are analyzed.

5.1 Silicon dioxide dielectric

In the last decades, silicon has been the most important substrate for technological applications. In particular, field-effect transistor technology relies on the growth of ultrapure silicon dioxide films at the interface with highly doped conducting silicon, in order to fabricate the gate in direct contact with the dielectric. The most common method used for the fabrication of SiO_2 is thermal oxidation. The process yields high performance silicon dioxide with electrical and mechanical properties such as high break-down voltage, no pin holes, uniform thickness and density[1]. Silicon dioxide is also very versatile, since its surface chemistry can be tailored with a variety of processes.

From a physical point of view, SiO_2 is an amorphous material in which each Si atom binds with four oxygen atoms in a tetrahedral geometry. The surface is characterised by the presence of two different kinds of bonds, silanols (Si-OH) and siloxanes (Si-O-Si) (Figure 43). High silanol density makes the surface hydrophilic.

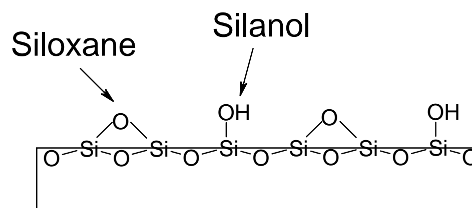

Figure 43: Schematics of the silicon dioxide surface with the presence of silanol and siloxane groups.

Silicon is spontaneously oxidised by the combined effect of H_2O and O_2. The mechanism of oxidation described in literature[2] shows that H_2O reacts more readily than O_2 with the silicon surface. Water promotes the formation of Si-OH bonds and renders the surface hydrophilic; afterwards, O_2 starts to react increasing the oxide thickness. The film formed is called *native oxide* and is usually about 1 nm thick. Typical contact angle values for this oxide are around 30°. To produce technologically high quality silicon dioxide for devices, thermal oxidation around 1100°C is used. Temperature makes silanoles to react as soon as they are formed on the surface. This *thermal oxide* presents a contact angle of about 65-70°.

In our OFETs, substrates consisted of heavily doped n^{++} silicon, that works also as gate contact, with a layer of thermally grown silicon dioxide (SiO_2). The thickness of the thermal oxide was 240 nm (with capacitance per unit area of: $C_{ox} = 1.8 \times 10^{-8}$ Fcm^{-1}). A typical value for the contact angle is $\theta_c = 67° \pm 2°$.

Before growing the organic active material on top of the silicon dioxide surface, this has to be cleaned. There are many possible cleaning processes aimed at removing surface contaminants and increasing hydrophobicity. Three different protocols were used in this thesis: *wet cleaning*, *plasma cleaning* and *HF etching.*

5.1.1 Wet cleaning

Wet cleaning is the mildest process, as it does not alter the surface but only removes impurities attached to it. It involves a sequential sonication in different solvents: 10 minutes in deionised water, 10 minutes in acetone, 10 minutes in chloroform, 10 minutes in acetone and finally, 10 minutes in deionised water again. The first water sonication is mainly used to remove SiO_2 residual dust due to batch cuts. Solvent sonication (from the less polar one to the more polar one and backward) removes organic impurities present on the silicon dioxide surface. The last sonication is in water, in order to avoid the presence of organic species remaining after the organic solvent evaporation. Samples were dried using argon gas after each sonication. The organic material is grown immediately after the cleaning process.

5.1.2 Plasma cleaning

In this case substrates before the plasma exposure underwent 10 minutes water and 10 minutes acetone sonications in order to remove the main surface impurities. Then they are cleaned with an oxygen plasma for 15 minutes at 100 W power. With this protocol, we expected to increase the amount of silanol (Si-OH) groups with a decrease of the Si-O-Si groups. We also found a little increase in the RMS roughness values of the film.

The organic material is grown immediately after the plasma process.

5.1.3 HF etching

HF etching is made by dipping substrates in a 2% water solution for a few minutes and then rinsing them in deionised water. This removes about 5 nm of the SiO_2 layer in order to leave more Si-O-Si or Si-H groups[3] on the surface with respect to the pristine SiO_2 one. Unfortunately, groups formed in this way are instable and convert to Si-OH bonds[4] with consequent re-growth of the native oxide.

5.2 Gas phase treatments of SiO_2 surface

As mentioned before, SiO_2 surface is rich in siloxane and silanol groups. The former are chemically stable, while the latter present the typical reactivity of alcohols and can be used to graft organic molecules. In our work, two kinds of molecules were grafted on the silicon dioxide surface: 1,1,1-octadecyltrichlorosilane (referred to as OTS) and 1,1,1,3,3,3-hexamethyldisiloxane (referred to as HMDS). These treatments attempt to overcome the trap charge nature of –OH groups and of other pollutants present on the silicon dioxide surface.

5.2.1 1,1,1-octadecyltrichlorosilane (OTS) treatment

The reaction of silicon dioxide with OTS yields a self assembled monolayer (SAM) terminated with methyl groups and is widely used to make the silicon dioxide surface hydrophobic. The first reaction step is the hydrolysis of trichlorosilane to trihydroxysilane. After that, the molecule is able to adsorb to the surface, thus creating a network of hydrogen bonds with the silanol groups and with itself. The final step is the condensation of hydroxyl groups and the creation of a covalent system. The entire reaction mechanism is reported in Figure 44.

The key parameter for the process is the amount of water. If it is in excess, hydrolysis is fast and hydroxysilanes start to polymerise before the adsorption step. On the contrary, if water is totally absent trichlorosilane cannot hydrolize. OTS forms SAM onto silicon substrates because its linear chain can pack into a compact film. The chain stands normal to the surface, binding to it through its silicon atoms and interacting intermolecularly with strong lateral interactions. The height of a standing OTS molecule in a SAM is around 2.5 nm[5].

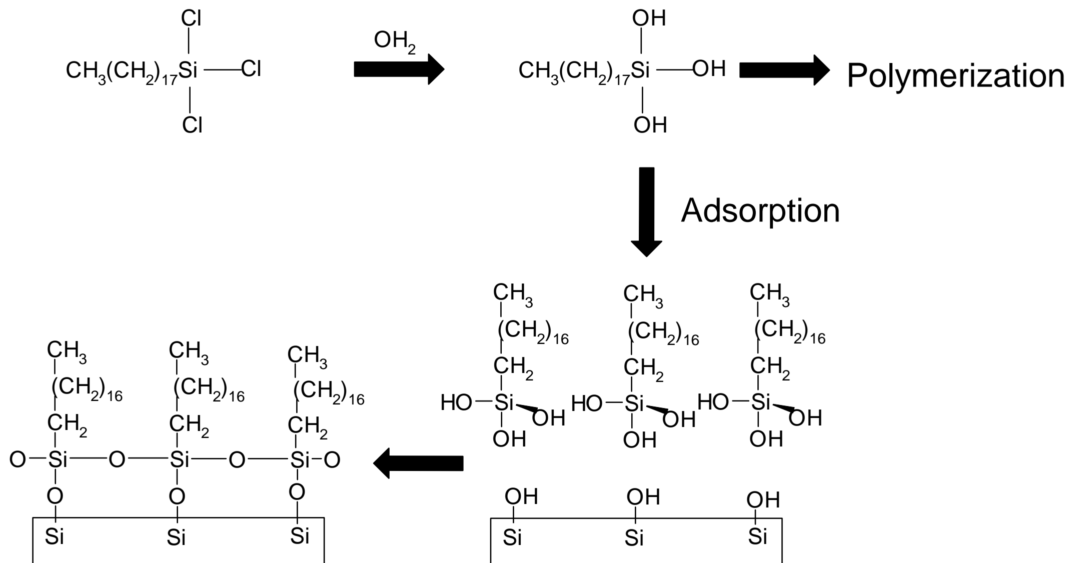

Figure 44: OTS reaction mechanism: hydrolysis of the molecule, adsorption to the surface and condensation to form a SAM. If there is a water excess an undesired polymerization starts.

Two experimental ways to obtain OTS SAM onto the silicon dioxide surface were carried out. First of all, the wet treatment: a solution of 1 mL of OTS in 1000 mL of heptane was prepared, then wet cleaned SiO_2 substrates (Section 5.1.1) were dipped into the solution. The solution with the samples was sealed, in order to prevent further atmospheric water penetration, and samples were left immersed for 2 hours. Finally, substrates are repeatedly rinsed with heptane and dried with an argon flux. This procedure does not yield good SAM because of the large water excess that, as already mentioned, causes undesired polymerization.

The other procedure was performed in gas phase (Figure 45). The OTS was put in a crucible supported by a glass cylinder inside a vial. On top of the cylinder, cleaned substrates with top oriented SiO_2 side were arranged. This geometry is needed because OTS gas moves upwards. Vacuum is performed with a rotary pump alternated with argon vent. Finally, a low vacuum atmosphere was left ($P \sim 10^0$ mbar). Low vacuum permits the persistence of a small quantity of water necessary to the reaction. The vial was dipped in an oil bath set at 170°C; OTS sublimes and the reaction takes place. The vial was left immersed and in vacuum for 3-5 hours. Finally, substrates were repeatedly rinsed with dichloromethane.

The drawback of this second treatment is the uncertain completion SAM formation. Anyhow, this procedure was selected because it is more reproducible and devices grown on this kind of substrates showed better electrical characteristics. The film quality was controlled by contact angle measurements.

A typical contact angle value for the OTS treated silicon dioxide which was used is $\theta_c = 97° \pm 2°$.

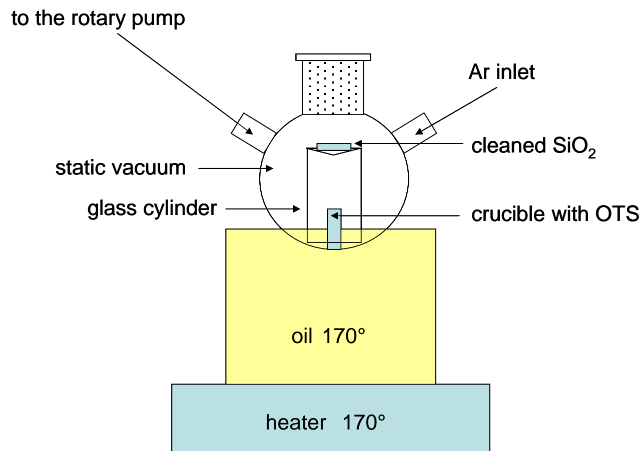

Figure 45: OTS gas phase set up.

5.2.2 *1,1,1,3,3,3-hexamethyldisilazane (HMDS) treatment*

The reaction of silicon dioxide with HMDS is extensively used in microelectronics, because silanole groups present at the SiO_2 surface act as charge traps (Section 3.3.2.2). Each HMDS molecule reacts with two hydrophilic Si-OH, and transforms them into hydrophobic Si-O-Si$(CH_3)_3$ (Figure 46). A Si atom of the HMDS molecule binds to the –OH oxygen. It substitutes the H atom, which binds to the ammonium group releasing NH_3 gas. It is noteworthy that HMDS treatment leaves thermal oxide with lower contact angle values with respect to OTS treatment, as HMDS does not form a SAM but binds a single Si atom to -OH surface groups. This is due to HMDS not being able to cross-link intermolecuarly. Its tetrahedral geometry does not allow it to pack with strong lateral interactions, therefore it cannot form compact films.

Typical contact angle values for the HMDS treated silicon dioxide that we used is $\theta_c = 95° \pm 2°$.

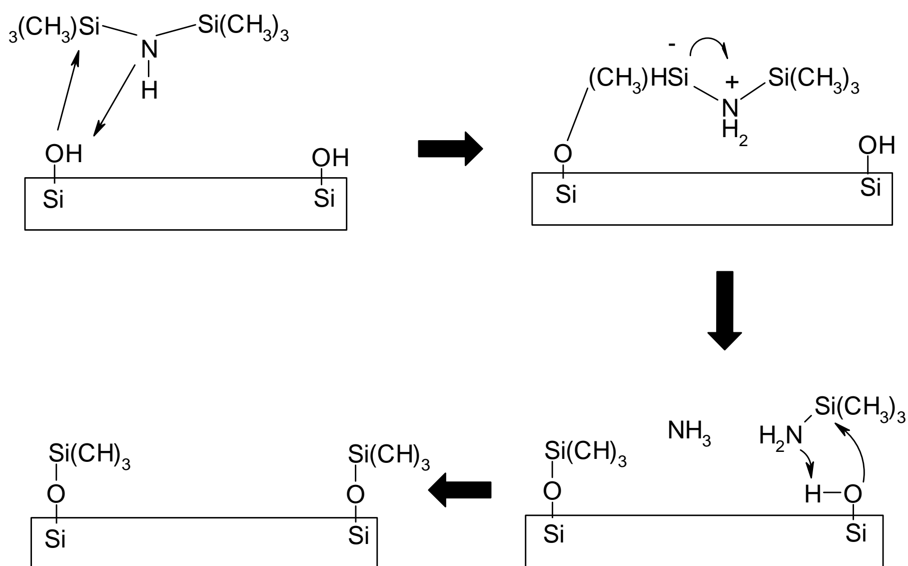

Figure 46: HMDS reaction with –OH groups. NH_3 gas is released during the reaction.

HMDS treatment was performed in gas phase. HMDS is put inside a vial, on a crucible surrounded by cleaned substrates (in this case the glass cylinder used in OTS case is not necessary because HMDS does not move upwards but goes all around). Subsequent cycles of vacuum and argon atmosphere are yielded by a rotary pump, so leaving the vial in vacuum conditions. HMDS is more volatile than OTS, thus the atmosphere gets saturated of HMDS gas even without heating. The vial was left in vacuum for 10-12 hours, then samples were repeatedly rinsed with dichloromethane.

5.3 Dielectric polymer buffer layers

In this thesis three dielectric polymers were used as buffer layer on top of the thermal silicon dioxide dielectric layer: polyvinilyalchol (PVA), polymethylmetacrilate (PMMA) and a cyclotene derivative (B-staged bisbenzocyclobutene or BCB). This strategy was adopted because, as already stressed, the SiO_2 surface is rich in charge carrier traps (e.g. –OH groups, etc…) and we wanted different surfaces in intimate contact with the active OS in order to improve the OFET performances.

5.3.1 Poly(vinyl alcohol) [PVA]

Poly(vinyl alcohol) is a completely water soluble polymer and is thus used as a thickener in some suspensions and emulsions. It is generally amorphous, with a typical density of 1.26 g/cm^3. Its glass transition temperature is around 85°C (depending on molecular weight) and the monomer weight is 44.00 g/mol (Figure 47). The PVA we employed is Mowiol 40-88 supplied by Sigma-Aldrich.

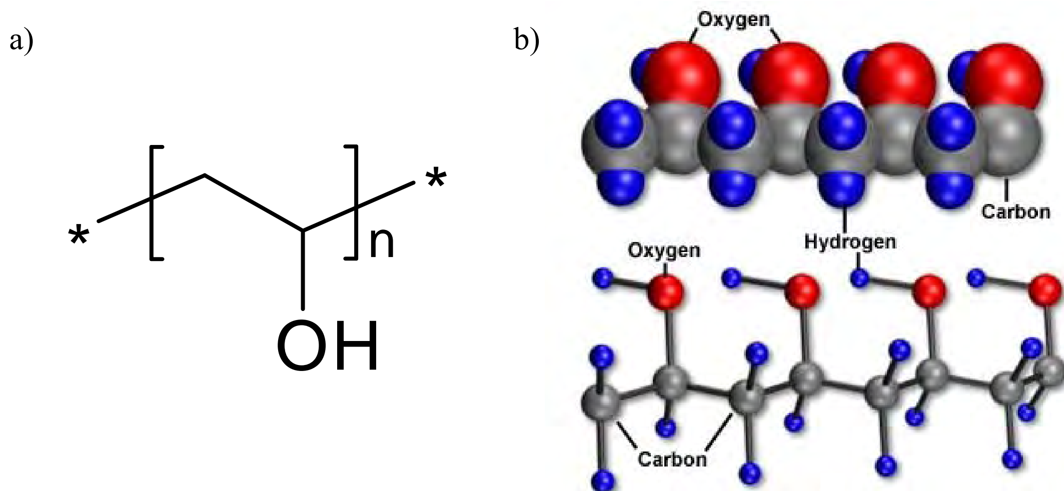

Figure 47: a) PVA repetition unit; b) 3D back-bone structure of PVA.

The dielectric constant value obviously varies with frequency. A low frequency value was selected, because in our measurements devices are operated in a quasi-steady state. Furthermore, we verified that the dielectric constant does not vary drastically with frequency. Variations slightly involved mobility values (some percent at maximum) and did not affect the analysis of our results. The value used for the PVA capacitance per unit area calculation is: $\varepsilon_{PVA} = 6.9$ at 100 KHz[6].

PVA films are obtained via spin-coating, after the wet cleaning of the SiO_2 substrates (Section 5.1.1), using 200 μL of a 10 g/L water solution at 1500 rpm. In these conditions, we obtain 50 ± 5 nm thick films.

From these data, and observing that our film is similar to a plane plate capacitor, we calculated the capacitance per unit area of the dielectric PVA thin film as:

$$\frac{C}{A_0} = \frac{\varepsilon_0 \varepsilon_{PVA}}{d} = 8.85 \cdot 10^{-14} \left[\frac{Far}{cm}\right] \frac{1}{50 \cdot 10^{-7}} \left[\frac{1}{cm}\right] 6.9 = 1.22 \cdot 10^{-7} \left[\frac{Far}{cm^2}\right]$$

where ε_0 is the vacuum dielectric constant and d the film thickness.

After the PVA deposition on top of the silicon dioxide, our device presents a double dielectric layer. The total capacitance of the dielectric was calculated, as the total capacitance of two capacitors in series[7], the SiO_2 electrical capacitance plus the polymeric one:

$$\frac{1}{C_{PVA}^{tot}} = \frac{1}{C_{SiO_2}} + \frac{1}{C_{PVA}} = \frac{1}{1.80 \cdot 10^{-8}} \left[\frac{Far}{cm}\right] + \frac{1}{1.22 \cdot 10^{-7}} \left[\frac{Far}{cm}\right]$$

The total capacitance per unit area value, for a device with PVA buffer layer, is:

$$C_{PVA}^{tot} = 1.57 \cdot 10^{-8} \left[\frac{Far}{cm}\right]$$

The substrates obtained were thermally annealed at 80°C for 12 hours (around PVA glass temperature) before the active material growth, in order to facilitate the residual solvent evaporation.

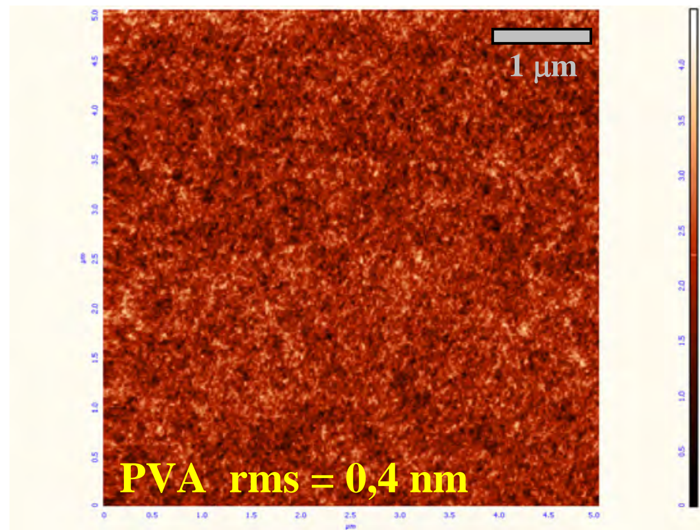

Figure 48: 5 x 5 μm^2 Atomic Force Microscopy (AFM) images of PVA films spin-cast onto silicon dioxide.

RMS roughness values of the annealed films, measured by AFM, are around 0.4 nm (Figure 48). Contact angle measurements are not performed because PVA is water soluble and it ideally presents a $\theta_c = 0°$.

5.3.2 Poly(methyl methacrylate) [PMMA]

Poly(methyl methacrylate) is a clear, colourless polymer extensively used in optical applications. It is commercially available in both pellet and sheet form. It is an amorphous polymer with a typical density of 1.17 g/cm^3. Its glass transition temperature is around 114°C (depending on the molecular weight) and the monomer weight is 100.12 g/mol (Figure 49). A 950K molecular weight PMMA in 3% wt. ethyl-lactate solution supplied by All Resist was used.

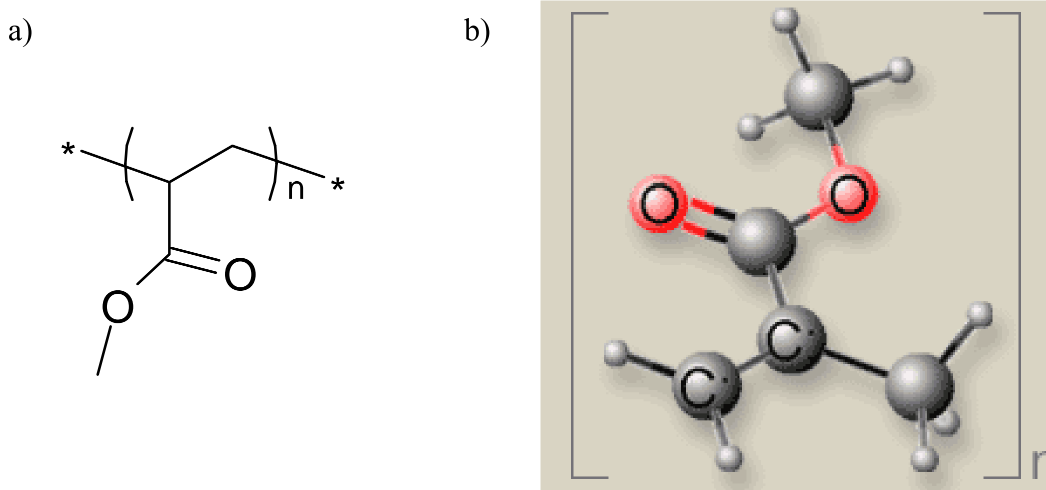

Figure 49: a) PMMA repetition unit; b) 3D back-bone structure of PMMA.

As already mentioned for PVA (Section 5.3.1), a low frequency dielectric constant value for PMMA was selected, because in our measurements devices are operated in a quasi-steady state, therefore we used $\varepsilon_{PMMA} = 3.6$ at 100 Hz[8].

PMMA films are obtained via spin-coating, after the wet cleaning of the SiO_2 substrates (Section 5.1.1), using 150 μL of a 3% wt ethyl-lactate solution at 6000 rpm, yielding 130 ± 7 nm thick films.

From this data, following the assumption of the PVA case, we calculated the capacitance per unit area of the dielectric PMMA thin film as:

$$\frac{C}{A_0} = \frac{\varepsilon_0 \varepsilon_{PMMA}}{d} = 8.85 \cdot 10^{-14} \left[\frac{Far}{cm}\right] \frac{1}{130 \cdot 10^{-7}} \left[\frac{1}{cm}\right] 3.6 = 2.45 \cdot 10^{-8} \left[\frac{Far}{cm^2}\right]$$

Considering the presence of the silicon dioxide layer, the total capacitance for a device with a PMMA buffer layer, is:

$$C_{PMMA}^{tot} = 1.04 \cdot 10^{-8} \quad \left[\frac{Far}{cm}\right]$$

The substrates obtained were thermally annealed at 120°C for 12 hours before the active material growth, in order to facilitate the residual solvent evaporation.

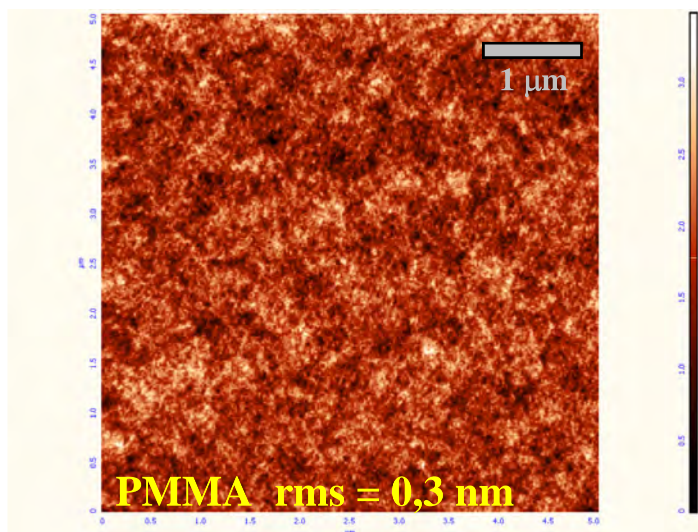

Figure 50: 5 x 5 µm^{2}Atomic Force Microscopy (AFM) images of spin-coated PMMA film onto silicon dioxide.

RMS roughness values of the annealed films, measured by AFM, are around 0.3 nm (Figure 50). Contact angle measurements were also performed, giving a typical value of $\theta_c = 61° \pm 2°$.

5.3.3 Bisbenzocyclobutene derivative [BCB]

BCB or B-staged bisbenzocyclobutene is a cyclotene derivative (Figure 51). It is a resin formulation designed for dielectric and planarization applications. Its glass transition temperature is above 350°C (depending on molecular weight). BCB supplied by *The Dow Chemical Company* (Resin XU.71918) in a 10% weight solution of mesitylene (tri-methyl benzene) was used.

BCB is not a widely diffused commercial polymer, so the dielectric constant supplied by the producer and reported in literature[9] was used for data analysis: $\varepsilon = 2{,}65$ at 1 GHz.

BCB films are obtained via spin-coating, after the plasma cleaning of the SiO_2 substrates (Section 5.1.2). In this case oxygen plasma cleaning instead of the wet procedure is used, in order to provide a better film adhesion. We employed 90 µL a 10% wt. solution of BCB in mesitylene. The spinning process is performed at 6000 rpm, obtaining 121 ± 2 nm thick films.

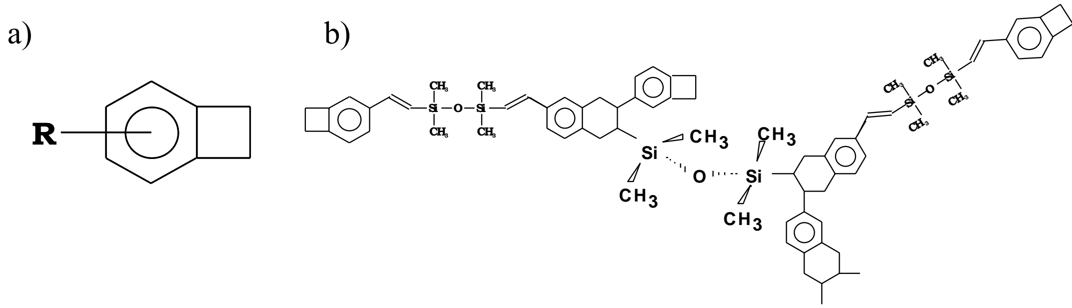

Figure 51: a) Benzo cyclo butene group; b) BCB polymer structure

As in the previous cases, the capacitance per unit area of the dielectric BCB thin film was calculated:

$$\frac{C}{A_0} = \frac{\varepsilon_0 \varepsilon_{BCB}}{d} = 8.85 \cdot 10^{-14} \left[\frac{Far}{cm}\right] \frac{1}{121 \cdot 10^{-7}} \left[\frac{1}{cm}\right] 2.65 = 1.95 \cdot 10^{-7} \left[\frac{Far}{cm^2}\right]$$

Considering the silicon dioxide layer presence, the total capacitance for a device with BCB buffer layer, is:

$$C_{BCB}^{tot} = 9.36 \cdot 10^{-9} \left[\frac{Far}{cm}\right]$$

For optimal BCB cross-linking, films followed this thermal curing process: they were held at room temperature for 15 minutes; they underwent a temperature ramp from 30°C to 150°C at 4°C/min; were held at 150°C for 30 minutes; a second temperature ramp was performed from 150°C to 250°C in 1 hour; samples were held at 250° for 1 hour and finally quenched down to room temperature.

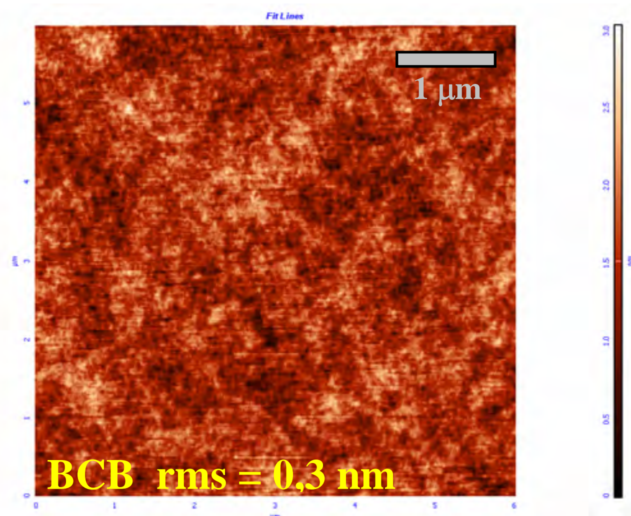

Figure 52: 6 x 6 µm^{2}Atomic Force Microscopy (AFM) image of spin-coated BCB film onto silicon dioxide.

RMS roughness values of the annealed films, measured by AFM, are around 0.3 nm (Figure 52). Contact angle measurements were also performed, giving a typical value of $\theta_c = 89° \pm 2°$.

5.4 Dielectric/OS interface in PPV based OFETs

Gaining new understanding of the dielectric/organic interface is crucial in order to improve OFETs performances. Therefore, the active material and the device structure were kept fixed and the dielectric layer changed to perform a systematic OFETs performance analysis. A systematic investigation on two p-type polymers was carried out: MEH-PPV, (Poly[2-methoxy-5-(2-ethylhexyloxy)-1,4-phenylenevinylene], figure 53.a) and OC_1C_{10}-PPV (Poly[2-methoxy-5-(3,7-dimethyloctyloxy)-1,4-phenylenevinylene], figure 53.b) grown on the afore-mentioned dielectric species.

5.4.1 Poly-phenylenevinylene derivatives

MEH-PPV and OC_1C_{10}-PPV are widely used in organic electronics[10-15] and can be considered representative of a wide class of polymer semiconductors.

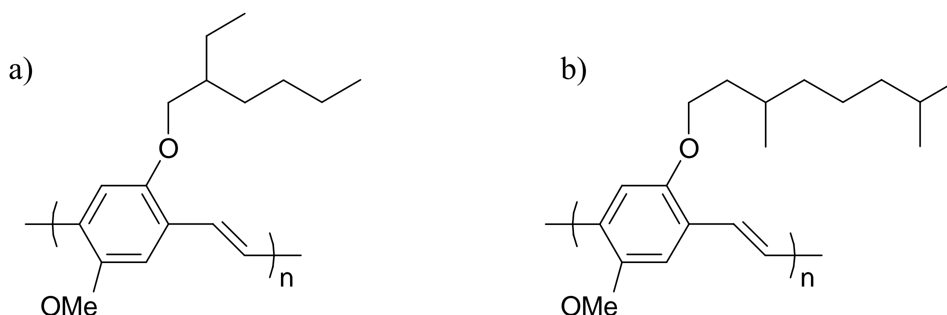

Figure 53: Chemical structure of the MEH-PPV (a) and OC_1C_{10}-PPV (b) monomer.

MEH-PPV was purified by chromatography, while OC_1C_{10}-PPV was used as received from ADS dyes. Before using these materials, their glass transition temperature (T_g) was measured by Differential Scanning Calorimetry (DSC). The respective values are: 78.3°C for MEH-PPV and 17.8°C for OC_1C_{10}-PPV. Furthermore, a basic study of their optical properties (absorption and photoluminescence) was performed (Figure 54) to check the commercial product characteristics .

Thin films of about 100 nm of MEH-PPV were obtained via spin-coating, using 150 µL of a 10 g/L chlorobenzene solution, at 2500 rpm for 75 seconds. For OC_1C_{10}-PPV 75 µl of a 5 g/L chlorobenzene solution, spun at 2000 rpm for 75 seconds were used, in order to obtain the same film thickness.

Devices were operated after annealing for 15 minutes at 100°C, with the exception of PMMA dielectric devices. In the MEH-PPV on PMMA case samples were analyzed as deposited, annealed at 75°C and 100°C. As for OC_1C_{10}-PPV on PMMA, samples were studied as deposited, annealed at 50°C and 100°C. Because the active films annealing is extremely important to optimise the OFET behaviour, we decided to study the electrical response at different annealing temperatures for the PMMA case which gave us the best results (Section 5.4.2.3).

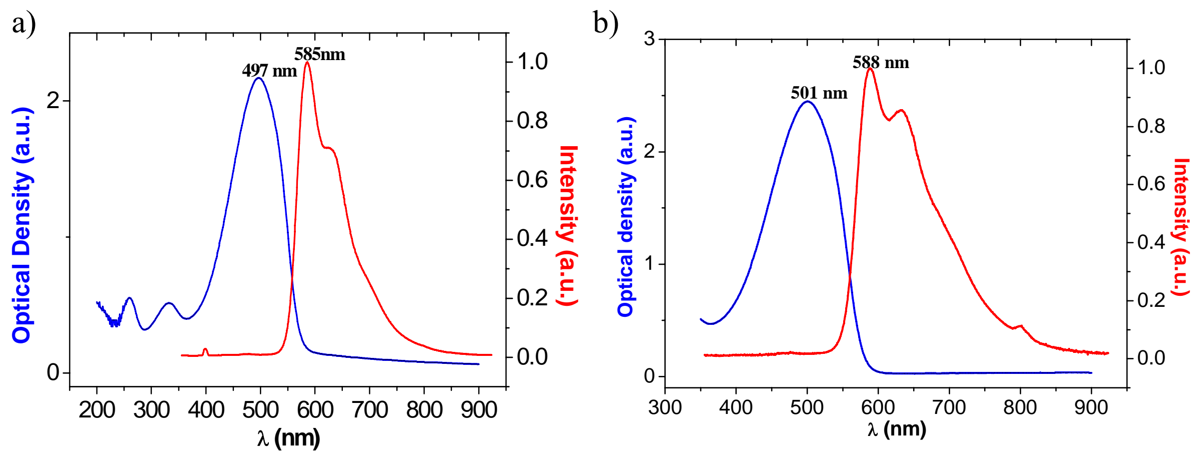

Figure 54: Absorption (blue curves) and emission (red curves) spectra of MEH-PPV (a) and OC_1C_{10}-PPV (b).

5.4.2 *Electrical characteristics of PPV based OFETs*

This section reports the electrical performances of devices based on PPVs derivatives, grown on different substrates. Mobility and threshold voltage values are obtained from locus curves, while On/Off ratio values are derived from output curves (as described in Section 3.2.2). BG-TC geometry and 50 nm thick Au source-drain contacts were used for all devices.

5.4.2.1 *OFETs with pristine silicon dioxide*

The first step of this study was dedicated to analyze MEH-PPV based OFETs, grown on silicon dioxide cleaned substrates without any further treatment. This was meant to identify the most effective cleaning procedure to obtain the best OFET electrical performances. For this purpose, the three above mentioned (Section 5.1) standard cleaning protocols were used

In order to comprehend our results, it has to be considered that cleaning procedures alter the silanol density, thus affecting the OFET performance. Results obtained with the “wet cleaning” procedure (Table 1, Figure 55.a) were used as a reference, because this protocol simply removes any organic contamination due to air exposure; silanol density remains thus

unvaried with respect to uncleaned samples. Silanol density depends on the modality of the thermally driven oxide growth and is not easy to control. The typical field-effect μ values of the MEH-PPV was measured in devices prepared with this method. All output curves present low saturation: at high drain-source voltages the curves do not reach a plateau, and have high hysteresis (Figure 56.a)

The oxygen plasma procedure is not only supposed to remove the organic contaminations, but also to increase silanol density. Accordingly (Section 3.3.2.2), we obtained a reduction of μ that was reproducible in all the analyzed devices. We also observed lower On/Off ratio values and similar V_t (Table 1). The output curves showed comparable hysteresis (Figure 56.b).

Active material	***Treatment***	***μ (cm²/Vs)***	***V_t (V)***	***On/Off ratio***
MEH-PPV	wet	6.0×10^{-5}	-10.9	6.6×10^{2}
MEH-PPV	plasma	4.2×10^{-5}	-8.5	1.3×10^{2}
MEH-PPV	HF	2.8×10^{-5}	-6.7	1
OC_1C_{10}-PPV	wet	2.5×10^{-5}	-8.7	1.3×10^{2}

Table 1: Electrical data of OFETs grown on SiO_2 as dielectric layer with different cleaning protocols: hole mobility (μ), threshold voltages (V_t) and On/Off ratios.

HF cleaning protocol is intended to etch a certain amount of SiO_2. Silanol groups are removed from the pristine SiO_2 surface, leaving Si-O-Si terminal groups. Electrical parameters are the worst of all (Table 1), although the etched surface has the same RMS roughness of the others, about 0,5 nm. The I-V curves show high hysterisis and there is no difference between the drain-source current at high or low gate voltages (Figure 56.c). This is due to the reaction of instable Si-O-Si groups with air humidity that reintroduces the silanol groups. In our procedure, this reaction was supposed to occur almost immediately, as the active material is spin-coated after a few minutes only. Reintroducing silanol groups causes a deterioration of the dielectric layer and of the interface with the semiconducting polymers, leading to lower performance OFET devices.

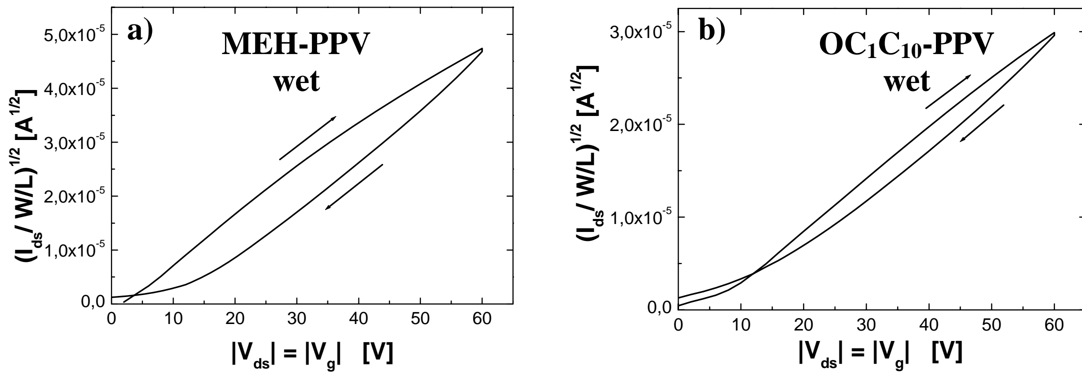

Figure 55: Locus curves of wet cleaned OFETs based on: a) MEH-PPV on SiO_2; OC_1C_{10}-PPV on SiO_2. I_{ds} is normalized with respect to the channel width (W) and length (L)

These data suggest that the "wet" cleaning protocol is the best option to build OFETs using as-grown SiO_2 as dielectric layer without any further treatment. In particular, it yielded the highest μ and On/Off ratio, whereas V_t did not vary noticeably. Furthermore, this cleaning procedure allows one to obtain a good film adhesion without dewetting, as it can occur in case of other surface treatments. That being so, for OC_1C_{10}-PPV we decided to study only the electrical characteristics of wet cleaned OFETs. The results are similar, as expected, to the MEH-PPV ones (Table 1, Figure 55.b), hysterisis is also in the same range (Figure 56.d).

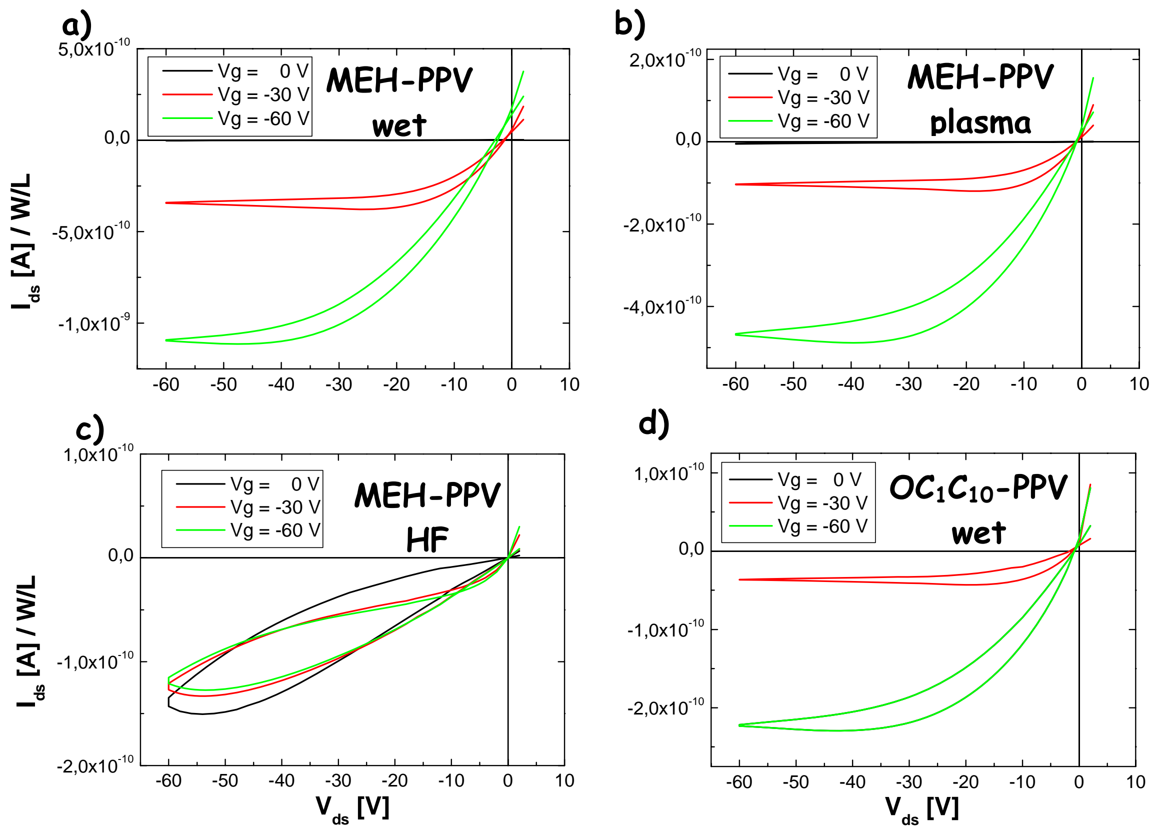

Figure 56: Output curves for PPVs based OFETs cleaned with different procedure: a) MEH-PPV on wet cleaned SiO_2; b) MEH-PPV on plasma cleaned SiO_2; c) MEH-PPV on HF cleaned SiO_2; d) OC_1C_{10}-PPV on wet cleaned SiO_2. I_{ds} is normalized with respect to the channel width (W) and length (L).

5.4.2.2 OFETs with gas phase treated silicon dioxide

After the preliminary study of the characteristics of devices fabricated using different cleaning protocols, the SiO_2 surface was treated in different ways, in order to change the chemical properties and the physical adhesion characteristics of the dielectric/organic interface. For this purpose, two molecular species were used: octadecyltrichlorosilane (OTS) and hexamethyldisilazane (HMDS) (Section 5.2). In both cases the “wet” cleaning protocol for the SiO_2 surface was employed before any treatment.

Active material	*Treatment*	*μ (cm^2/Vs)*	*V_t (V)*	*On/Off ratio*
MEH-PPV	wet + OTS	1.2×10^{-4}	-11.1	7.5×10^{2}
MEH-PPV	wet + HMDS	1.3×10^{-3}	-9.1	4.9×10^{2}
OC_1C_{10}-PPV	wet + OTS	1.6×10^{-4}	-14.4	1.7×10^{2}
OC_1C_{10}-PPV	wet + HMDS	1.3×10^{-3}	-22.1	1.7×10^{2}

Table 2: Electrical data of OFETs grown on gas phase treated SiO_2 as dielectric layer: hole mobility (μ), threshold voltages (V_t) and On/Off ratios.

Unexpectedly, OTS treatment does not significantly improve electrical properties; only a slight increase in μ can be observed with respect to the wet cleaning (Table 2, Figure 57.a,b). OTS forms a SAM anchored to some silanol groups. When completely formed, silanol groups should be fully screened. We therefore assume that either the SAM formed using the gas phase technique is not continuous and does not fully screen the silanol groups, or that OTS molecules interact with the active polymer forming traps. It has been recently shown that a second step to endcap residual –OH groups with HMDS is needed[16] to improve the quality of the OTS gas phase treatment. It is therefore likely that this causes the poor response which was observed. V_t values were higher than in untreated devices and On/Off ratios remained similar.

HMDS treatment substantially improves the OFET performances: much higher μ, whereas V_t and On/Off ratio were comparable with those obtained with the “wet” cleaning procedure (at least for MEH-PPV, Table 2, Figure 57.c,d).

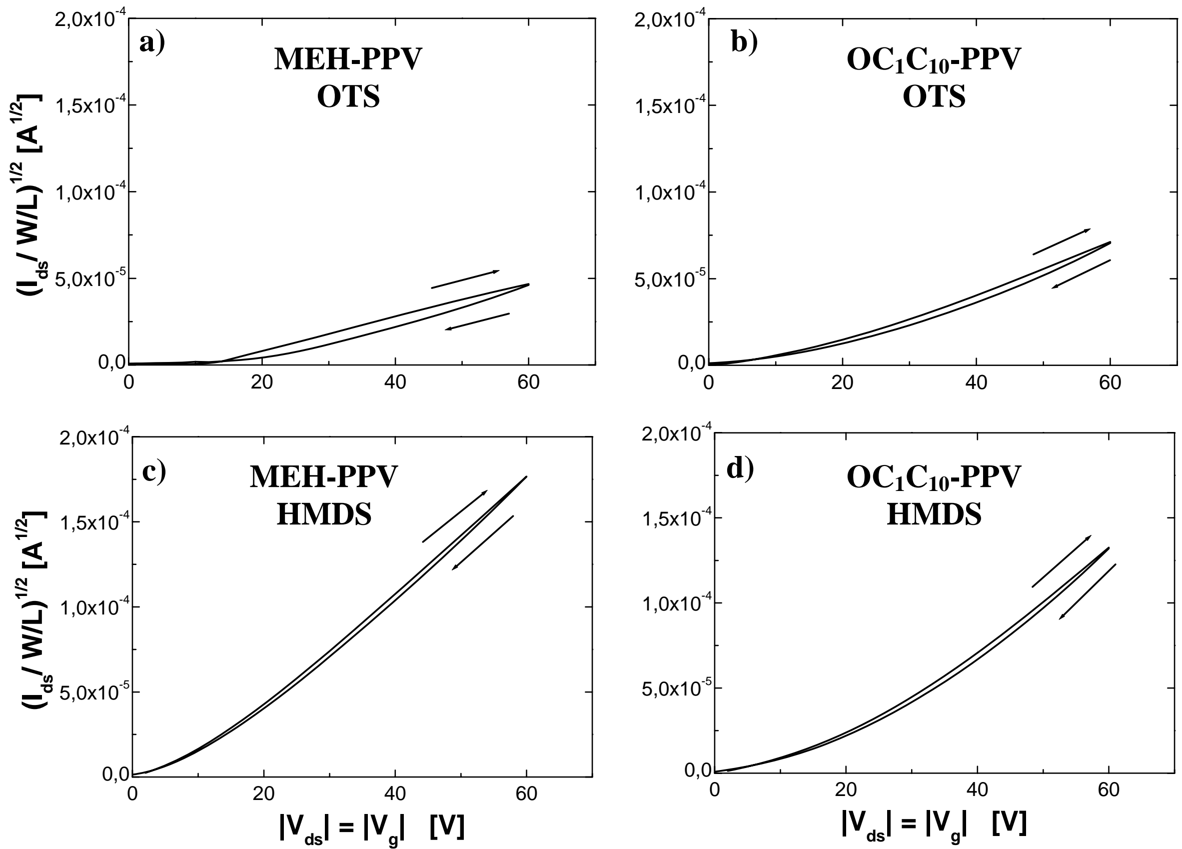

Figure 57: Locus curves of OFETs with different gas phase treatments of SiO_2: a) MEH-PPV on OTS treated SiO_2; b) OC_1C_{10}-PPV on OTS treated SiO_2; c) MEH-PPV on HMDS treated SiO_2; d) OC_1C_{10}-PPV on HMDS treated SiO_2. The maximum of the y axis is fixed at 2.0×10^{-4} $A^{1/2}$ in order to allow the direct comparison of the I_{ds} currents and of the hysterisis in OFETs with different treatments. I_{ds} is normalized with respect to the channel width (W) and length (L).

The I-V curves present good saturation and the current hysteresis is reduced with respect to pristine substrates in both cases, although it is slightly better for HMDS (Figure 58).

In HMDS case, too, we observed that the treatment quality is very important. We observed that μ increases as the contact angle increases (Table 3). The contact angle is a direct measurement of the silanol density. This means that better HMDS treatments reduce both silanol density and free surface traps. These results show that silanol groups can not only trap electron carriers, but also hole carriers. Holes trapping due to the –OH groups has never been reported before.

θ_c	μ (cm^2/Vs)	V_t (V)	On/Off ratio
87° ± 2	3.8×10^{-4}	- 6.0	1.2×10^{1}
90° ± 2	7.5×10^{-4}	- 5.6	2.6×10^{2}
95° ± 2	1.3×10^{-3}	- 9.1	4.9×10^{2}

Table 3: Electrical data of MEH-PPV based OFETs on HMDS treated SiO_2. A higher value of the contact angle (θ_c) is related to a lower density of the silanol (Si-OH) groups.

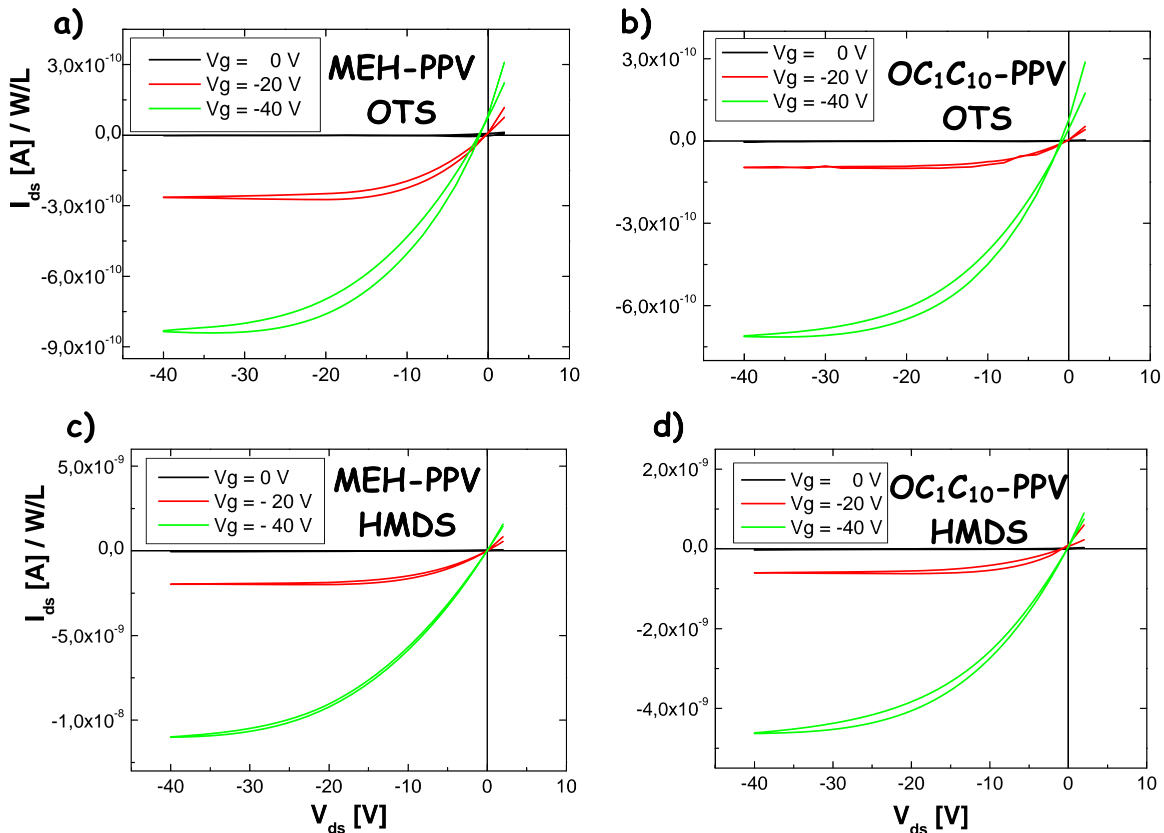

Figure 58: Output curves of OFETs with different gas phase treatments of SiO_2: a) MEH-PPV on OTS treated SiO_2; b) OC_1C_{10}-PPV on OTS treated SiO_2; c) MEH-PPV on HMDS treated SiO_2; d) OC_1C_{10}-PPV on HMDS treated SiO_2. I_{ds} is normalized with respect to the channel width (W) and length (L).

5.4.2.3 OFETs with a polymer dielectric buffer layer

Finally, OFETs devices were investigated in which the SiO_2 surface was covered with a polymeric buffer thin film using three different dielectric polymers: PVA, PMMA and BCB (Section 5.3). The deposition of a thick polymeric dielectric film is sufficient to fully screen the influence of silanol groups that remain deep down the surface.

Before the PVA and PMMA spin-coating, the “wet” cleaning protocol was employed for SiO_2 surfaces, while only in the BCB case oxygen plasma cleaning was used to provide a better film adhesion. Electrical data are reported in Table 4.

Starting with PVA, we observed that μ values were lower in both MEH-PPV and OC_1C_{10}-PPV with respect to HMDS (Table 4) and the current hysteresis in the curves was higher (Figure 59.a,b). The I-V curves do not reach a well defined plateau at high drain-source voltages (Figure 60.a,b). We can explain this behavior noting that PVA still presents –OH groups in the polymer chain, though in a different chemical environment and with different acidity, as they are linked to aliphatic groups, with respect to the SiO_2.

Active material	*Treatment*	*μ (cm²/Vs)*	*V_t (V)*	*On/Off ratio*
MEH-PPV	wet + PVA	3.5×10^{-4}	-15.7	2.6×10^{3}
MEH-PPV	wet + PMMA	1.3×10^{-3}	-8.7	3.9×10^{3}
MEH-PPV	plasma + BCB	3.3×10^{-3}	-18.7	2.6×10^{3}
OC_1C_{10}-PPV	wet + PVA	3.9×10^{-4}	-15.2	1.1×10^{3}
OC_1C_{10}-PPV	wet + PMMA	1.1×10^{-3}	-18.5	1.9×10^{3}
OC_1C_{10}-PPV	plasma+ BCB	7.1×10^{-4}	-20.9	6.9×10^{2}

Table 4: Electrical data OFETs grown on SiO_2 covered with a polymeric dielectric layer: hole mobility (μ), threshold voltages (V_t) and On/Off ratios.

Furthermore, the polymer film has an amorphous structure with the chains bundled together. On average, OH groups are randomly oriented and the total dipolar moment at the dielectric interface should be zero. Electrical performances are the worst, if compared to HMDS, but still better with respect to pristine SiO_2 surfaces. This is the evidence that the PVA polymer –OH groups still act as traps. The lower trapping efficiency of these groups on PVA, with respect to pristine SiO_2 surface, can be explained in two ways: either the density of properly aligned dipoles at the free surface is lower in PVA than in SiO_2, or the silanol group dipolar strength is larger than the one of OH groups linked to aliphatic chains.

On the contrary, when employing PMMA, almost no hysteresis and a good saturation of the curves at high drain-source voltages were found (Figure 59.c,d and Figure 60.c,d). μ values were always higher than in HMDS and PVA, with better On/Off ratio and similar or lower V_t (Table 4). These electrical characteristics were the best observed using polymeric treatments and the best ever observed in literature. High μ values (Table 4) with good electrical characteristics (Figure 59.e,f) were also obtained when using BCB as dielectric layer. The output curves showed fairly good saturation and rather low hysteresis (Figure 60.e,f), although not as good as the PMMA treatment. On/Off ratios were similar to PMMA. The only drawback was a slight increase in V_t values. PMMA and BCB do not contain any –OH species. Therefore, the large improvements in the electrical characteristics are well in accordance with this scenario.

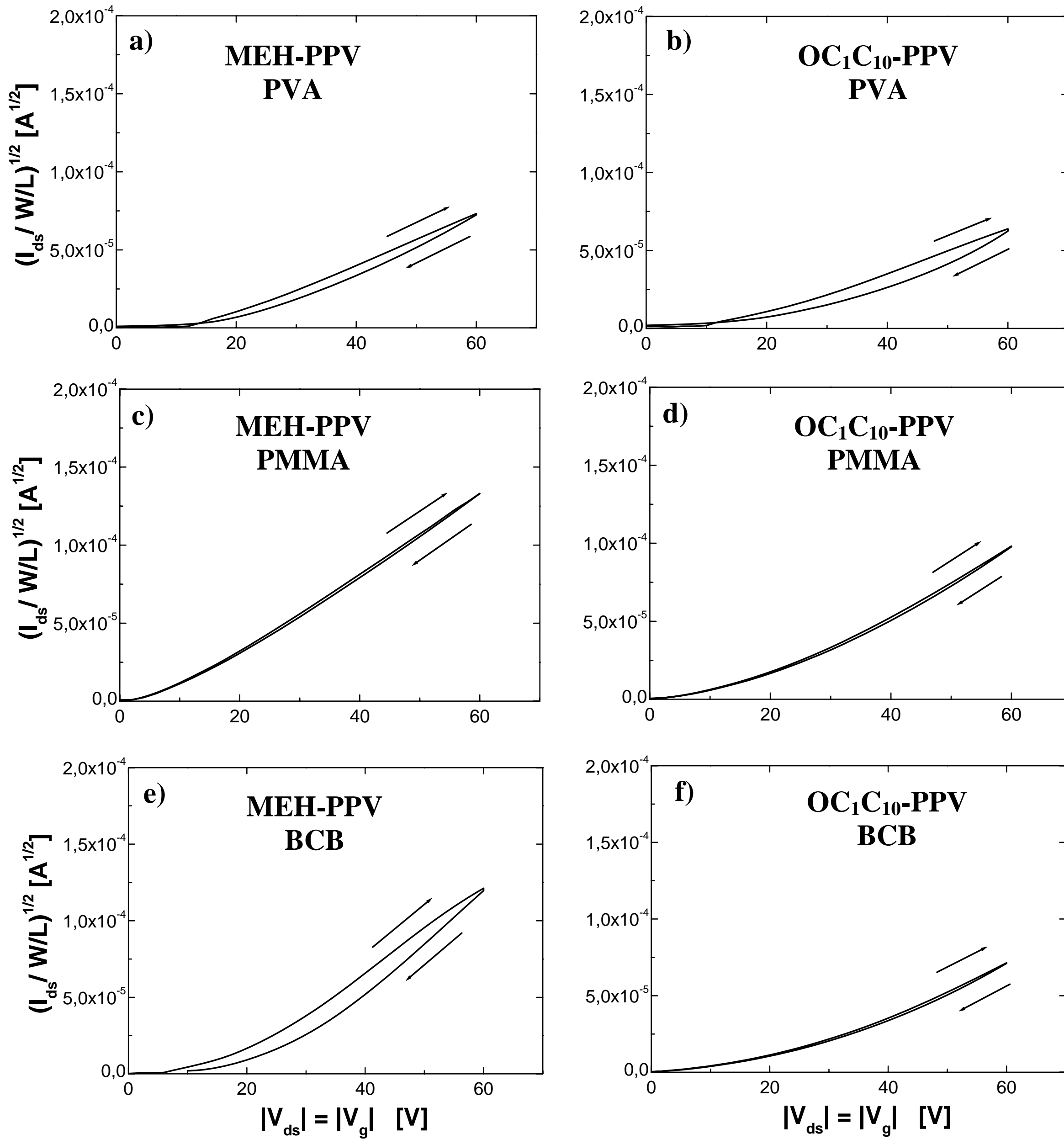

Figure 59: Locus curves of OFETs with polymer buffer layer: a) MEH-PPV on PVA coated SiO_2; b) OC_1C_{10}-PPV on PVA coated SiO_2 ; c) MEH-PPV on PMMA coated SiO_2; d) OC_1C_{10}-PPV on PMMA coated SiO_2; e) MEH-PPV on BCB coated SiO_2; f) OC_1C_{10}-PPV on BCB coated SiO_2. As for the curves of gas phase treated devices, the maximum of the y axis is fixed at 2.0 x 10^{-4} $A^{1/2}$ in order to allow the direct comparison of the I_{ds} currents and of the hysterisis in OFETs with different treatments. I_{ds} is normalized with respect to the channel width (W) and length (L).

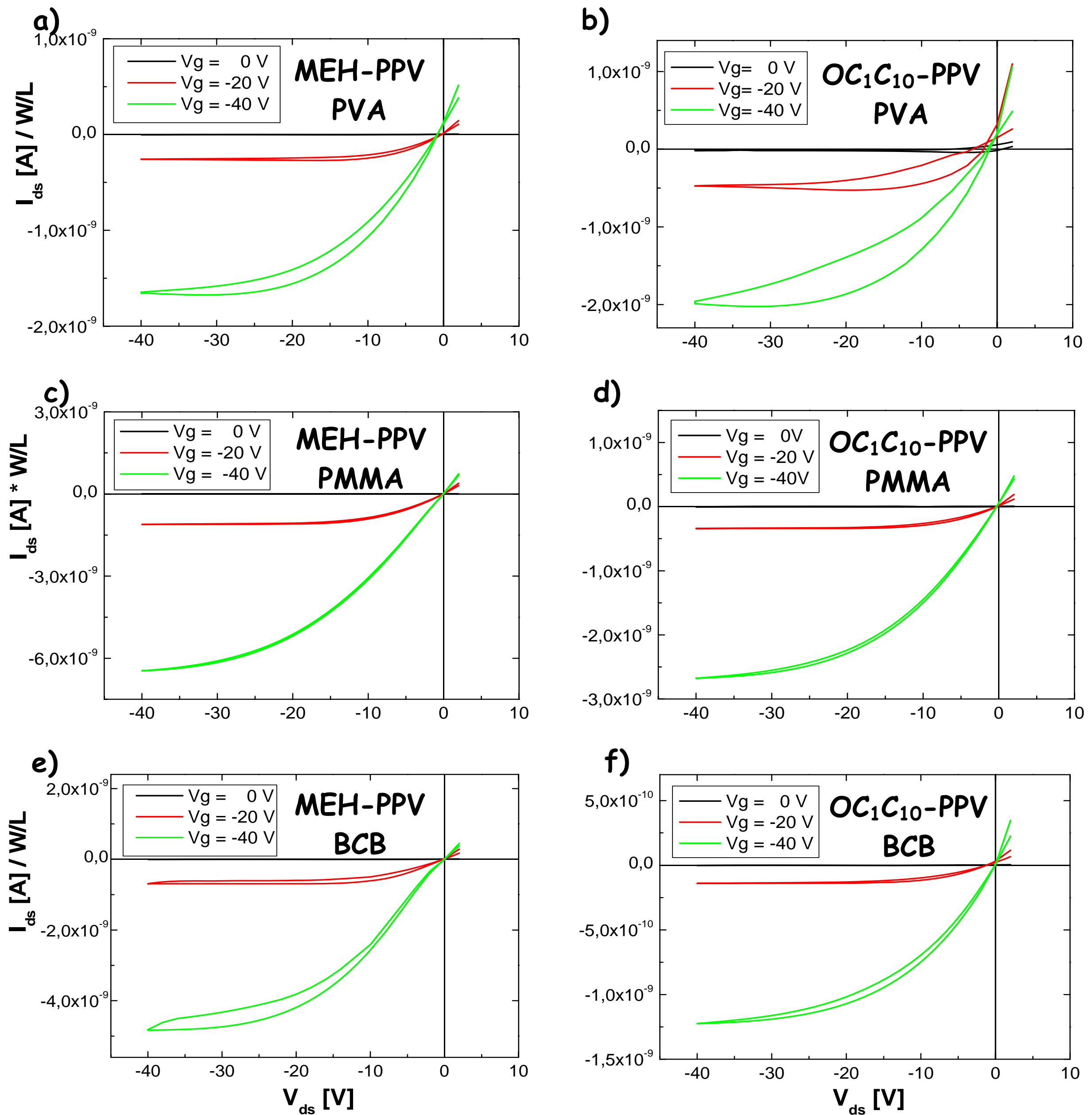

Figure 60: Output curves of OFETs with polymer buffer layer: a) MEH-PPV on PVA coated SiO_2; b) OC_1C_{10}-PPV on PVA coated SiO_2; c) MEH-PPV on PMMA coated SiO_2; d) OC_1C_{10}-PPV on PMMA coated SiO_2; e) MEH-PPV on BCB coated SiO_2; f) OC_1C_{10}-PPV on BCB coated SiO_2. I_{ds} is normalized with respect to the channel width (W) and length (L).

Annealing the active films is extremely important to optimise the OFET behaviour, therefore we decided, as already mentioned (Section 5.4.1), to study the electrical response at different annealing temperatures (Table 5) for both the active polymers on PMMA, our best case. In the MEH-PPV (T_g = 78.3°C) on PMMA case, samples were analyzed as deposited, annealed at 75°C (around the T_g) and 100°C. For OC_1C_{10}-PPV (T_g = 17.8°C) on PMMA samples were studied as deposited, annealed at 50°C and 100°C. The best electrical characteristics in the former active material were obtained after annealing for 15 minutes at 75 °C. Similar values were obtained in devices annealed at 50°C for 15 minutes. Dewetting (Section 5.4.3) of the

active materials, associated with a large degradation of the electrical characteristics were noticed at higher annealing temperatures and same annealing times. The same behaviour was observed in OC_1C_{10}-PPV. In this latter case the best OFET performances were obtained with no annealing.
In both cases, the best performances were reached when devices were annealed around the T_g of their own active materials.

Active material	*Treatment*	*Annealing T (°C)*	μ *(cm²/Vs)*	V_t *(V)*	*On/Off ratio*
MEH-PPV	wet + PMMA	R.T.	1.1×10^{-3}	-8.8	1.3×10^{3}
MEH-PPV	wet + PMMA	75	1.3×10^{-3}	-8.7	3.9×10^{3}
MEH-PPV	wet + PMMA	100	8.3×10^{-4}	-11.6	8.3×10^{2}
OC_1C_{10}-PPV	wet + PMMA	R.T.	1.1×10^{-3}	-15.5	1.9×10^{3}
OC_1C_{10}-PPV	wet + PMMA	50	9.6×10^{-4}	-16.1	1.8×10^{3}
OC_1C_{10}-PPV	wet + PMMA	100	4.7×10^{-4}	-13.5	7.2×10^{2}

Table 5: Different electrical responses with respect to different annealing temperatures for OFETs based on MEH-PPV and OC_1C_{10}-PPV grown on SiO_2 with a PMMA buffer layer. Annealing time is always 15 minutes.

5.4.3 Morphological study of PPV films

An AFM analysis on PPV films used as active material in OFETs was performed to complete the device analysis. Figure 61 reports topographical images of MEH-PPV films on various dielectric layers, along with RMS roughness values (images of OC_1C_{10}-PPV do not show differences). It can be observed that morphology does not noticeably change from one to the other. RMS roughness values of the films after annealing were typically around 0.6 nm in MEH PPV (and also 0.6 nm for OC_1C_{10}-PPV).
As previously described (Section 5.4.2.3), annealing active films is extremely important to optimise the OFET behaviours . When PMMA was used as buffer layer, the best electrical characteristics were obtained after annealing the active material for 15 minutes around its glass transition temperature. At higher annealing temperatures a dewetting process of the active materials starts, involving the aforementioned deterioration.

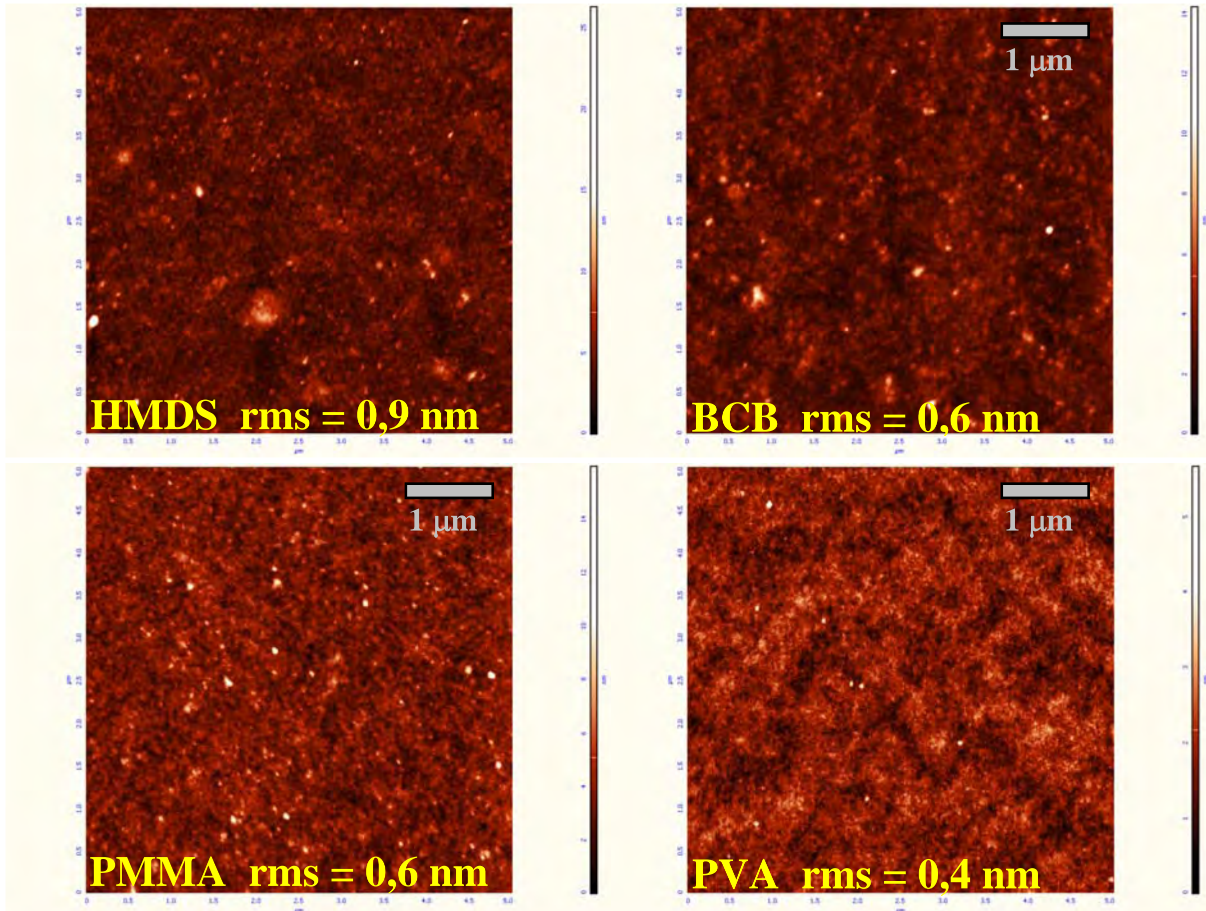

Figure 61: Atomic Force Microscopy (AFM) images of MEH PPV films spin-coated on different dielectric substrates with the corresponding surface RMS roughness. The lateral size is 5 x 5 μm^2. The film deposited on PMMA was annealed at 75°C for 15 minutes; all the others at 100°C for 15 minutes.

In order to directly observe the film dewetting, AFM measurements were performed also on films deposited on PMMA and annealed at a temperature higher than the active material T_g (Figure 62). We observed the formation of spherical clusters and high surface roughness.

On the contrary, no dewetting phenomenon was observed on PVA, BCB and HMDS, even when the annealing time was extended from 15 minutes to 1 hour and the annealing temperature was raised up to 100°C. This is evidence that MEH-PPV and OC_1C_{10}-PPV have less affinity with PMMA. Therefore, the active polymer molecules have lower probability to interact with the dielectric layer at the dielectric/semiconductor interface. Consequently, trap formation is also expected to reduce.

This can explain why devices grown on SiO_2 with a buffer layer of PMMA are more performing than all the others.

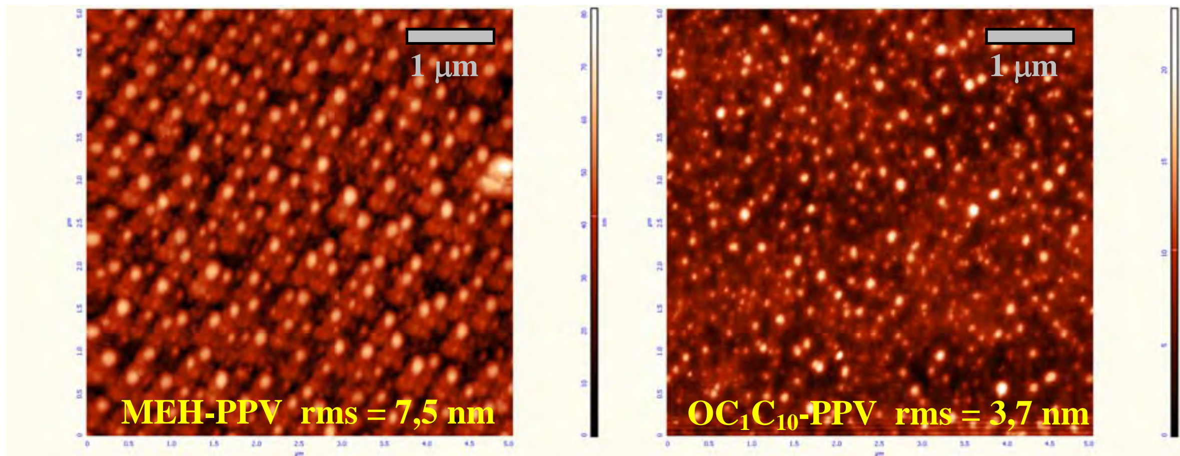

Figure 62: Atomic Force Microscopy (AFM) images of MEH PPV and OC_1C_{10}-PPV films spin-coated on PMMA, annealed at 100°C, with the corresponding surface RMS roughness. The lateral size is 5 x 5 μm^2.

5.4.4 Conclusions on dielectric/PPV interface

A systematic study on the role of the dielectric/organic interface was performed. To control the interface influence, key electrical parameters of polymer-based OFETs were used. Two conjugated polymers, MEH-PPV and OC_1OC_{10}-PPV, were employed and thermal SiO_2 was employed as dielectric layer, either in its pristine state, or chemically treated with OTS and HMDS, or covered with polymeric layers such as PVA, BCB and PMMA.

We have found out that the presence of silanol groups strongly affects the hole transport: the higher their density, the worse the electrical performances. We have also established that the chemical environment matters as well. In particular, –OH groups present in PVA molecules are less deleterious to the hole transport than the silanol ones. The best performances were found in PMMA, which does not have –OH groups in its chemical structure and which shows the lowest affinity with the active polymeric layers[17]. We underlined that, reducing the dielectric/organic interaction, the output curves present a reduced current hysteresis.

Hole mobility values in PMMA, HMDS and BCB are the highest values reported in literature to date (it has to be considered that even if the curves present similar current values, the mobility can be different because it depends also on the dielectric capacitance; additionally variations of the threshold voltages can affect the current values at similar biasing conditions). These high mobility values are also associated with other important electrical features such as low threshold voltage and current hysteresis, high on/off ratio and good saturation characteristics.

We also observed that the threshold voltage values do not follow a common trend like the μ ones, and their variation could be related both to charge injection barriers and to the deep trap presence in the semiconducting polymer films. Furthermore, we observed higher

threshold voltages in the cases of SiO_2 treated OC_1C_{10}-PPV based OFETs, with respect to the MEH-PPV ones. This is probably connected to a lower chemical purity of the former material with respect to the latter (Section 5.4.1). In fact, in presence of deep traps in the active materials[18] (for instance, different chemical species) the injection of mobile charges would only be possible after the filling of deep traps. So the active material purification was confirmed to be fundamental to improve the device performances and reliability.

Finally, we noted that the behaviour of current hysteresis in both active materials presents some anomalies. Device performances decay after a certain number of measurements, in particular current hysteresis highly increases without any recovery even if it is left unbiased for a long time[19]. We assigned this *stress* to a damage of the active material interfacial layers in contact with the dielectric (the zone responsible for conduction), probably due to current flow, which involves a local heating. Again, different chemical interfaces in contact with the active conduction zone could give different damage levels. PMMA gives lower hysteresis, probably as a consequence of the weaker interaction between the semiconducting and dielectric polymers. This weak interaction was confirmed, as already mentioned before, by the dewetting of the active polymer, associated to a large increase in the film RMS roughness if the annealing temperature is increased.

5.5 Dielectric/OS interface in DHCO-4T based OFETs

In this section the study of the dielectric/OS interface through the analysis of the performances of a small molecule based OFET (α,ω-dihexylcarbonylquaterthiophene, named DHCO-4T) is reported. SiO_2 is used as dielectric, either in its pristine state, or chemically treated with OTS and HMDS, or covered with a buffer layer of PVA or PMMA.
A morphological study of the early stages of film growth on some of these substrates is also performed.

5.5.1 *α,ω-dihexylcarbonylquaterthiophene [DHCO-4T]*

α,ω-dihexylcarbonylquaterthiophene (named DHCO-4T, Figure 63) belongs to a novel molecular class synthesized at the *Department of Chemistry and Materials Research Center* of the Northwestern University by Prof. T.J. Marks and Dr. A. Facchetti group[20].

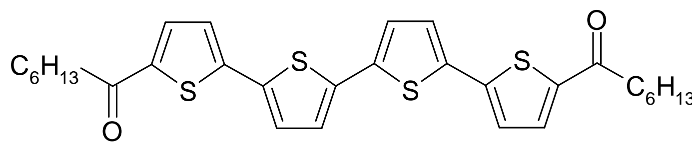

Figure 63: Chemical structure of the DHCO-4T.

The design of this class of molecules starts from the selection of the quarterthiopene core, since it exhibits one of the greatest and most reproducible OFET mobility in the whole oligothiopene family.
Carbonyl electron-withdrawing group (EWD) was introduced in the molecular structure, in an attempt to combine electron and hole transport, and not only hole transport as is typical for oligothiopene.
Carbonyl functionalization was chosen because it allows additional modifications and it can be readily incorporated into π-conjugated core, in contrast with other EWD groups (e.g. –CN, $–NO_2$)
HOMO and LUMO energies in this molecule are respectively estimated as -6,38 eV and -3,78 eV. In principle, this molecule possesses low-lying LUMO that allows and facilitates electron injection and transport as well as hole transport compatible HOMO energy. It was shown that DHCO-4T presents an intrinsic ambipolar character. DHCO-4T based OFETs exhibit field-effect mobility values of the order of 10^{-1} cm^2 V/s for holes and of 10^{-3} cm^2 V/s for electrons. It is currently one of the few small molecules showing high-mobility ambipolarity in

OFETs[19]. Furthermore, it has to be considered that DHCO-4T is also luminescent, with a measured photo-luminescence quantum yield in thin film of about 5%. The main drawback of this compound, when employed as active material in a field effect transistor, is high air sensitivity, which induces a significant lowering of the electrical transport properties when working in air.

In our work, α,ω-dihexylcarbonylquaterthiophene films for OFETs were grown by sublimation in high vacuum, at a base pressure of 5 x 10^{-7} mbar and at a temperature of 240°C in a locally constructed chamber which was directly connected to a nitrogen glove-box to prevent air exposure (Section 4.5.1). Each film had a nominal thickness of 20 nm as measured with a quartz microbalance. Substrate temperature during growth was 90°C and the growth rate was fixed at 0.1-0.2 Å/s (0.6-1.2 nm/min). Device geometry factors were the following: channel width (W) = 10^3 μm, channel length (L) = 150, 300 or 600 μm.

A basic study of the optical properties (absorption and photoluminescence) of this new small molecule was also carried out (Figure 64).

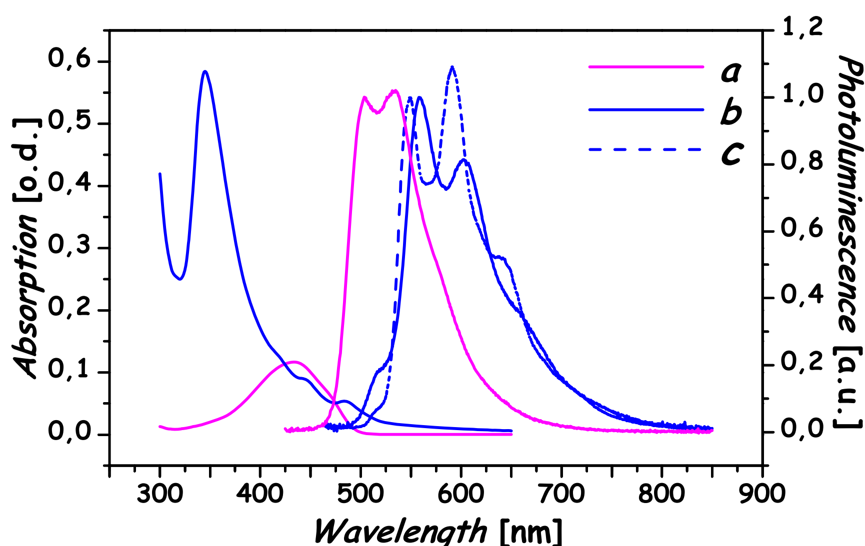

Figure 64: Absorption and photoluminescence (PL) spectra of DHCO-4T molecule in a dichloromethane solution (a) and in a 100 nm film, at room temperature (b) and 20 K (c).

5.5.2 *Electrical characteristics of DHCO-4T based OFETs*

This section aims at understanding how DHCO-4T opto-electronic response varies with the selection of the gate dielectric. BG-TC geometry and 50 nm thick Au source-drain contacts were again used in all devices. The dielectric species used were: pristine SiO_2, wet cleaned SiO_2(Section 5.1.1), OTS or HMDS chemically treated SiO_2 (Section 5.2), and SiO_2 coated with a buffer layer of PVA or PMMA (Section 5.3).

In our experiments, low and unstable drain-source current was measured when operating devices fabricated on bare SiO_2. As expected, the SiO_2 surface is rich in traps and profoundly affects the transport properties for both charge carriers [20]. Performances are very poor also in the OTS treated SiO_2 surface (Table 6). OTS treatment is probably not optimized (Section 5.4.2.2) and there is some interaction between OTS and DHCO-4T that introduces charge carriers traps and consequently affects the OFET performances.

Dielectric Layer	μ p-type (cm^2/Vs)	μ n-type (cm^2/Vs)	V_{th} p-type (V)	V_{th} n-type (V)
Bare SiO_2	----	-----	-----	-----
OTS	1×10^{-6}	10^{-6}	-55	65
HMDS	8×10^{-3}	0.1	-60	53
PVA	6×10^{-4}	0.5	-22	40
PMMA	3×10^{-3}	0.15	-46	63

Table 6: Electron and hole field-effect mobility (μ) data as a function of the SiO_2 surface treatment. The threshold voltage (V_t) values for electron and hole transport are also reported.

The electrical behaviour of the HMDS and PVA based devices is in agreement with results previously reported in literature[21]. Comparing our results of HMDS and PVA based devices, it is clear that electron μ is enhanced by a factor 5 and electron V_t is reduced when the latter dielectric is used. However, the hole μ is reduced by an order of magnitude and the hole V_t is reduced by about 40 V. In conclusion, hole/electron ratio in PVA is very unbalanced with electrons predominating.

An improvement in the electrical characteristics was obtained using PMMA to treat the SiO_2 surface. The current hysteresis is clearly reduced with respect to the HMDS case (Figure 71) and the hole and electron mobility values are substantially unvaried (and consequently the holes/electrons ratio). However, variations in the threshold voltage values guarantee a better balance of the hole/electron ratio in the ambipolar region (V_{DS} = 2 V_{GS}).

The ambipolar behaviour of the DHCO-4T is well shown on the saturation transfer curves (Figure 65). These are transfer curves (Section 3.2.2) obtained keeping fix V_{ds} at higher values than V_g, in order to work exclusively in saturation regime. The only difference between the plots is in the SiO_2 surface treatment: a) treatment with HMDS; b) spin-coating of a PVA layer; c) spin-coating of a PMMA layer. I_{ds} are characterized by a central minimum with a monotonic current increase in the left and right bias regions around it, a clear signature of ambipolarity. Roughly, we can assign the left part of the transfer curves to hole transport,

the right part to electron transport, and the central region to the simultaneous coexistence of holes and electrons in the active zone.

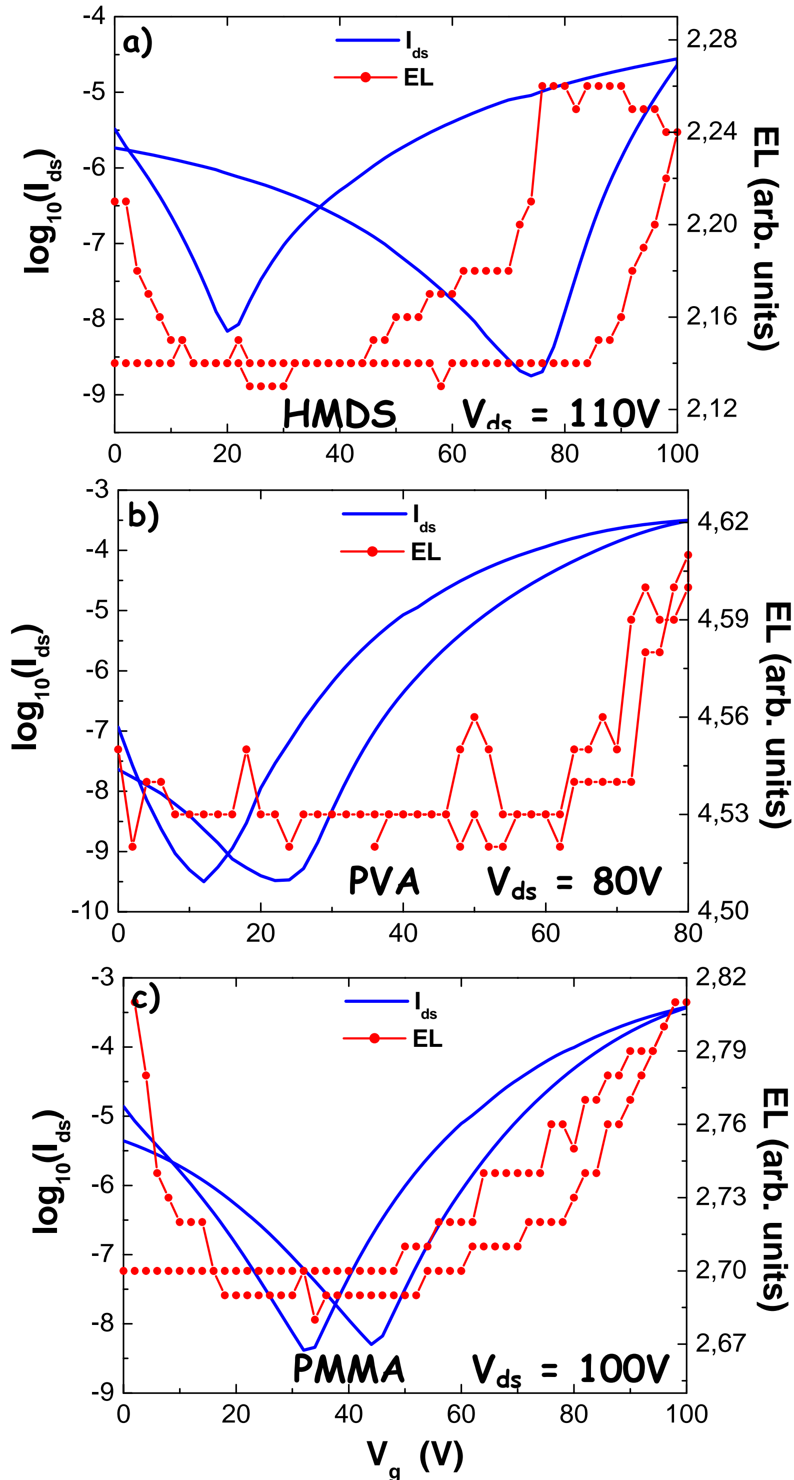

Figure 65: Transfer characteristics and corresponding electroluminescence (EL) of DHCO-4T based OFETs fabricated by treating the SiO_2 gate dielectric surface with: a) HMDS, b) PVA, c) PMMA.

The latter situation is fundamental for efficient radiative recombination between holes and electrons, thus to obtain not only an ambipolar OFET but also light generating electronic

device (*light emitting transistor*, Section 7.1.1). Because of this and of the relatively high solid state emission quantum yield of the DHCO-4T (Section 5.5.1), we collected the corresponding electro-luminescence (EL) signal together with I_{ds}, measuring them during OFET operation (Figure 65).

The absence of an EL signal around the minimum of the transfer plots can be ascribed to the low values of I_{ds} in this region. The hole/electron carrier density ratio present in the ambipolar current is not only related to μ values, but also to V_t values of each charge carrier. The principal limitations to efficient ambipolar transport in devices based on DHCO-4T small molecules are large V_t values (Table 6). In optimum cases, hole μ is three orders of magnitude lower than the electron one (Table 6). This implies that exciton formation is dominated by holes, so that light emission is hole-limited. In spite of this, a μ of $\sim 10^{-3}$ cm^2 V/s should afford a clearly detectable EL signal[22]. On the other hand, high V_t values drastically compress the bias regime where the active channel is open for both electrons and holes. This restricts photon formation to relatively low V_g values and to the saturation condition ($V_g = V_{ds}$). The intermediate zone remains therefore nearly inactive.

These high threshold voltages could depend on several factors:[17] on morphology (it has been demonstrated that grain boundaries and changes in molecular organization at the microscopic scale can create a distribution of spurious electronic states[23-25], Section 3.2.2.1); on the metal contact-semiconductor interface; on the material composition of the dielectric and of the semiconductor (at the dielectric/OS interface energy levels acting as charge traps can exist, and they have to be filled before I_{ds} can flow: this increases V_t, Section 3.3.2.2).

In DHCO-4T, the role of the chemical interaction between the OS and the dielectric layers in determining the V_t needed to open the transport channel is not particularly relevant. Clearly, changing the dielectric surface composition principally affects μ (Table 6), which varies over three orders of magnitude. Differences in V_t as a function of the substrate treatment can be rather large, specifically in the PVA case. We can therefore conclude that the chemical species present at the dielectric-semiconductor interface are not the principal cause for V_t variations.

To better understand these points, we decided to study the DHCO-4T early stages of growth onto different substrates (Section 5.5.3).

Also using DHCO-4T small molecules we observed the phenomenon of *stress,* that involves hysterisis increase and electrical performance lowering. Differently from PPV cases, the initial performance characteristics can be partially recovered after leaving the transistor unbiased for a certain period of time. Part of the deterioration is however irreversible.

5.5.3 Early stages of DHCO-4T film growth

The electric response of DHCO-4T devices varies with the selection of the gate dielectric as well as with the OS film growth conditions. Concerning the morphology of the DHCO4T-dielectric layer interface, where charge transport occurs, we have analysed the early stages of DHCO-4T growth by AFM. Our measurements reveal an initial layer-by-layer growth mechanism with a high density of nucleation centres (Figure 66). This is substantially independent from the various SiO_2 treatments employed. The height distribution of the DHCO-4T islands is peaked around a characteristic value of 3 nm. This bi-dimensional growth affords good film connectivity, which is essential for good charge transport. We can therefore reasonably conclude that lowering V_t requires optimising the metal-organic interface (an issue that will be discussed in Section 6.2).

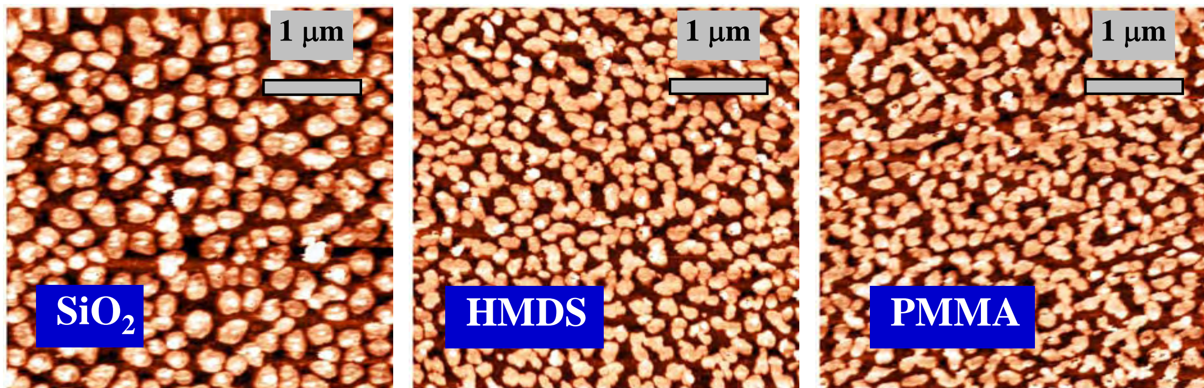

Figure 66: Atomic Force Microscopy (AFM) images of the early growth stages of DHCO-4T films sublimed on: a) bare SiO_2; b) HMDS treated SiO_2; c) SiO_2 with a buffer layer of PMMA.

5.5.4 Conclusions on dielectric/DHCO-4T interface

A systematic study of the role of the dielectric/organic interface in OFET devices based on the novel ambipolar α,ω-dihexylcarbonylquaterthiophene (DHCO-4T) molecule was reported. Thermal SiO_2 was employed as dielectric layer, either in its pristine state, or chemically treated with OTS and HMDS, or covered with polymeric layers such as PVA and PMMA.

Our results demonstrate that DHCO-4T hole and electron mobility and I_{ds}-V_{ds} hysteresis mainly depend on the composition of the dielectric material employed. With respect to previously reported works, improvements in the electrical performance of the device have been achieved by using PMMA coated SiO_2 as dielectric layer. In particular, in comparison to the best results reported before (HMDS case), current hysteresis is clearly reduced with hole and electron mobility remaining substantially unvaried[26].

Beyond the ambipolar behaviour, electroluminescence was also successfully observed in DHCO-4T based OFETs, in correspondence with the unipolar transport in the active channel. The principal limitations to the opto-electronic performances are the high gate threshold voltage values, measured for both electrons and holes.

The initial stages of DHCO-4T film growth were studied by AFM, revealing a layer-by-layer growth mechanism with a high nucleation density that gives rise to the formation of a continuous and homogeneous transport layer. Studying the morphology of the first DHCO-4T layers onto different substrates we always observed good film connectivity, which is essential for good charge transport. These information indicate that high threshold voltage values are neither related to the dielectric nature nor to a detrimental growth of the early stages of the film. Thus, the metal-semiconductor interface is probably the most relevant parameter determining the gate threshold voltage (Section 6.2).

5.6 Dielectric/OS interface in T3

In this section we report on the dielectric/OS interface formed using semiconducting small molecules based on benzene rings arranged in the typical fluorenes structure: ter(9,9-diarylfluorene), named T3. T3 belong to a widely studied class of OS: the oligofluorens.

This study was performed through a morphological analysis of T3 thin films onto different dielectric substrates: HMDS chemically treated SiO_2, or SiO_2 covered with a buffer layer of BCB or PMMA.

Some preliminary results of the field-effect characteristics of a T3 based OFET are also reported.

5.6.1 Ter(9,9-diarylfluorene) [T3]

This particular ter(9,9-diarilfluorene) (T3, Figure 67) belongs to a class of 9,9-diarilfluorenes which was synthesized at the *Department of Chemistry* of the National Taiwan University from Dr. Ken-Tsung Wong[27]. This compound contains intrinsically stronger carbon sp^3-sp^2 bonds between the pendant aryl groups and the carbon of fluorene and exhibits excellent morphological and thermal stability. This small molecule also present high blue emission quantum yield in thin film.

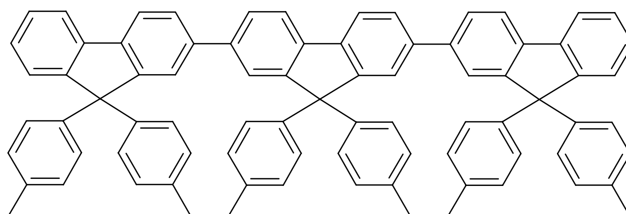

Figure 67: Chemical structure of the T3.

In previous works, thin films of T3 exhibited unusual ambipolar charge transport in Time Of Flight (TOF, bulk conduction) measurements[28]. Because of its peculiarities, T3 is promising for applications in OLEDs, as an efficient blue emitter.

These characteristics are retained also in air. Therefore, purely phenyl-based conjugated system, without strong electron-withdrawing groups or electron-accepting heterocyclic rings, shows good electron transport and environmental stability.

In our work, ter(9,9-diarilfluorene) was employed in OFET top contact geometry (Section 5.6.2) and grown by sublimation in high vacuum at a base pressure of 5 x 10^{-7} mbar and at a temperature of 360°C, in a locally constructed chamber which was directly

connected to a nitrogen glove-box to prevent air exposure (Section 4.1.1). Films had a nominal thickness of 30 nm as measured with a quartz microbalance. Substrate temperature during growth was kept at room temperature and the growth rate was fixed at 0.5 Å/s (3.0 nm/min).

5.6.2 Preliminary field-effect characteristics of T3 based OFETs

In this preliminary study, we used as dielectric wet cleaned pristine SiO_2, (Section 5.1.1), and SiO_2 treated with the protocols that gave the best results in the previous cases: HMDS treated SiO_2 (Section 5.2), and SiO_2 coated with a buffer layer of PMMA (Section 5.3).

BG-TC geometry and 50 nm thick Au source-drain contacts were used in all devices. The device geometry factors were the following: channel width (W) = 10^3 µm, channel length (L) =150, 300 and 600 µm.

Unfortunately, the only device showing detectable field-effect conduction is the HMDS treated SiO_2 one (Figure 68). The device exhibits hole transport only, instead of the ambipolar behavior suggested by TOF measurements.

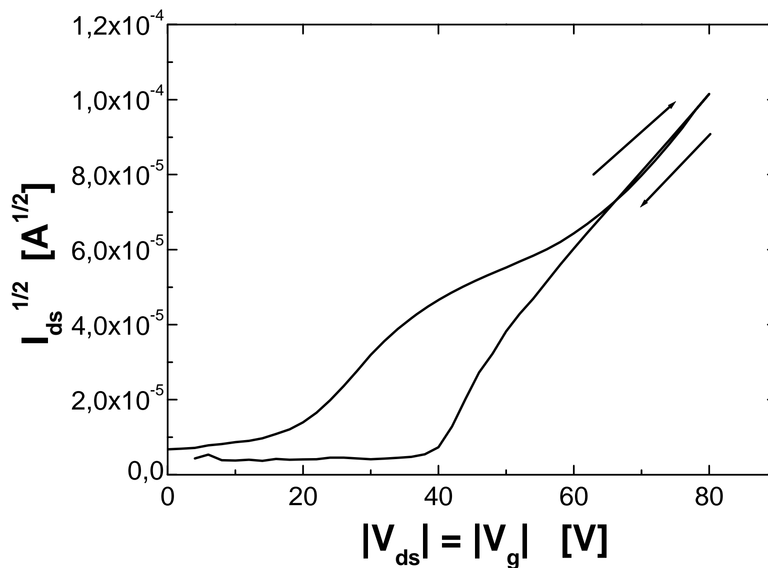

Figure 68: Locus curves for OFETs based on T3 grown onto HMDS treated SiO_2.

The hole mobility value obtained is $\mu = 1.4 \times 10^{-5}$ cm^2 V/s with a threshold voltage of V_t = -30.6 V.

For an easier electron injection (Section 2.5), and to verify the possible electron transport, a similar BG-TC geometry device with 50 nm thick Al source-drain contacts was grown, but we measured very low drain-source current that involves negligible mobility.

5.6.3 Morphological study of T3 thin films

As already observed in DHCO-4T (Section 5.5.2), T3 electrical responses are profoundly dependent on the dielectric/OS interface. Field-effect conduction can be completely hindered depending on the dielectric used. In order to understand if this behaviour is linked to the chemical nature of the dielectric species or to the different films morphologies induced by the different dielectric, a study on T3 thin films was performed. Films with a nominal thickness of 5 and 10 nm grown onto HMDS treated SiO_2 and SiO_2 covered with a buffer layer of PMMA were analyzed. Furthermore, we decided to analyze also thin films grown on SiO_2 covered with BCB, as this is the next substrate which will be employed to build T3 based OFETs.

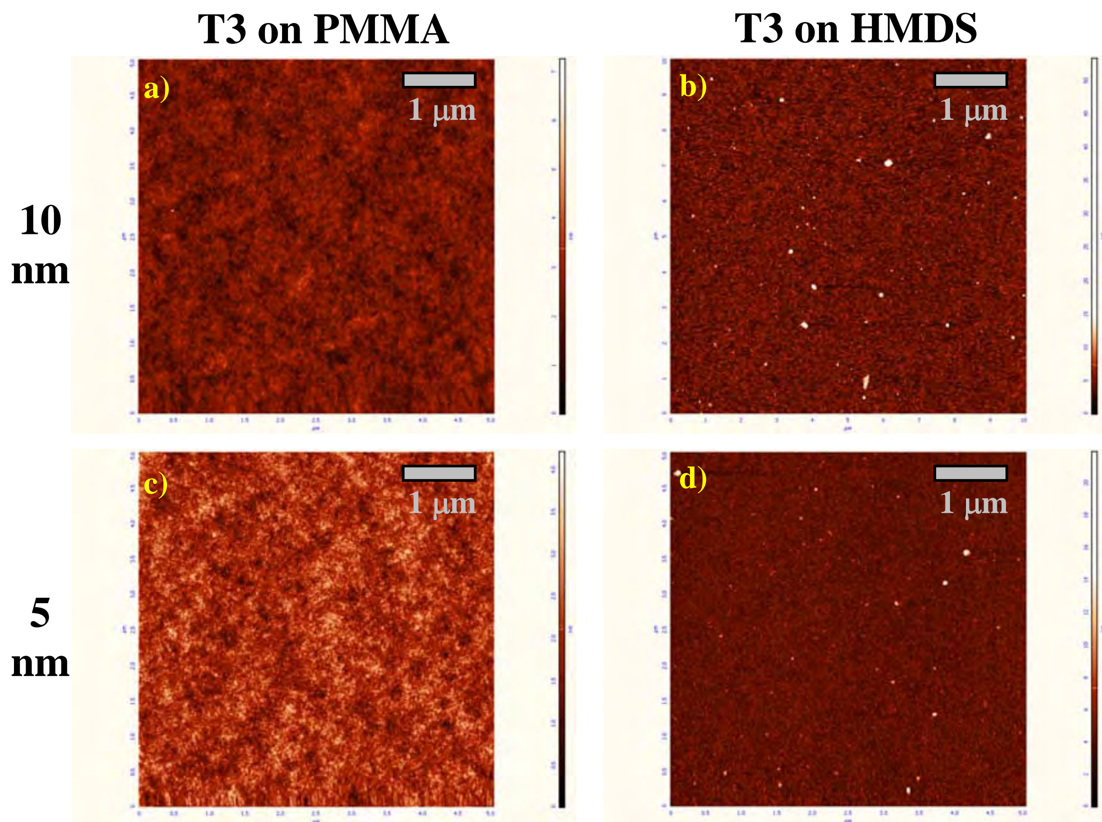

Figure 69: Atomic Force Microscopy (AFM) images of 10 nm (a,b) and 5 nm (c,d) T3 thin films grown on PMMA (a,c) and HMDS (b,d). The lateral size is 5 x 5 μm^2.

We started our analysis from 5 x 5 μm^2 images on PMMA and HMDS (Figure 69). The two films morphologies are very different. T3 is grown on PMMA in a disordered way, following the structure of the polymer dielectric (Figure 50) and it also presents the same roughness (Table 7). On HMDS, we observed small quasi-spherical grains with a diameter of tens of nm (as is better observed in the 1 x 1 μm^2 images, Figure 70 and Figure 71). This structure

suggests a more ordered small molecule packing which can in principle facilitate the field-effect conduction.

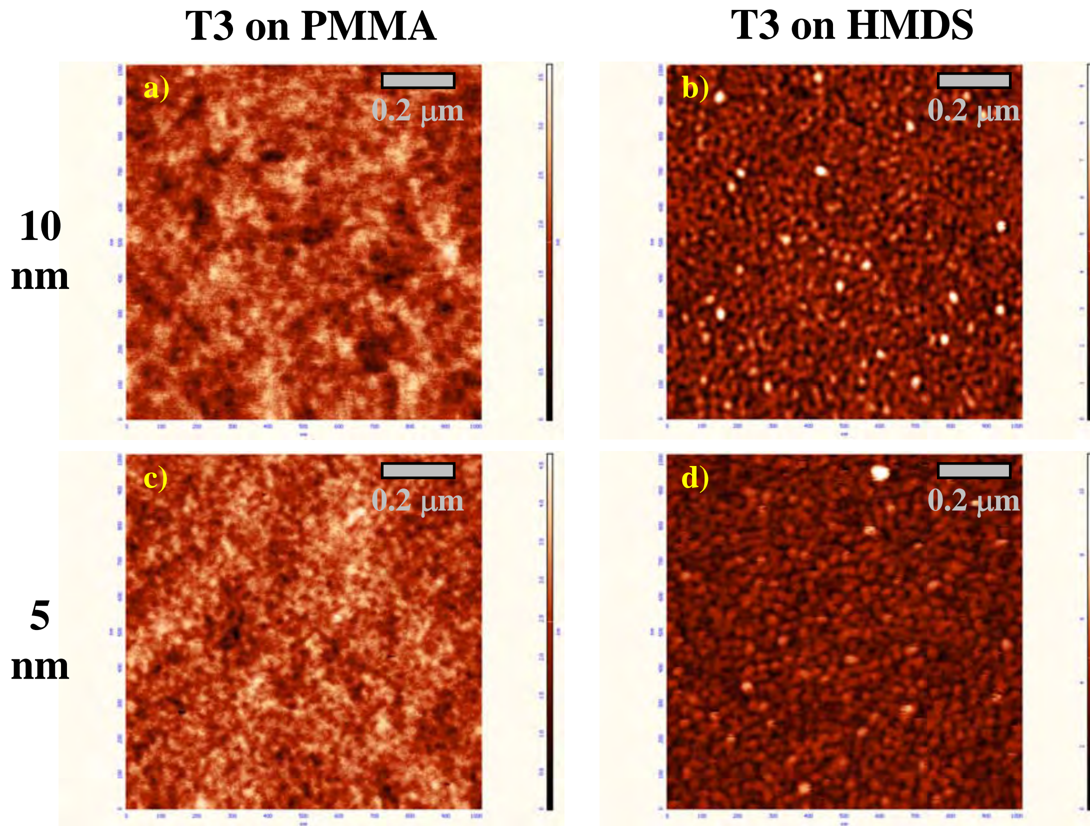

Figure 70: Atomic Force Microscopy (AFM) images of 10 nm (a,b) and 5 nm (c,d) T3 thin films grown on SiO_2: covered with PMMA (a,c) or treated with HMDS (b,d). The lateral size is 1 x 1 μm^2.

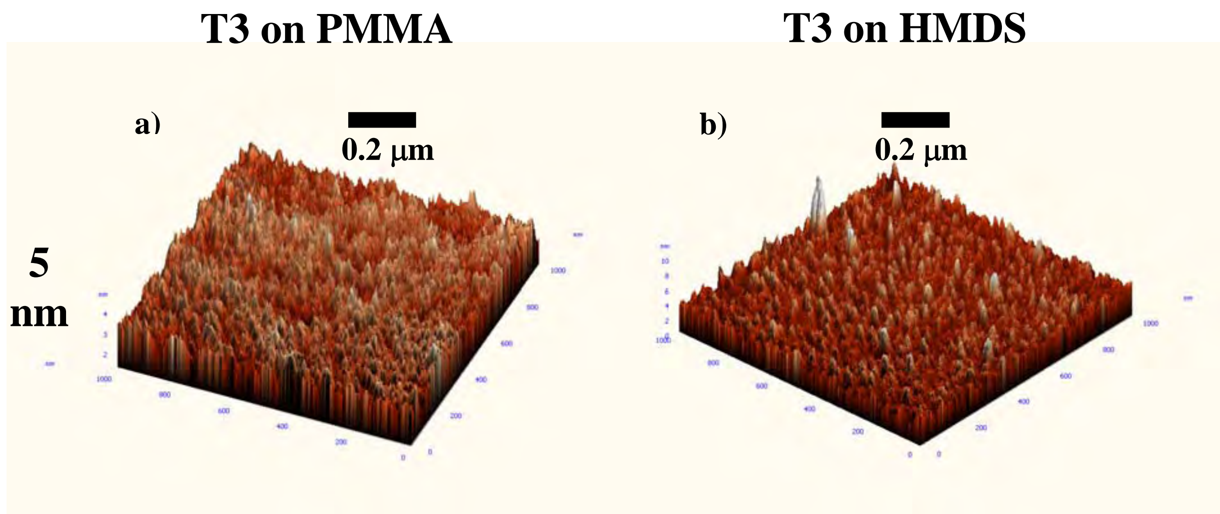

Figure 71: 3-D Atomic Force Microscopy (AFM) images of 5 nm T3 thin films grown on: a) SiO_2 covered with PMMA; b) HMDS treated SiO_2 . The lateral size is 1 x 1 μm^2.

Then we moved to study the growth of T3 onto SiO_2 covered with a BCB buffer layer (Figure 72), in order to have a hint whether this is a good treatment to obtain efficient field effect transistors or not.

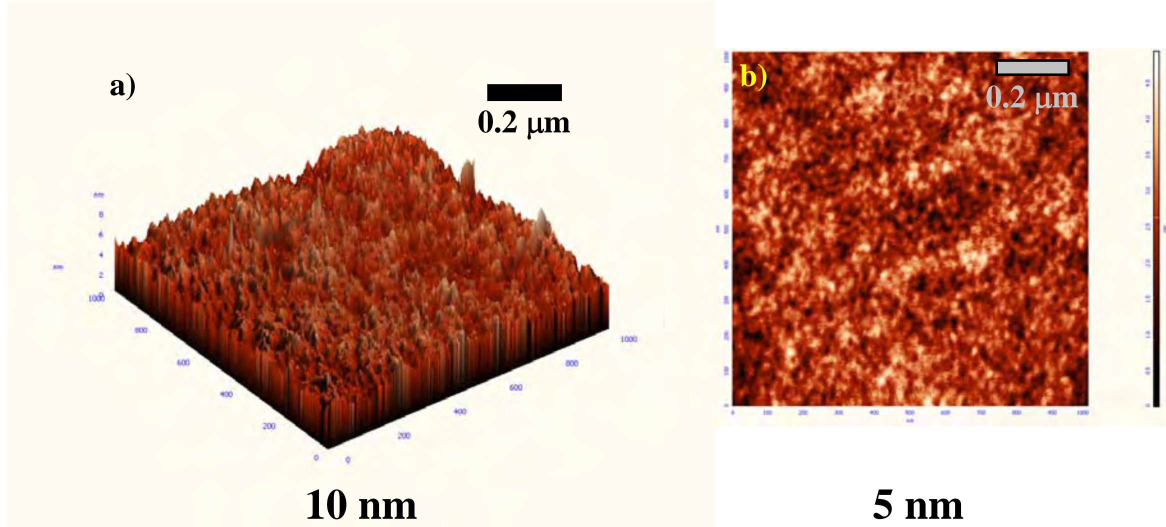

Figure 72: Atomic Force Microscopy (AFM) images of 5 nm T3 thin films grown on SiO_2 covered with PMMA: a) 3-D image of 10 nm thin film; b) 2-D image of 5 nm thin films. The lateral size is 1 x 1 μm^2.

As in the PMMA case, T3 is grown following the BCB morphology, thus giving a disordered structure with a slightly higher roughness (Table 7) than the dielectric one (Figure 52).

Dielectric layer	*Thickness (nm)*	*Roughness (nm)*
wet + HMDS	5	0.66
wet + HMDS	10	0.76
wet + PMMA	5	0.39
wet + PMMA	10	0.38
wet + BCB	5	0.59
wet + BCB	10	0.68

Table 7: Surface roughness of 5 and 10 nm T3 thin films growth on different substrates.

5.6.4 Conclusions on T3

T3 devices based on PMMA dielectric polymer do not exhibit field-effect conduction. This is probably due to the T3 molecules disordered packing on this surface, that is disadvantageous for the OFET operation. It has to be underlined that the roughness does not change if the thickness of the film increases, so we can presume that the molecular packing has the same degree of disorder.

Devices made on HMDS treated SiO_2 showed a detectable field-effect conduction, limited to hole transport. Their morphological structure suggests a more ordered small molecule packing

with respect to the PMMA case, and this can in principle facilitate the field-effect conduction. We observed that, if film thickness increases, roughness also increases. This suggests that the film structure is more ordered in the first layers, where the field-effect conduction happens, than in the rest of the film. A more ordered structure is preferred to achieve better field-effect performances. Unfortunately, transport properties are low and current hysterisis high; the device performances in this configuration are not optimized. In order to have a better performing OFET additional investigation are needed.

Finally, the morphological analysis made on BCB pointed to an OFET behaviour similar to the PMMA one.

References Chapter 5:

[1] P.O. Hahn, M. Grundner, A. Schegg, H. Jakob, *Appl. Surf. Science*, 39, 436, **1989**.

[2] T. Miura, M. Niwano, D. Shoji, N. Miyamoto, *J. of Appl. Phys.*, 79, 4373, **1996**.

[3] G. Trucks, K. Raghavacharai, G.S. Higashi, Y.J. Chabal, *Phys. Rev. Lett.*, 65, 504, **1990**.

[4] T. Takahagi, I. Nagai, A. Ishitani, H. Kuroda, Y. Nagasawa, *J. of Appl. Phys.*, 64, 3516, **1988**.

[5] N. Rozlosnik, M.C. Gerstenberg, N.B. Larsen, *Phys. Rev. Lett.*, 19, 1182, **2003**.

[6] S.H. Jin, J.S. Yu, C.A. Lee, J. Wook, B.G. Park, J.D. Lee, *J. Of the Korean Phys. Soc.*, 44, 181, **2004**.

[7] M. Yoon, C. Kim, A. Facchetti, T.J. Marks, *J. Am. Chem. Soc.*, 128, 12851, **2006**.

[8] http://www.pupman.com/listarchives/1998/April/msg00337.html

[9] H.L. Chen, T.C. Chu, M.Y. Li, F.H. Ko, H.C. Cheng, T.Y. Huang, *j. Vac. Sci. Technol. B*, 16, 2381, **2001**.

[10] L.L Chua, J. Zamuseil, J.F. Chang, E.C.W. Ou, P.K.H. Ho, H. Sirringhaus, R.H. Friend, *Nature*, 434, 194, **2005**.

[11] J. Zaumseil, R. H. Friend, H. Sirringhaus, *Nature Mater.*, 5, 69, **2006**.

[12] C. Tanase, J. Wildeman, P. W. M. Blom, *Adv. Funct. Mater.*, 15, 2011, **2005**.

[13] C. Tanase, J. Wildeman, P. W. M. Blom, M. E. Mena Benito, D. M. De Leeuw, A. J. J. M. Van Breemen, P. T. Herwig, C. H. T. Chlon, J. Sweelssen, H. F. M. Schoo, *J. Appl. Phys.*, 97, 123703-1, **2005**.

[14] A. J. J. M. Van Breemen, P. T. Herwig, C. H. T. Chlon, J. Sweelssen, H. F. M. Schoo, M. E. Mena Benito, D. M. De Leeuw, C. Tanase, J. Wildeman, P. W. M. Blom, *Adv. Funct. Mater.*, 15, 872, **2005**.

[15] M. Jaiswal, R. Menon, *Polymer International*, 55 (12), 1371, **2006**.

[16] P.K.H. Ho, L.L. Chua, M. Dipnakar, X. Gao, D. Qi, A.T.S. Wee, J.F. Chang, R.H. Friend, *Adv.Mater.*, 19, 215, **2007**.

[17] F. Todescato, R. Capelli, F. Dinelli, M. Murgia, N. Campioni, M. Yang, R. Bozio, M. Muccini, *Adv. Funct. Mater.*, submitted.

[18] C.R. Newman, C.D. Frisbie, D.A. da Silva Filho, J.L. Bredas, P.C. Ewbank, K.R. Mann, *Chem. Mater.*, 16, 4436, **2004**.

[19] D. Kawakami, Y. Yasutake , H. Nishizawa ,Y. Majima , *Jpn. J. Appl. Phys. (Part 2)*, 45, L1127, **2006**.

[20] M.H. Yoon, S.A. Di Benedetto, A. Facchetti, T.J. Marks, *J. Am. Chem. Soc.*, 127, 1348, **2005**.

[21] M. H. Yoon, C. Kim, A. Facchetti, T. J. Marks, *J. Am. Chem. Soc.*, 128, 12851, **2006**.

[22] F. Dinelli, R. Capelli, M. A. Loi, M. Murgia, M. Muccini, A. Facchetti, T. J. Marks, *Adv. Mater.*, 18, 1416, **2006**.

[23] R. Capelli, C. Taliani, M. Muccini, *Synth. Met.*, 139, 691, **2003**.

[24] M. Muccini, M. Murgia, F. Biscarini, C. Taliani, *Adv. Mater.*, 13, 355, **2001**.

[25] P. Mei, M. Murgia, C. Taliani, E. Lunedei, M. Muccini, *J. Appl. Phys.*, 88, 5158, **2000**.

[26] R. Capelli, F. Dinelli, S. Toffanin, F. Todescato, M. Murgia, M. Muccini, A. Facchetti, T. J. Marks, *J. Phys. Chem. B*, submitted.

[27] K.T. Wong, Y.Y. Chien, R.T. Chen, C.F. Wang, Y.T. Lin, H.H. Chiang, P.Y. Hsieh, C.C. Wu, C.H. Chou, Y.O. Su, G.H. Lee, S.M. Peng, *J. Am. Chem. Soc.*, 124, 11576, **2002**.

[28] C.C. Wu, T.L. Liu, W.Y. Hung, Y.T. Lin, K.T. Wong, R.T. Chen, Y.M. Chen, Y.Y. Chien, *J. Am. Chem. Soc.*, 125, 3710, **2003**.

Chapter 6:

Semiconductor/metal interface

The properties of the OS/metal interface are studied through the analysis of the electrical performances of PPV and DHCO-4T based OFETs with different metal contacts.
A morphological study of the top contacts was also performed in order to control the possible organic film damaging caused by metal deposition.

6.1 Metals used as injecting electrodes

Drain and source contacts are fundamental to obtain a field effect transistor (Sections 3.1 and 3.2). When working with non-ohmic contacts, a potential barrier is formed, and it leads to poor charge injection[1,3]. This is relevant when field-effect transistors perform in the linear regime because a large part of the source-drain voltage drops at the contacts and not across the channel. Therefore, charge carriers have to be injected by ohmic contacts.
In most cases, these contacts are metallic. Obviously, the choice of the metal is fundamental for a good transistor operation[4] and depends on the active material used. The main parameter considered in selecting the metal is the work function (WF_m).
Generally, the lower WF_m, the easier the electron injection, the higher WF_m, the easier the hole injection[5]. Hence, low work function metals are preferred for n-type materials, and high work function ones for p-type materials.
In this work gold (Au), copper (Cu), silver (Ag), aluminium (Al) and calcium (Ca) were the metals employed to fabricate the drain and source contacts. These metals have to be ultra-pure in order to prevent charge carriers traps presence.
The work function value for each metal is reported in Table 8.

Electrode Metal	Au	Cu	Ag	Al	Ca
WF_m (eV)	5.10	4.65	4.26	4.20	2.87

Table 8: Work function values for metals employed in this thesis as drain and source contacts.

6.2 OS/metal interface in PPV based OFETs

Normally, WF_m and the injection properties are directly related[6,7]. This correlation strongly influences both the threshold voltage and the OS mobility. We decided to analyze the electrical response of OC_1C_{10}-PPV, a classic p-type material, to confirm this behaviour. In this case, better injection is expected from high WF_m metals rather than form low WF_m ones. We started our analysis using SiO_2 covered with a buffer layer of PMMA because this treatment gives the best electrical performance for OC_1C_{10}-PPV.

BG-TC OFETs with gold source and drain contacts have been widely analyzed previously (Section 5.4). Au presents very high work function (WF_m = 5.10 eV), therefore we decided to employ a metal with a lower one: aluminium (Al, WF_m = 4.20 eV).

We measured the p-type conduction properties of OC_1C_{10}-PPV, and we expected the change of metal to cause a deterioration of the performance due to a more difficult charge carrier injection.

Top contacts	*WF_m (eV)*	*μ (cm^2/Vs)*	*V_t (V)*
Au	5.10	1.1×10^{-3}	-18.5
Al	4.20	2.4×10^{-5}	-32.5

Table 9: Hole mobility (μ) and threshold voltage (V_t) data for two different OC_1C_{10}-PPV based OFETs with different metals as top contact electrodes. The active material is spun on SiO_2 covered with a PMMA buffer layer. The electrode thickness is always 50 nm.

As expected (Table 9), electrical performances are worse using Al electrodes than when Au ones are employed. Mobility values decrease of two orders of magnitude and the threshold voltage increases of about a factor 2. The device with aluminum drain and source contacts also presents a higher hysterisis with respect to the one with gold contacts (Figure 73), this is the symptom of a larger charge carrier trap formation during the device operation.

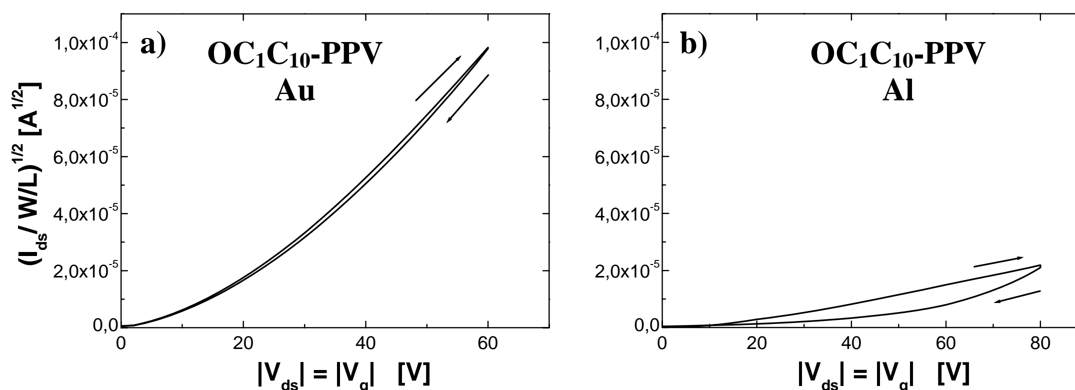

Figure 73: Locus curves: I_{ds} is normalized with respect to the channel width (W) and length (L) for OFETs based on SiO_2 with a polymeric buffer layer of PMMA : a) OC_1C_{10}-PPV with Au drain-source contacts; b) OC_1C_{10}-PPV with Al drain-source contacts. The maximum of the y axis is fixed at 1.1 x 10^{-4} $A^{1/2}$ in order to allow the direct comparison of the I_{ds} currents and of the hysterisis in OFETs with different metal electrodes.

To verify the presence of a good metal/OS interface, we performed a morphological study of the top of the drain and source contacts. In principle, these should be homogeneous and reproduce the organic film morphology (Figure 74.a) if damaging during deposition is avoided.

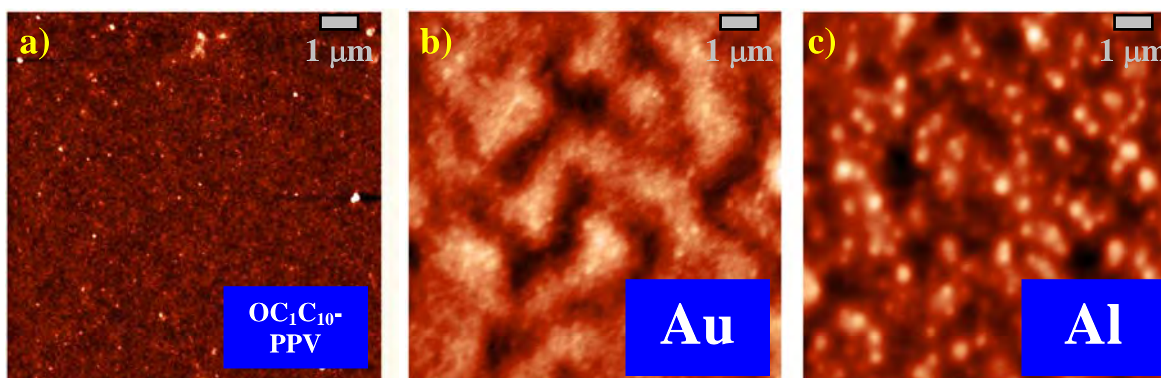

Figure 74: Atomic Force Microscopy (AFM) images of the top electrodes (including film thickness) grown with Au b) and Al c). By comparison an image of the active semiconducting polymer in the middle of the channel is reported, a). The dielectric functionalization layers are SiO_2 covered with PMMA.

Gold forms very small, well interconnected clusters which cover quite uniformly the organic semiconducting polymer. The film morphology is almost preserved (Figure 74.b) and good electrical conduction through the metallic film is achieved.

When aluminium is used, grains formed are bigger than in the case of gold. The film morphology is not preserved (Figure 74.c), but the coverage is sufficiently homogeneous to ensure the electrical conduction through the metallic film.

In both cases, no pinhole or other damage that can be detrimental for the injection are detected. We can suppose that organic semiconductor damaging during the metal deposition is avoided.

From these observations, we can suggest that variations in the electrical characteristics of OFETs with Au or Al source-drain contacts are mainly due to the difference in the metal work function.

In future investigations, to improve the p-type electrical performances of PPV based OFET, we intend to employ metals with higher work function with respect to gold, i.e. platinum (WF_m = 6.10 eV)[8].

6.3 OS/metal interface in DHCO-4T based OFETs

Section 5.5.2 dwells on the electrical response of OFETs based on DHCO-4T small molecules grown on different dielectrics. High V_t values are the principal limitation to the opto-electronic performances for both electrons and holes. The results presented in Section 5.5 enabled us to conclude that neither the chemical species present at the dielectric/semiconductor interface, nor a detrimental growth of the early stages of the film are the main cause of high V_t values.

Another possible cause of these high threshold voltages can reside in a poor injection of the charge carriers from the drain and source contacts. As already described (Section 2.5 and Section 3.3.1) and confirmed with the OC_1C_{10}-PPV case (previous section), normally the energy injection barrier for holes and electrons depend on the work function of the metal (WF_m) which operates as contact. Therefore, we decided to study how different metals used as electrodes influence V_t values and other electrical parameters in BG-TC OFETs based on DHCO-4T.

To verify the presence of a good metal/OS interface, we performed a morphological study of the top of the drain and source contacts. These should reproduce the organic film morphology and the coverage should be homogeneous, if damaging during deposition is avoided.

6.2.1 Electrical response of different metal contacts for DHCO4T based OFETs

Understanding the mechanism of the metal/semiconductor interface formation and the charge injection process is one of the key points in organic electronics technology[9]. In particular, the energetic matching between the metal work function and the organic transport

levels, the HOMO for holes and the LUMO for electrons, is considered crucial to control the device gate threshold voltage.

In our study on the electrical characteristics of DHCO-4T based OFETs (Section 5.5.2), the only metal used to produce the device electrodes was gold. The best results are obtained using HDMS treated SiO_2 or SiO_2 covered with a buffer layer of PMMA as dielectric. Thus, we chose to investigate the metal/OS interface in such devices.

Au is one of the higher work function metal which is used as electrode in OFETs, so we decided to use lower work function metals. The work function of the metals employed in this study ranged between 5.1 (Au) and 2.87 eV (Ca). HOMO and LUMO values of DHCO-4T are estimated to be -5.38 and -3.78 eV, respectively[10]. Therefore, the energy alignment of the HOMO level should be more favourable for high WF_m metals such as Au, whereas the alignment of the LUMO level should be more favourable for low WF_m metals such as Ca.

With regards to threshold voltage, we expected a progressive shift of the hole V_t and the electron V_t towards higher and lower values respectively, when moving from Au to Ca. Consistently, the hole mobility would be expected to decline and the electron mobility to increase when progressing from Au to Ca.

Dielectric Layer	**HMDS**				**PMMA**			
Electrode Metal	Au	Cu	Ag	Ca	Au	Cu	Ag	Ca
WF_m (eV)	5.10	4.65	4.26	2.87	5.10	4.65	4.26	2.87
μ p-type (cm^2/Vs)	$8\ 10^{-3}$	$2\ 10^{-4}$	$8\ 10^{-5}$	----	$3\ 10^{-3}$	-----	$2\ 10^{-3}$	-----
μ n-type (cm^2/Vs)	0.1	$6\ 10^{-4}$	0.2	----	0.15	$4\ 10^{-3}$	0.1	$7\ 10^{-5}$
V_t p-type (V)	-60	-36	-50	----	-46	-----	-50	-----
V_t n-type (V)	53	40	30	----	63	56	55	11

Table 10: Electron and hole field-effect mobility (μ) data together with the corresponding gate threshold voltage (V_t) as a function of the work function (WF_m) of the metal used to make the top contact electrodes. The thickness of the electrodes is always 50 nm.

In devices based on HMDS treated SiO_2, the electron threshold voltage trend is as expected (Table 10): electron injection efficiency increases as WF_m decreases. From very high V_t values of 53 V for the gold electrodes we moved to acceptable values of 30 V for the silver ones. Unfortunately, devices made on HMDS with Ca electrodes did not show detectable field-effect response although the whole deposition process is made in high vacuum and

measurements were taken in a glove-box with controlled atmosphere < 1 ppm O_2 and H_2O. The reason for this behaviour is not clearly understood yet and needs further investigations.

The hole threshold voltage is largely unaffected: that implies that the hole injection is not degraded by the WF_m lowering. An exception is represented by the case of Cu contacts, where the hole V_t is unexpectedly reduced to -36 V. Concerning the mobility, we noted that the variations in hole and electron μ do not parallel trends in the hole and electron V_t values. In particular, a linear trend in μ with V_t is not obeyed.

The same argument is valid for devices based on PMMA covered SiO_2. In this case, the electron V_t lowering is less marked when moving from gold, 63 V, to silver, 55 V. When treated in this way, devices with calcium top electrodes showed detectable field-effect conduction for electrons. The electron V_t calculated for such devices is the lower observed in this study: 11 V. As regards the hole injection, we observed that PMMA devices with copper and calcium drain-source electrodes did not work. The hole threshold voltage is weakly correlated to the WF_m values; indeed for silver contacts (lower WF_m) we had only a little higher V_t than for the gold ones (higher WF_m). Again, the variations of the electron μ do not follow the trend of the electron V_t values. Employing Au contacts, the hole mobility is a little higher (V_t is lower) than using Ag contacts.

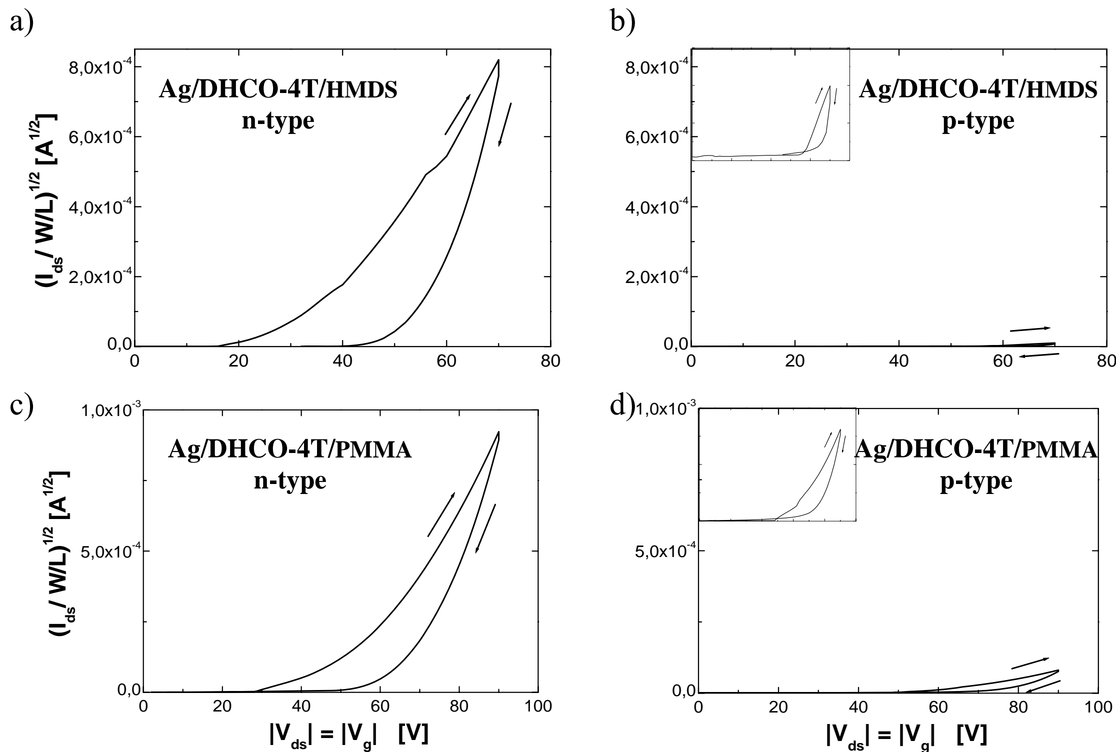

Figure 75: Locus curves of OFETs based on DHCO-4T with Ag electrodes: a) n-type on HMDS treated SiO_2; b) p-type HMDS treated SiO_2; c) n-type on PMMA covered SiO_2; d) p-type on PMMA covered SiO_2. The maximum of the y axis is fixed at 9.0 x 10^{-4} $A^{1/2}$ for HMDS and 1.3 x 10^{-3} $A^{1/2}$ for PMMA in order to allow the direct comparison of the I_{ds} currents. I_{ds} is normalized with respect to the channel width (W) and length (L). Zoom in the b) and d) curves are reported in the respective insets.

We have already observed that hole/electron ratios are very unbalanced with electrons predominating using Au electrodes (Section 5.5.2). This behaviour is preserved also changing the metal of the contacts (Figure 75).
For both DHCO-4T cases, differently from the PPV one, a direct correlation between the injection properties and the WF_m of the electrodes is not observed. A universal trend for all devices is that the largest μ is always obtained with Au electrodes. In addition, the electron V_t decreases when moving from Au to Ca. This indicates that enhanced electron injection is achieved although the electron mobility decreases. The present patterns in OFETs behaviour can be interpreted as follows. The energy gap between the molecular HOMO and LUMO levels and WF_m is not the sole parameter playing a role in the charge injection process. The interfacial morphology between the organic molecules and the metallic atoms of the contact must be taken into account. In order to control this interface we performed a morphological study for Au, Cu and Ag electrodes by AFM measurements.

6.2.2 Morphological study of the different metal contacts on top of DHCO-4T films

A sharp, smooth interface between the semiconductor layer and the metallic electrode is needed to ensure that the charge is injected into molecules with a sufficient number of π-π overlapping nearest neighbours. This situation is required for the charges to reach, via hopping, the device accumulation region located at the semiconductor-dielectric interface. If molecules are not well connected each other, they can be considered "dead" points for charge transport and barriers to charge injection. During metal deposition, the possibility of damage occurring to the DHCO-4T films cannot be completely ruled out. The degree of metal atom penetration into organic semiconductor films may also play a role in these phenomena. To check this problem, we have started an AFM analysis of the top of the electrodes in order to exclude dramatic effects on the morphology of the underlying organic films. If damaging is avoided, the metal should cover homogenously the active material (Figure 76)

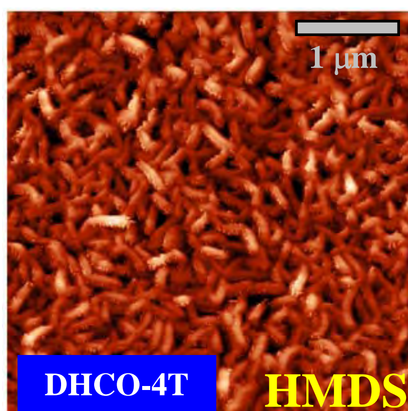

Figure 76: AFM image of the conduction channel for a DHCO-4T based OFET grown on HMDS treated SiO_2.

We performed AFM images of Au, Cu and Ag electrodes (Figure 77). Due to the strong chemical reactivity of Ca with the environment, we could not record any image of Ca electrodes.

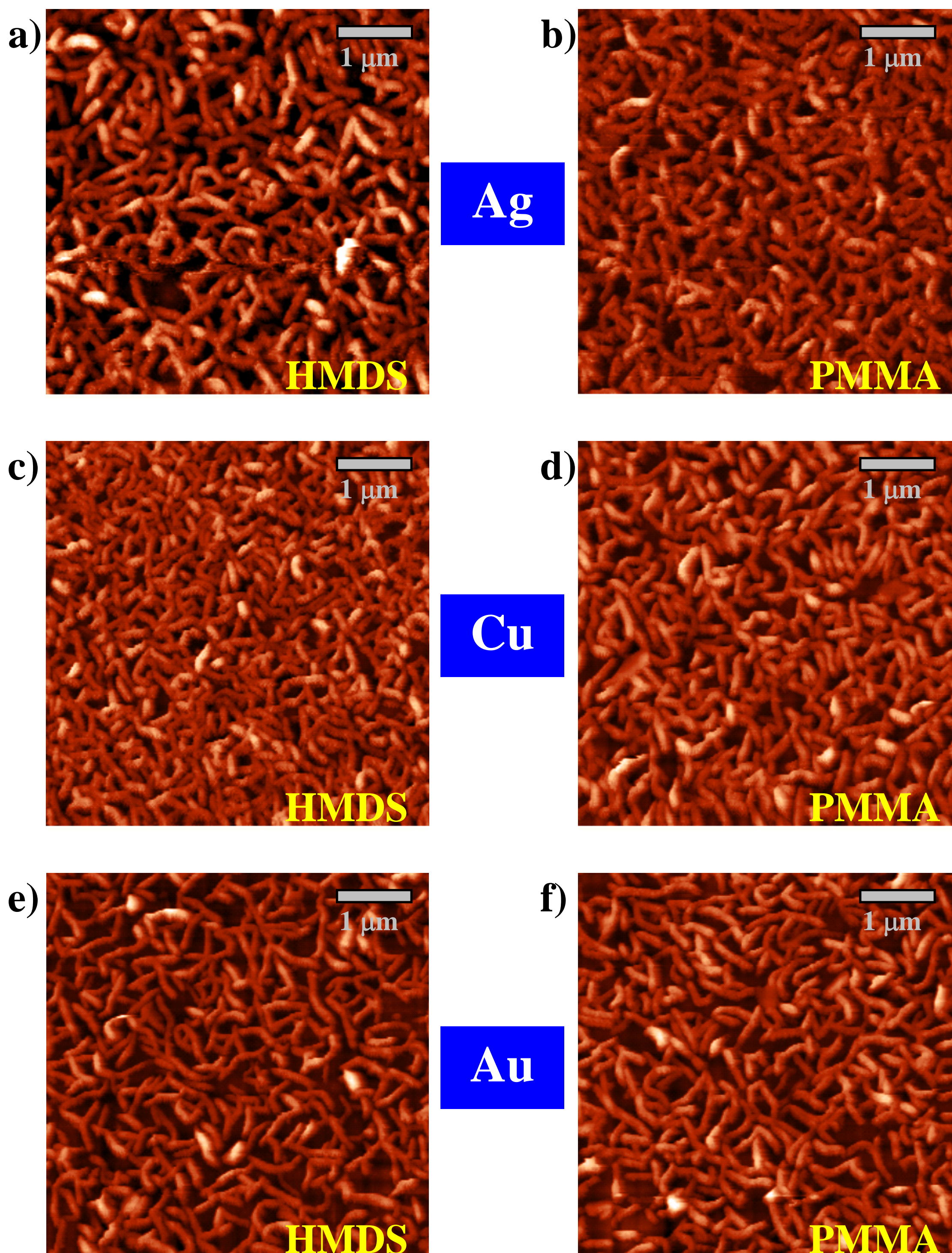

Figure 77: Atomic Force Microscopy (AFM) images of top electrodes (grown on the organic layer) of Ag in a) and b); Cu in c) and d); Au in e) and f). The dielectric functionalization layer is HMDS in a), c), e), and PMMA in b), d), f).

Both for HMDS treated or PMMA covered SiO_2 the growth of silver exhibits the same morphology. Long interconnected wires of metal are formed.
Wires are shorter when copper is used, and this involves less interconnection among them. Anyhow, a packing of these wires ensures the electrical conduction through the metallic film.
The basic organic film morphology is preserved in all growths. No difference is observed between the surfaces of the metallic layers (Figure 77) and the surfaces of the DHCO-4T films in the middle of the active channel (Figure 76). The metallic layers largely cover uniformly the organic semiconductor and no pinhole or other detrimental damage can be detected.
Further investigations are however needed in order to deeply understand what happens at a molecular level during the metal-semiconductor interface fabrication.

6.2.3 Conclusion on metal/DHCO-4T interface

The electrical and morphological data obtained in Section 5.5.2 suggested that the high threshold voltages for both electrons and holes, which are the principal limitation to the performances of OFETs based on α,ω-dihexylcarbonylquaterthiophene, should be ascribed to the metal/organic semiconductor interface.
The electrical measurements of the mobility and threshold voltage values on devices with different drain-source contact metals convinced us that no correlation between the metal work function and the injection efficiency is present for holes. Therefore, for these charge carriers the metal/OS interface is not the most relevant parameter determining the gate threshold voltage.
Differently from holes, the metal/OS interface matters in obtaining low threshold voltage values for electrons. A direct correlation is observed between WF_m and the threshold voltage, the lower the former, the lower the latter. These topics do not correspond to a similar improvement in the electron mobility values. Indeed, for both SiO_2 treatments (HMDS and PMMA) the higher electron μ are measured with gold electrodes.
AFM analysis of the top of the electrodes does not evidence significant changes in the DHCO-4T film morphology when the metals employed are changed.
That being the results, we suggest that the electrical behaviour is likely to be determined by the nanoscale interactions between the DHCO-4T film top surface and the metal layer used as top electrode[11]. A sharp, smooth interface between the semiconductor layer and the metallic electrode is needed to ensure that the charge is injected into molecules with a sufficient number of π-π overlapping nearest neighbours. If the molecules are not well connected to

others, they can be considered “dead” points for charge transport and barriers to charge injection. During metal deposition, the possibility of damage occurring to the DHCO-4T films cannot be completely ruled out. Furthermore, the degree of metal atom penetration into organic semiconductor films may also play a role in these phenomena. These two events can isolate a molecule from its nearest neighbours thereby lowering the molecular interconnection and therefore the mobility.

References Chapter 6:

[1] R. Schroeder, L.A. Majewski, M. Grell, *Appl. Phys. Lett.*, 84, 1004, **2004**.

[2] H. Ishii, K. Sugiyama, E. Ito, K. Seki, *Adv. Mater.*, 11, 605, **1999**.

[3] A. Kahn, N. Koch, W. Gao, *J. of Polymer Phys.*, 41, 2529, **2003**.

[4] P. Stallinga, H.L. Gomes, *Org. Elec.*, 8, 300, **2007**.

[5] S. M. Sze, *Physics of Semiconductor Devices*, 2nd edition,Wiley, New York, **1981**.

[6] W. Mönch, *Surf. Sci.*, 299/300, 928, **1994**.

[7] L. Burgi, T. J. Richards, R. H. Friend, H. Sirringhaus, *J. Appl. Phys.*, 94, 6129, **2003**.

[8] D. Gu, S.K. Dey, *Appl. Phys. Lett.*, 89, 082907, **2006**.

[9] A. Molinari, I. Gutiérrez, I. N. Hulea, S. Russo, A. F. Morpurgo, *Appl. Phys. Lett.*, 90, 212103, **2007**.

[10] M.-H. Yoon, S. A. Di Benedetto, A. Facchetti, T. Marks, *J. Am. Chem. Soc.*, 127, 1348, **2005**.

[11] R. Capelli, F. Dinelli, S. Toffanin, F. Todescato, M. Murgia, M. Muccini, A. Facchetti, T.J. Marks, *J. Phys. Chem. B*, submitted.

Chapter 7:
Future developments

In this section some of the possible future developments of OFET applications are briefly introduced. The possibility to build totally transparent devices as well as to integrate more functionalities in a single device, e.g. field-effect conduction and light emission, are discussed. Doping the active layer of a light emitting transistor with a highly emissive chromophore can be crucial to achieve high emission efficiency. The effect on the charge transport properties of doping the OFET active layer with emissive chromphore is briefly investigated.

7.1 Transparent electronic

As already stressed (Chapter 1), OFETs are technologically attractive because all their layers can be deposited at low temperature and low cost, in a large area and on flexible substrates[1]. Furthermore, light weight, low power consumption and low operating voltages make these devices more attractive for their principle applications as active matrix displays, electronic papers, etc… The availability of optically transparent and mechanically flexible electronic circuits is an essential step to develop next-generation display technologies. Transparency permits to develop displays directly integrated in windows or visors: the "see-through" display technology. Besides, replacing transistors based on the opaque, light-sensitive, amorphous silicon with transparent ones allows each pixel to transmit more light, thus yielding a brighter and more efficient display. Moreover, such transparency allows the use of both top and bottom emission displays.

Studies on this topic started using transparent conductive oxides being both electrically conductive and visually transparent. In 2003, *Nomura* demonstrated the first efficient transparent (optical transmittance > 80% in the wavelength between 390 and 3200 nm) inorganic field-effect transistor[2]. This transistor obviously looses the advantages of the organic ones; therefore, the field of interest moves to the hybrid or total organic transparent transistors.

Wang reported in 2006 a fully transparent hybrid inorganic-organic field-effect transistor, fabricated at room temperature, based on In_2O_3 as active layer, indium tin oxide (ITO) on glass as gate electrode and an organic polymer or a self assembled super-lattice as dielectric[3]. Recently, flexible and partially transparent (optical transmittance of about 40-50%, in the visible region) all-polymer OFET have been reported by Lee[4]. The active channel layer and the electrodes are fabricated using photolithographic patterning of the electrically conducting poly(3,4-ethylenedioxythiopene) (PEDOT) or polypyrrole (PPy). Photocrosslinked poly(vinylcinnamate) (PVCN) or epoxy/methacrylate (epoxy/MMA) polymers were used as the dielectric layer.

Currently, much effort aims at using ITO as gate electrode. ITO films has attracted much attention because of its unique characteristics, such as good electrical conductivity, high optical transparency over the visible wavelength region, excellent adhesion to the substrates, stable chemical property and easy patterning ability. ITO on glass substrate is also widely employed in OLEDs[5]. The real breakthrough would be the employment of ITO on plastic substrates, in order to achieve not only optical transparency but also flexibility. Unfortunately, ITO on such plastic substrates present high roughness that can involve low device performances. A planarization layer has to be introduced, making the device production more difficult. In addition, the ITO growth on plastics is not widely studied as on glass and its manufacturing is more critical.

Extensive academic and industrial efforts have also focused in designing transparent active materials and electrodes. Even now, among potential semiconductor candidates, metal oxides are still the most attractive[6,7]. In confirmation of this *Wang* reported the building of a flexible inorganic/organic hybrid transistor using all-transparent component materials[8].

7.2 Organic light emitting transistors

An organic light emitting transistor (OLET) is a three terminal device that couples the electrical characteristics of an OFET and the emitting characteristics of a OLED[9]. This OFET and OLED combination joins different functionalities in a single device, which is useful for the development of all-organic active matrix display technology and of organic electronics in integrated components and circuits.

OLETs offer an ideal structure for improving the lifetime and efficiency of organic light emitting materials. This is due to the different driving conditions with respect to standard

OLED architectures. Differently to OLEDs, OLETs present a planar geometry and the charge transport occurs in the plane at dielectric/OS interface (field effect charge transport), instead of perpendicularly to the organic layers (classic bulk conduction). Moreover, the electron and hole mobility can be four orders of magnitude higher in OLETs than in OLEDs, with direct consequences on the material lifetime and on exciton emission.

Another clear advantage of OLETs is the potentially higher electroluminescence quantum efficiency. The exciton quenching due to the interaction with metal contacts, the externally applied electric field and to the charge carriers, is drastically reduced. Moreover, the availability of a third electrode to balance currents and move the recombination zone is another obvious advantage.

Organic light-emitting field-effect transistors were first demonstrated using a unipolar p-type transistor[10]. The charge transport and emitting layer was a tetracene polycrystalline film. The observation of light emission from tetracene prove that electrons and holes are simultaneously injected into the active layer. As tetracene films do not sustain a measurable electron current across the channel[11], injected electrons are trapped near the metal/tetracene interface where hole–electron recombination and light emission occur.

For better performing OLETs, ambipolar charge transport is desirable (Figure 78) to maximize the exciton recombination through electron–hole balance, as well as to adjust the position of the recombination region in the channel by tuning the gate voltage[12]. The first ambipolar OLETs were demonstrated using a bulk heterojunction as active component of the device[13], thus extending to OLETs the approach of mixing two materials with complementary properties, previously applied to LEDs[14,15] (Section 1.1) and FETs[16,17]. The active layer of the ambipolar OLET consisted of a vacuum-sublimed bulk heterojunction composed of P13 (N,N′-ditridecylperylene-3,4,9,10-tetracarboxylicdiimide) for electron conduction and T5 (α-quinquethiophene) for hole conduction .

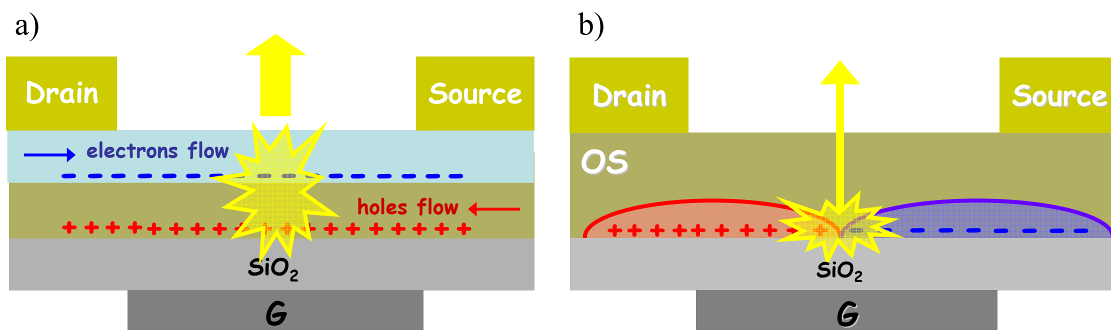

Figure 78: Typical OLET configuration: a) bi-layer structure; b) intrinsic ambipolar material.

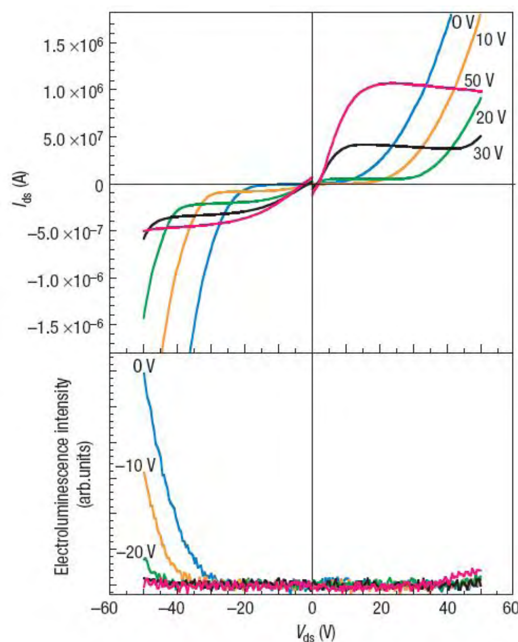

Figure 79: Output curves (top) and electroluminescence intensity (bottom) of an ambipolar OLET[13].

A classic output curve for an ambipolar OFET based on such heterojunction, is reported in Figure 79. The emission is generated in correspondence of the injection of both charge carriers.

Later, an OLET based on a sequential deposition of a p-type (α,ω-dihexyl-quarterthiopene, named DH4T) and a n-type (N,N'-ditridecylperylene-3,4,9,10-tetracarboxylic diimide, named PTCDI-$C_{13}H_{27}$ or P13) materials was demonstrated[18]. The bi-layer configuration (Figure 78.a), has to date, the highest balanced mobility values in ambipolar OLET devices. Unfortunately, the spatial separation between the electron transport layer and the hole transport layer drastically reduces the probability that electrons and holes meet to form excitons inside the device channel. Therefore, an intrinsic ambipolar material would be preferable (Figure 78.b).

Recently, *Zamuseil* demonstrated spatially resolved visible light emission from an ambipolar OC_1C_{10}-PPV based transistor[19]. A low work function metal (Ca) is used for the electron injection electrode and a high work function metal (Au) for the hole injection electrode. BCB dielectric (Section 5.3.3) were used to avoid electron trapping and to enable ambipolar transport[20,21]. The recombination and emission zone can be moved in any position along the channel by varying the applied voltages. At present, the drawback of the ambipolar polymer-based OLETs with respect to the small molecule based ones is the lower charge mobility.

Finally, it has to be underlined that flexible and semi-transparent OLET based on tetracene small molecule have been recently demonstrated by *Santato*[22]. This device is unipolar, is fabricated on a Mylar foil and employs gold electrodes.

7.2.1 Doping of the OFET active layer with chromophores

As described above, PPVs derivatives can be employed as active materials in OLETs. Unfortunately, they exhibit unipolar behaviour with almost all dielectric species and radiative recombination is therefore not optimized. In order to increase the light emission efficiency in opto-electronics devices, in particular in OLEDs, doping the active layer with a light-emitting dye (either fluorescent or phosphorescent) is a common practice. If doping the OFET active layer would not lower the electrical device performances, the doping approach could be a viable route to enhance the exciton recombination and the emission efficiency in optoelectronic field-effect devices. For this reason, we assessed the effect of a dopant dye molecule, dispersed in the semiconducting MEH-PPV and OC_1C_{10}-PPV polymers, on the OFET μ and V_t for our best performing devices[23] (dielectric made of HMDS treated SiO_2, and PMMA).

We selected a commercial iridium complex as dopant: Bis(2-(2'-benzothienyl) pyridinato-N,C3')(acetylacetonate) (btp_2[Ir]acac, purchased from ADS-DYES, Figure 80), which has been successfully employed in OLEDs.

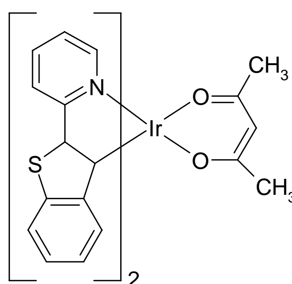

Figure 80: Metal-organic complex used as phosphorescent dye for active materials doping: btp_2[Ir]acac.

We dispersed the iridium complex into the semiconducting polymer solution and then spun the film with the parameters described in Chapter 5. In the MEH-PPV case we doped at 6% in weight, while in the OC_1C_{10}-PPV case we doped at 4% in weight.

Using the HMDS treatment we observed μ of about 9.0 x 10^{-4} cm^2/Vs in both cases, with V_t similar to the undoped ones. The I-V curves for the undoped and doped cases were similar (Figure 81).

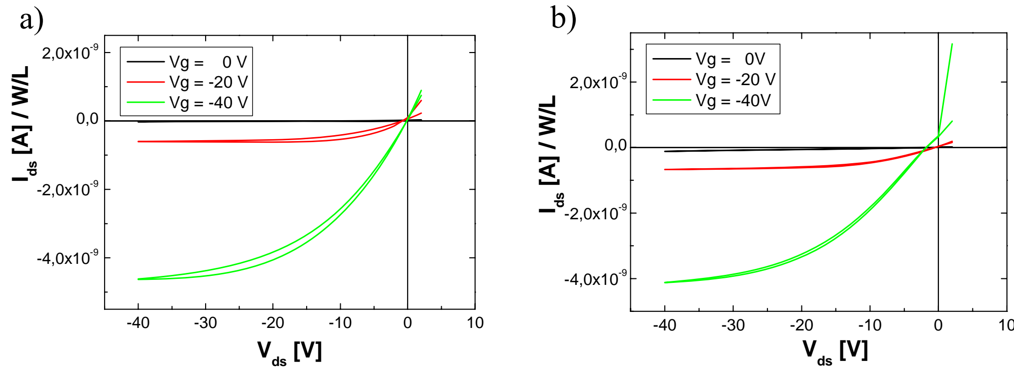

Figure 81: a) I-V curve for OFET based on OC_1C_{10}-PPV with SiO_2 surface treated with HMDS; b) I-V curve for OFET based on OC_1C_{10}-PPV, doped with $btp_2[Ir]acac$ at 4% in weight, and with SiO_2 surface treated with HMDS.

The results with PMMA dielectric films were rather different. For both semiconducting polymers mobility was about 5.0 x 10^{-5} cm^2/Vs (more than one order of magnitude lower with respect to the undoped devices). In this case, the dye is likely to modify the interaction between the dielectric and the active material, thus favouring the creation of traps which make the charge carrier flow more difficult. Notwithstanding, the I-V curves for the undoped and doped cases are still of good quality and similar shape (Figure 82).
A very different behaviour was observed in threshold voltages, which present good values. In MEH-PPV values were around -2.0 V. In OC_1C_{10}-PPV we had values around -4.5 V.

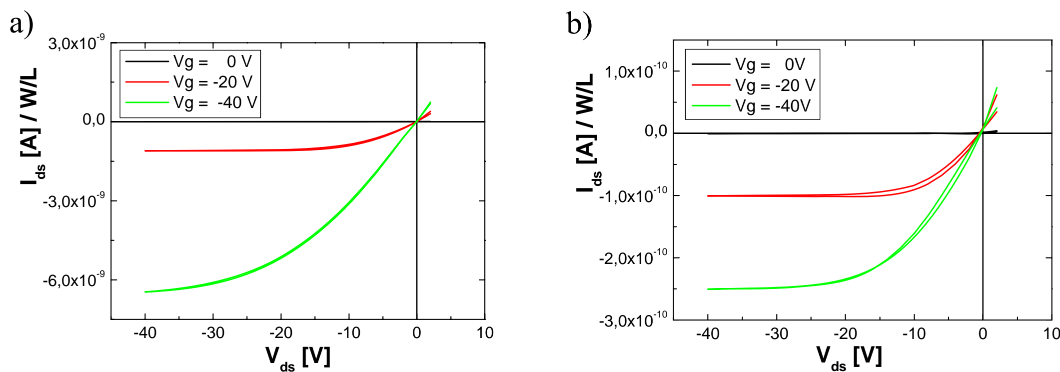

Figure 82: a) I-V curve for MEH-PPV based OFET with SiO_2 covered with PMMA buffer layer; b) I-V curve for OFET based on MEH-PPV, doped with $btp_2[Ir]acac$ at 6% in weight, and with SiO_2 covered with PMMA buffer layer.

We also studied the characteristics of an OFET having OC_1C_{10}-PPV doped at 4% in weight with $btp_2[Ir]acac$ as active layer, and untreated thermally grown SiO_2 as dielectric. The results are quite similar to the undoped case with mobility in the order of 5.0 x 10^{-5} cm^2/Vs and V_t of a few volts.

In summary, we have shown that the dispersion of a phosphorescent dye in the active layer may or may not degrade the device characteristics. It depends on the dielectric layer which is in contact with the active material: in the standard silicon dioxide case or HMDS gas phase treatments we obtained results similar to the undoped cases; using a PMMA dielectric layer the threshold values remain similar to the undoped devices, but mobility decreases of more than one order of magnitude.

References Chapter 7:

[1] S.R. Forrest, *Nature*, 428, 911, **2004**.

[2] K. Nomura, H. Ohta, K. Ueda, T. Kamiya, M. Hirano, H. Hosono, *Science*, 300, 1269, **2003**.

[3] L. Wang, M.H. Yoon, G. Lu, A. Facchetti, T.J. Marks, *Nat. Mater.*, 5, 893, **2006**.

[4] M.S. Lee, H.S. Kang, H.S. Kang, J. Joo, A.J. Epstein, J.Y. Lee, *Thin Solid Films*, 477, 169, **2005**.

[5] *Organic Light-Emitting Materials and Devices*, edited by Zhigang Li, Hong Meng, Taylor and Francis Group, **2006**.

[6] G.J. Exarhos, X.D. Zhou, *Thin Solid Films*, 515, 7025, **2007**.

[7] H. Hosono, *Thin Solid Films*, 515, 6000, **2007**.

[8] L. Wang, M.H. Yoon, A. Facchetti, T.J. Marks, *Adv. Mater.*, 19, 3252, **2007**.

[9] M. Muccini, *Nature Mater.*, 5, 605, **2006**.

[10] A. Hepp, H. Heil, W. Weise, M. Ahles, R. Schmechel, H. von Seggern ., *Phys. Rev. Lett.*, 91, 157406, **2003**.

[11] F. Cicoira, C. Santato, F. Dinelli, M. Murgia, M. A. Loi, F. Biscarini, R. Zamboni, P. Heremans, M. Muccini, *Adv. Funct. Mater.*, 15, 375, **2005**.

[12] M. Freitag, J. Chen, J. Tersoff, J.C. Tsang, Q. Fu, J. Liu, P. Avouris. *Phys. Rev. Lett.*, 93, 076803, **2004**.

[13] C. Rost, S. Karg, W. Riess, M.A.Loi, M. Murgia, M. Muccini, *Appl. Phys. Lett.*, 85, 1613, **2004**.

[14] N. Corcoran, A.C. Arias, J.S. Kim, J.D. MacKenzie, R.H. Friend, *Appl. Phys. Lett.*, 82, 299, **2003**.

[15] M.M Alam, C.J. Tonzola, S.A. Jenekhe, *Macromolecules*, 36, 6577, **2003**.

[16] E.J. Meijer, D.M. de Leeuw, S. Setayesh, E. van Veenendaal, B.H. Huisman, P.W.M. Blom, J.C. Hummelen, U. Scherf, T.M. Klapwijk, *Nature Mater.*, 2, 678, **2003**.

[17] K. Tada, H. Harada, K. Yoshino, *Jpn. J. Appl. Phys.*, 35, L944, **1996**.

[18] F. Dinelli, R. Capelli, M. A. Loi, M. Murgia, M. Muccini, A. Facchetti, T. J. Marks, *Adv. Mater.*, 18, 1416, **2006**.

[19] J. Zaumseil, R.H. Friend, H. Sirringhaus, *Nat. Mater.*, 5, 69, **2006**.

[20] L.L Chua, J. Zamuseil, J.F. Chang, E.C.W. Ou, P.K.H. Ho, H. Sirringhaus, R.H. Friend, *Nature*, 434, 194, **2005**.

[21] T.B. Singh, F. Meghdadi, S. Günes, N. Marjanovic, G. Horowitz, P. Lang, S. Bauer, N. S. Sariciftci, *Adv. Mater.*, 17, 2315, **2005**.

[22] C. Santato, I. Manunza, A. Bonfiglio, F. Cicoria, P. Cosseddu, R. Zamboni, M. Muccini, *Appl. Phys. Lett.*, 86, 141106, **2005**.

[23] F. Todescato, R. Capelli, F. Dinelli, M. Murgia, N. Camaioni, M. Yang and M. Muccini, SPIE 6655, *Organic Light Emitting Materials and Devices XI*, Ed. by Z. H. Kafafi and F. So, **2007**.

Chapter 8:

Conclusions

The work presented in this thesis focuses on the investigation of two interfaces which play a crucial role in the physics of organic electronic devices: the dielectric/organic semiconductor and the organic semiconductor/metal ones.
It is generally accepted that interfaces play a key role in determining the device stability and performance reproducibility. This topic matters especially for OFETs, which can be considered truly interfacial devices. Therefore, we studied the key OFET parameters in order to gain information about the two aforementioned interfaces which are present in such device.

Regarding the dielectric/OS interface, we have deeply investigated the relationship between the SiO_2 cleaning protocol or treatment and the electrical response of OFETs based on two PPV semiconducting polymers (MEH-PPV and OC_1C_{10}-PPV) and on a quarterthiopene derivative small molecule (DHCO-4T). The two polymers have been selected because they are widely used in organic electronics and can be considered as representatives of a wide class of polymer semiconductors, while the DHCO-4T was selected because it belongs to a novel class of non-commercial small molecules based on thiophene rings that exhibits ambipolar charge transport and good photo-luminescence quantum yield in thin film. It is a rare case of a molecular system intrinsically ambipolar.
In the PPVs case, we studied the OFET response to three cleaning protocols (*wet cleaning*, *plasma cleaning* and *HF cleaning*) and two SiO_2 gas phase treatments that lead to the formation of an OTS SAM or to the bonding of HMDS molecules to silanols present on the oxide surface. In addition, the influence of a dielectric polymeric thin film coverage on the silicon dioxide surface (using PVA, PMMA and BCB) was analyzed.
All these efforts aimed at screening the charge carrier traps present in SiO_2 surface that obstruct the electrical transport. The dielectric/OS interface was confirmed to be crucial to obtain good electrical performances in OFETs, and we demonstrated that the silanol groups (–OH) act not only as electron traps, as already known, but also as a hole traps. This finding has never been reported before. We also established that the chemical environment matters as well. In particular, –OH groups present in the PVA molecules are less deleterious to the hole

transport than the silanol groups present at the surface of SiO_2. The best performances were found on PMMA, which does not have any –OH groups in the chemical structure and which shows the lowest affinity with the active polymeric layers. The hole mobility values on PMMA, HMDS and BCB are the highest ones reported in literature to date.

As for DHCO-4T, we analyzed the relevance of OTS and HMDS treatments as well as the effect of PVA and PMMA coverage on the ambipolar transport in OFET that are also light emitting. Our results demonstrate that DHCO-4T hole and electron mobility as I_{ds}-V_{ds} hysteresis mainly depend on the composition of the dielectric material employed. The best electrical performances are reached using a PMMA buffer layer. The principal limitations to the opto-electronic performances are identified in the high gate threshold voltage values, measured for both electrons and holes in all dielectrics.

The dielectric can influence the OFET performances not only because traps are present on its surface, but also because it can drive a preferential growth modality of the active material. Morphological analysis were performed for both PPVs and DHCO-4T films. Neither for PPVs nor for DHCO-4T a relation between film morphology and substrate surface was observed. The early stages of DHCO-4T growth reveal an initial layer-by-layer mechanism. This information, together with the lack of a clear correlation between V_t and the dielectric used, indicates that high V_t values in the case of DHCO-4T OFETs are neither related to the dielectric nature nor to a detrimental growth of the early stages of the film.

We also performed a preliminary study of the dielectric/OS interface for T3, a semiconducting small molecule based on benzene rings arranged in the typical fluorene structure. This molecular system exhibits excellent morphological and thermal stability together with high blue emission quantum yields in thin film and ambipolar charge transport in time of flight measurements. We carried out a morphological analysis of T3 thin films onto different dielectric substrates, HMDS, PMMA and BCB, observing a more ordered molecular packing in the former with respect to PMMA and BCB cases. We also fabricated devices on PMMA and HMDS but, in agreement with the more ordered molecular packing, only the latter exhibits detectable hole field-effect conduction.

Regarding the OS/metal interface, we investigated the electrical performances of PPV and DHCO-4T based OFETs with different metal contacts. Normally, a direct correlation between WF_m and the injection properties exists, the higher the former, the easier the hole injection, more difficult the electron one, and vice versa.

For PPV derivatives, we started our analysis using OC_1C_{10}-PPV based OFETs grown on SiO_2 covered with a buffer layer of PMMA. The PMMA choice is due to the excellent electrical performances obtained with such treatment. Gold electrodes are commonly used for these devices and present very high work function (WF_m = 5.10 eV), therefore, we decided to employ a metal with a lower one: aluminium (Al, WF_m = 4.20 eV). As expected, electrical performances worsen using Al, so we confirmed the expected relation between charge injection and metal work function.
A different behaviour was observed for DHCO-4T. Electrical measurements performed on devices with different drain-source contact metals (Au, Cu, Ag, Ca) points to the fact that no correlation between the metal work function and the injection efficiency is present for holes. Differently, the metal/OS interface matters in obtaining low threshold voltage values for electrons, but like in the previous case no influence was noticed in mobility values.
In addition, a sharp, smooth interface between the semiconductor layer and the metallic electrode and avoidance of damaging during the metal deposition are needed to ensure a good charge injection. To control these features, morphological analysis of the top contacts were carried out for DHCO-4T. For all metals, no significant change in the film morphology was observed and no film damaging occurred.
We can assert that the different OFET electrical characteristics observed in the PPV case with Au or Al electrodes are mainly due to the difference in the metal work function, whereas in DHCO-4T WF_m is not the sole parameter playing a role in the charge injection process, and that determines the observed high threshold voltage values. We suggest that the electrical behaviour is likely to be determined by the nanoscale interactions between the DHCO-4T film top surface and the metal layer used as top electrode. The interfacial morphology between the organic molecules and the metallic atoms of the contact must be taken into account. If the molecules are not well connected to others, they can be considered *dead* points for charge transport and barriers to charge injection. During metal deposition, the possibility of damage or metal penetration occurring to the DHCO-4T films cannot be completely ruled out and this can strongly influence especially the mobility. The charge can be injected in *isolated* molecules and therefore the transport is lowered.

In conclusion, interfaces formed by different materials are intrinsically important. Organic based devices are composed by many different interfaces and OFETs in particular are considered *true interface* devices. The comprehension of the physics behind each interface is a crucial point to design new materials for device applications or to improve the performances

of the existing ones. Each interface influences the properties of a system in many different ways and further investigations are needed to understand in full depth the direct correlations. It would be important, rather than considering an interface as a couple of two individual materials that it would be investigated as a single entity with unique features.

Appendix:

Helicens

Helicens are very interesting helical-shaped aromatic systems, and they present great potential for developing new materials with optoelectronic properties. The helicens we studied are the tetrathia[7]helicene[1-3] (Figure A1) named 7-th and its derivatives. They are synthesized at the *Dipartimento di Chimica Organica e Industriale*, at Milan University by the group of Prof. S. Maiorana.

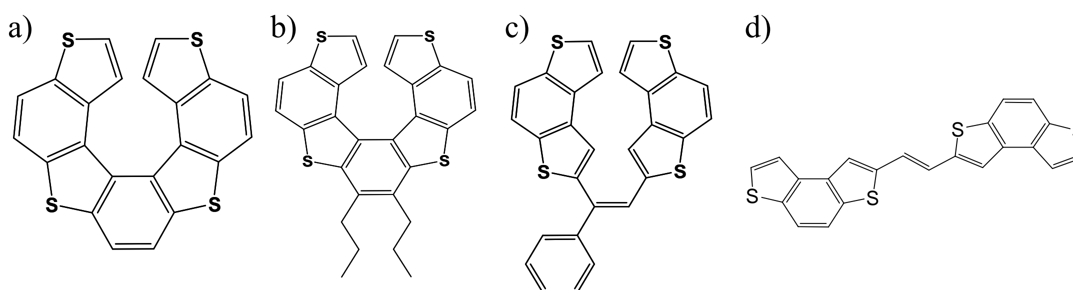

Figure A1: Chemical structure of 7-th (a), 7th-C3 (b), ALK-Ph (c) and MB02 (d).

Compound 7-th was selected among the various heterohelicens because it presents the alternation of thiopene and benzene rings. The presence of heterocycles rings may allow regioselective functionalization of the terminal thiopene rings in an easy and versatile way[3] thereby allowing the tuning of specific properties by introduction of different functional groups.

In this thesis we investigated compound 7-th (Figure A1.a); its alchil-derivative: 7,8-dipropyl-tetratia-[7]-helicene, named 7th-C3 (Figure A1.b); a phenyl derivative: (Z)-1,2-bis-(benzo-[1,2-b;4,3-b']-dithiophen-2yl)-styrene, named ALK-Ph (Figure A1.c); and the 7-th precursor: 1,2-dibenzoditiofene-etene, named MB02 (Figure A1.d).

We carried out a morphological study of these compounds grown on different dielectric substrates, via AFM measurements, in order to understand how the insulator influences the organic growth modality and to check whether OFET devices can be obtained with these molecules.

The work is performed in collaboration with the Prof. T.J. Marks and Dr. A. Facchetti group at the *Department of Chemistry and the Materials Research Center* of Northwestern University.

Morphological study of helicens

The morphology of vacuum sublimed thin films of 7-th, 7th-C3, ALK-Ph and MB02 compounds is investigated by semi-contact AFM measurements. Thin films are grown, both at RT and at 90°C, on different Si-based substrates by keeping the nominal film thickness constant at 50 nm. These growth conditions are chosen because the film morphology is strongly influenced by the substrate nature and temperature during growth, even in relatively thick films.

In particular, thin films of these compounds are studied on pristine Si with thermally grown SiO_2 on top and HMDS treated SiO_2 (typical substrates used in OFETs).

The morphology of 7-th does not show remarkable differences when different substrates are used at RT: elongated needle-like structures are invariably observed (Figures A2.a and A3.a). These structures are interesting because they indicate a possible self-organization of the material with a Volmer-Weber growth modality. The only slight difference is in the SiO_2/HMDS case (Figure A3.a), where anisotropic structures are a little bit more oriented with respect to the silicon dioxide one (Figure A2.a).

Morphology dramatically changes when growth is performed on substrates kept at 90°C. We observe a quasi-spherical grain structure on all substrates, probably due to a Stranski-Krastanov (2D+3D) growth (Figures A2.b and A3.b). An Ostwald-ripening behaviour can also be observed: there are empty regions (with absence of nucleation centers) around the larger grains, due to the coalescence of smaller neighbouring grains. The grain diameter varies from 0,5 to about 1 μm. In the SiO_2/HMDS case (Figure A3.b) a higher density of grains with smaller diameters is observed, and they seem to arrange in a more ordered way with respect to other substrates (Figure A2.b).

The 7th-C3 films grown at RT present radically different morphologies when deposited on silicon dioxide or on SiO_2/HMDS. On SiO_2 substrate, the AFM shows an homogeneous growth pattern consisting of small grains (Figure A2.c). In films grown on SiO_2/HMDS substrate we observe a 3D structure with unusual “coral-like” domains (Figure A3.c). The material preferentially grows along the z axis, giving rise to high and inhomogeneous “towers”.

Instead, 90°C films show a very flat surface with very small and ordered grains (Figures A2.d and A3.d), independently of the substrate.

The grain dimension is roughly estimated to be around 100 nm in the RT grown films, while they are slightly smaller in the 90°C cases.

Changes observed in morphology between compounds 7-th and 7th-C3 can be ascribed to the presence of alchilic chains in 7th-C3 which strongly affect the molecule packing and their interaction with the substrates.

In ALK-Ph molecules grown at RT we observe small and homogenous grains in all substrates (Figures A2.e and A2.e). Deposition on SiO_2 at 90°C is dominated by large and disordered islands (3-D growth) with poor inter-island connections (Figure A2.f).
Instead, morphology in ALK-Ph grown at 90°C on SiO_2/HMDS is similar to that of 7th, showing quasi-spherical grains with various dimensions within 1 and 2 μm (Figure A3.f).

In MB02 RT cases we observed the same morphology both for silicon dioxide and HMDS treated SiO_2: elongated grains with high surface coverage and no pinhole presence. Huge changes occur if growth is performed at 90°C. In SiO_2 case, big quasi-spherical grains with some inter-grain connection are present, whereas in HMDS treated substrates smaller grains with various shapes and chaotic distribution appear. Furthermore, increasing the substrate temperature induces a beginning of pinholes appearance with lower homogeneous coverage. This could be one reason why the field effect mobility in the 90°C cases is lower than in the RT ones, especially with HMDS treated substrates (see next Section).

To summarize, the morphological analysis shows that the substrate temperature is the most important parameter, as it determines the growth modality of all samples. The molecule diffusion on the substrate increases at higher temperature, and this probably involves different crystalline domain arrangements. For this reason, a temperature change determines a dramatic variation in the film growth of this class of organic molecules.
It is remarkable that the 7th-C3 morphology at RT shows huge differences depending on the substrate, even though we analyzed films with a constant thickness of 50 nm. This is probably due to a stronger molecule-substrate interaction with respect to the inter-molecular one. In other compounds this feature was not observed. This characteristic is lost when we heat the substrate during the growth, providing energy for molecules to rearrange.
The MB02 is also very interesting for FET applications even if it drastically changes its morphology when temperature increases, and lowers OFET characteristics[4].

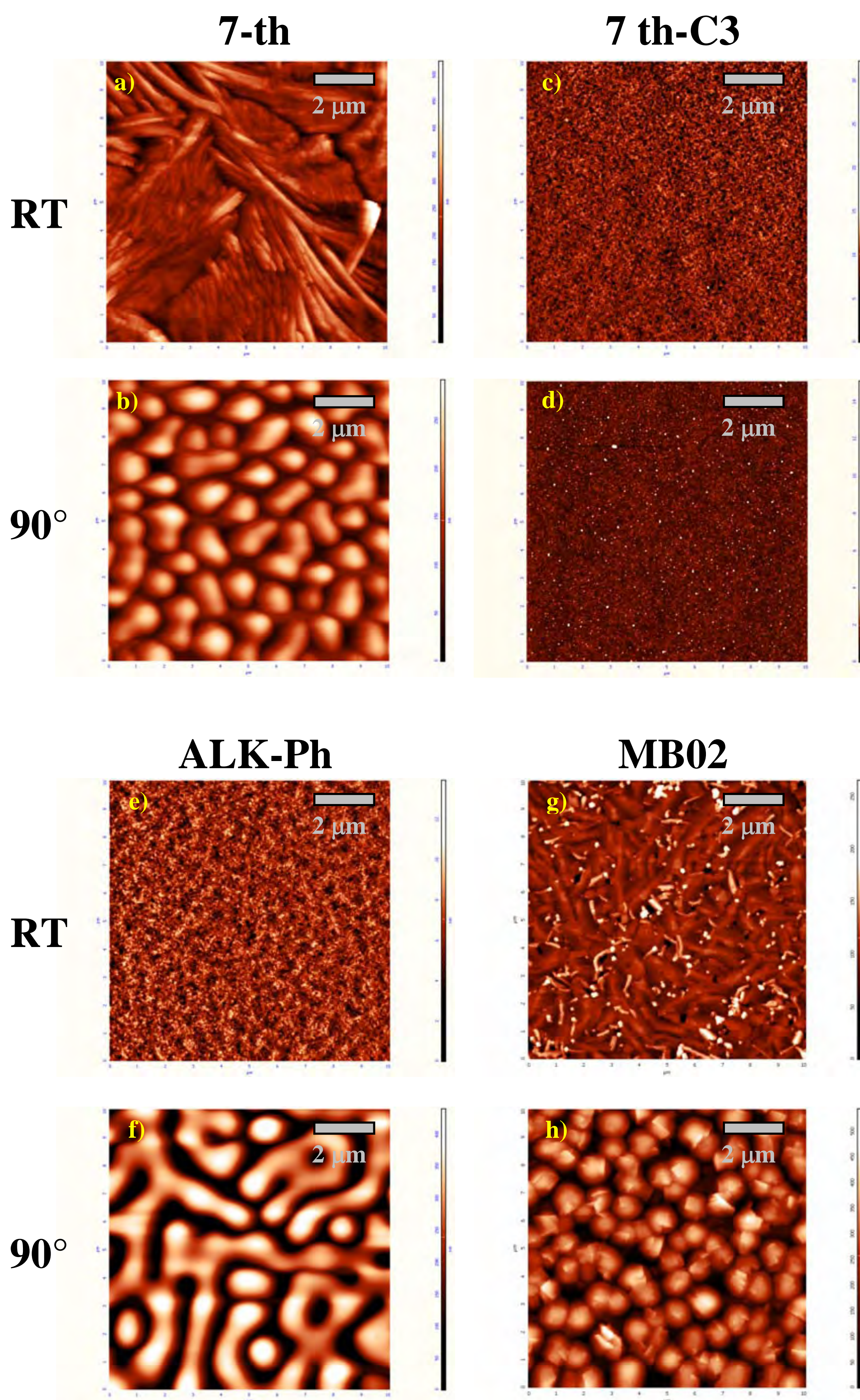

Figure A2: 10 x 10 µm AFM images of 7-th, 7th-C3, ALK-Ph and TMT68 on SiO_2 grown at RT and 90°C

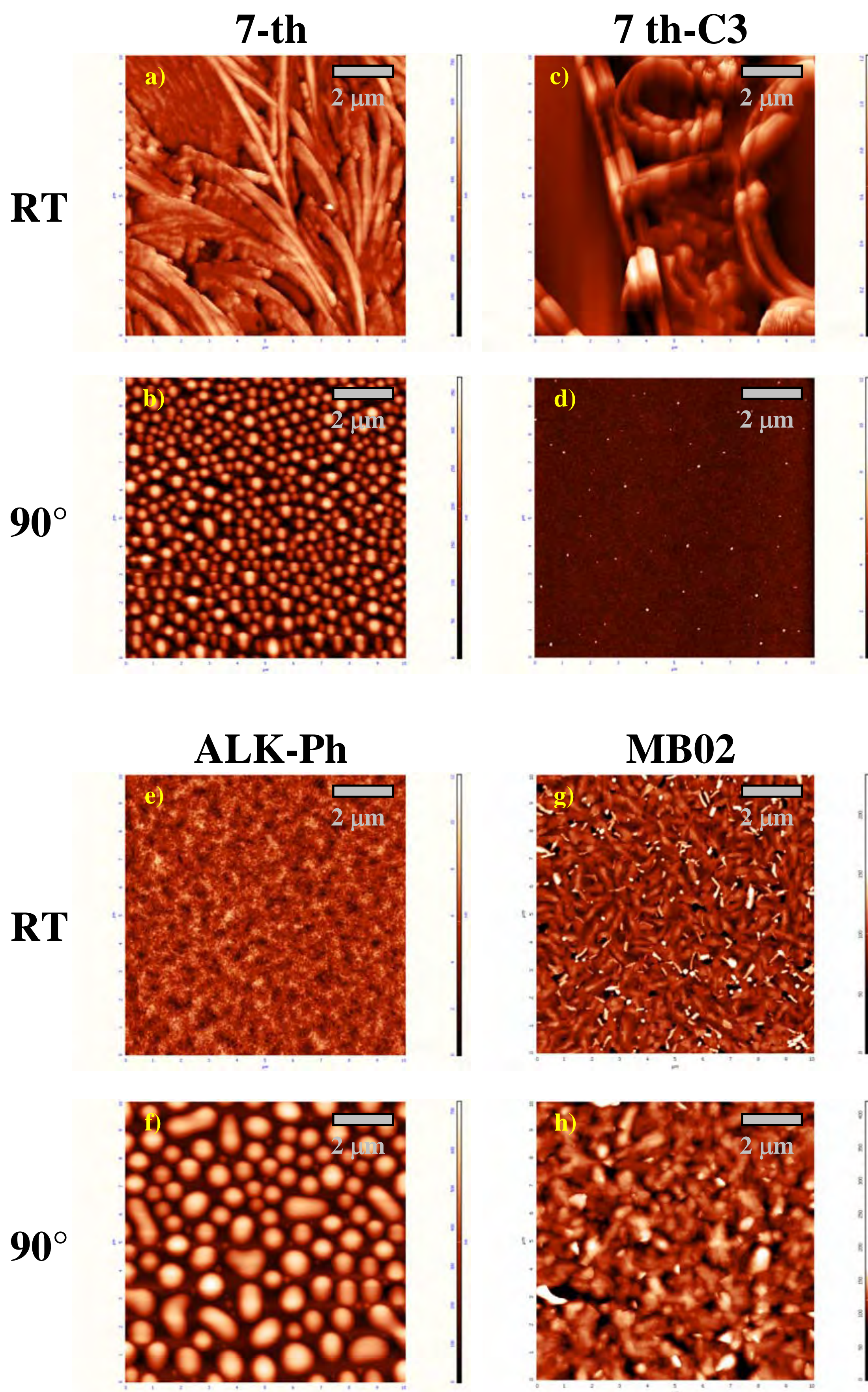

Figure A3: 10 x 10 μm AFM images of 7-th, 7th-C3, ALK-Ph and MB02 on HMDS grown at RT and 90°C

Collaboration: Electrical response

As already mentioned, the electrical field-effect measurements were performed by the Prof. T.J. Marks and Dr. A. Facchetti group at the *Department of Chemistry and the Materials Research Center* of Northwestern University (Table A1). We report these results to show how morphology strongly influences the field-effect performance of OFETs.

In particular, morphologies like 7 th-C3 on SiO_2 seem very homogeneous and compact and good electrical performances should be expected; the lack of conduction is probably due to the diffuse presence of grain boundaries (small grains). Instead, morphologies like the one of 7th-C3 on HMDS at RT clearly prevent any possible field-effect conduction because of the total absence of grain connectivity.

The best performance is obtained with MB02 on HMDS treated SiO_2 substrate, consistently with its morphology that presents elongated grains with high surface coverage and no pinhole presence.

Helicens	*Substrate*	μ^{RT} *(cm²/Vs)*	V_t^{RT} *(V)*	*On/Off* ^{RT}	$\mu^{90°}$ *(cm²/Vs)*	$V_t^{90°}$ *(V)*	*On/Off* $^{90°}$
7-th	SiO_2	1.7×10^{-7}	- 66	10^2	-	-	-
7-th	HMDS	-	-	-	-	-	-
7 th-C3	SiO_2	-	-	-	-	-	-
7 th-C3	HMDS	-	-	-	-	-	-
ALK-Ph	SiO_2	-	-	-	4.8×10^{-7}	- 20	10^1
ALK-Ph	HMDS	1.1×10^{-5}	- 44	10^3	1.2×10^{-7}	- 48	10^3
MB02	SiO_2	9.0×10^{-4}	- 49	10^6	3.0×10^{-4}	- 46	10^6
MB02	HMDS	2.0×10^{-2}	- 56	10^7	8.0×10^{-6}	-	10^2

Table A1: Mobility (μ, cm^2 V^{-1}s^{-1}), on/off ratios (I_{on}:I_{off}), and threshold voltages (V_t, V) for vacuum-deposited films of helicens at RT and 90°C.

Conclusions

Helicenes are very interesting helical-shaped aromatic systems, and they posses great potential for the use as new materials in photonic and opto-electronic applications. In particular carbo-helicenes have been deeply investigated for their non-linear optical properties. Heterohelicenes, such as the ones employed in our work, received much less attention, but in principle they have similar interesting and peculiar features.

Recently, tetrethia[7]helicene (7-th) has been investigated as new candidates for non linear optics[5,6] (NLO). Furthermore, his precursor, the 1,2-dibenzoditiofene-etene (MB02) has been used as active material for an OFET[4].

The interest in this heterohelicene family stems from the consideration that functionalising the two terminal thiopene rings should be easy and versatile. The possibility of introducing functional groups in a regioselective manner could allow their steric and electronic properties to be tuned in order to achieve efficient materials for OFETs active layer and/or for non-linear optic applications.

In our study, a preliminary analysis of the growth modality and field-effect response of few compound belonging to the 7-th family has been performed. This is the first step in view of their use in devices such as e.g OFETs.

References Appendix:

[1] S, Maiorana, A. Papagni, E. Licandro, R. Annunziata, P. Paravidino, D. Perdicchia, C. Giannini, M. Bencini, K. Clays, A. Persoons, *Tetrahedron*, 59, 6481, **2003**.

[2] C. Bandoli, A. Bossi, C. Giannini, E. Licandro, S. Maiorana, D. Perdicchia, M. Schiavo, *SynLett*, 7, 1137, **2005**.

[3] A. Bossi, S. Maiorana, C. Graiff, A. Tiripicchio, E. Licandro, *Eur. J. Org. Chem.*, 4499, **2007**.

[4] K. Yamaguchi, K. Nakashima, S. Takamiya, M. Minami, Y. Doge, Y. Nishide, H. Osuga, K. Uno, C. Nakamoto, I. Tanaka, *Jap. J. Appl. Phys.*, 46, L727, **2007**.

[5] B. Champagne, J.M. André, E. Botek, E. Licandro, S. Maiorana, A. Bossi, K. Clays, A. Persoons, *ChemPhysChem*, 5, 1438, **2004**.

[6] K. Clays, K. Wostyn, A. Persoons, S. Maiorana, A. Papagni, C. Daul, V. Weber, *Chem. Phys. Lett.*, 372, 438, **2003**.

Acknowledgments

I would like to thank my supervisors Renato Bozio at the University of Padova and Michele Muccini at the Istituto per lo Studio dei Materiali Nanostrutturati C.N.R. Bologna who allowed me to earn my PhD. A special thank to all the people involved in the work reported in this thesis and especially, for the courage they demonstrated when working with me, Raffaella Capelli, Franco Dinelli, Stefano Toffanin and Mauro Murgia.

I thank all my colleagues of the Istituto per lo Studio dei Materiali Nanostrutturati (ISMN) C.N.R. of Bologna.

Thanks a lot to all my friends and to the special people I have met in the past three years. Thank you guys, my walk would have been harder without you. I am also indebted with some people who helped me with writing this thesis and correcting the English grammar.

Finally, I would like to dedicate this thesis to my family. Profound apologies to my parents, for making them suffer throughout my "never ending" education and my swinging mood! Mum, Dad, I am joking. I have not finished studying yet!!!

“Theory is when we know everything but nothing works. Praxis is when everything works but we do not know why. We always end up by combining theory with praxis: nothing works and we do not know why.”

Albert Einstein

“Teamwork is essential - it allows you to blame someone else.”

Arthur Bloch